



**HAL**  
open science

## Search for a neutron dark decay in $6He$

Marius Le Joubioux

► **To cite this version:**

Marius Le Joubioux. Search for a neutron dark decay in  $6He$ . Nuclear Experiment [nucl-ex]. Normandie Université, 2024. English. NNT : 2024NORMC223 . tel-04816935

**HAL Id: tel-04816935**

**<https://theses.hal.science/tel-04816935v1>**

Submitted on 3 Dec 2024

**HAL** is a multi-disciplinary open access archive for the deposit and dissemination of scientific research documents, whether they are published or not. The documents may come from teaching and research institutions in France or abroad, or from public or private research centers.

L'archive ouverte pluridisciplinaire **HAL**, est destinée au dépôt et à la diffusion de documents scientifiques de niveau recherche, publiés ou non, émanant des établissements d'enseignement et de recherche français ou étrangers, des laboratoires publics ou privés.

# THÈSE

Pour obtenir le diplôme de doctorat

Spécialité **PHYSIQUE**

Préparée au sein de l'**Université de Caen Normandie**

## Search for a Neutron Dark Decay in $6\text{He}$

Présentée et soutenue par

**MARIUS LE JOUBIOUX**

**Thèse soutenue le 22/10/2024**

devant le jury composé de :

M. HERVÉ SAVAJOLS	Directeur de recherche au CNRS - 14 GANIL de CAEN	Directeur de thèse
MME FRANCESCA GULMINELLI	Professeur des universités - Université de Caen Normandie (UCN)	Président du jury
M. BERTRAM BLANK	Directeur de recherche au CNRS - UNIVERSITE BORDEAUX 1 SCIENCES ET TECHNOLOGIE	Membre du jury
M. DAVID MCKEEN	Chercheur - TRIUMF, MOB 231	Membre du jury
M. MAREK PFÜTZNER	Professeur - Université de VARSOVIE	Rapporteur du jury
MME STÉPHANIE ROCCIA	Maître de conférences - Université Grenoble Alpes	Rapporteur du jury

Thèse dirigée par **HERVÉ SAVAJOLS** (Grand Accélérateur National d'Ions Lourds)



# Remerciements

Le paradoxe de la thèse, c'est qu'on la trouve trop courte et trop longue à la fois. Content d'y être et heureux d'en finir ; bien heureux même. Si j'ai pu arriver jusque là, c'est avant tout grâce à beaucoup de personnes qui m'ont aidé et qui m'ont inspiré. Ces remerciements sont pour vous.

Le début pour mon directeur. Cette expérience unique, je la dois à Hervé Savajols, mon directeur de thèse pour qui il me paraît bien normal d'ouvrir le bal de ces remerciements. Hervé, je te remercie chaleureusement de m'avoir offert l'opportunité de travailler à tes côtés pour une thèse au sujet bien exotique, à l'interface entre physique nucléaire et physique des particules. J'espère qu'on aura pu explorer au maximum cette "cerise sur le côté" qu'est le dark decay et que tu es satisfait du résultat.

La suite pour la "core team". Je remercie Leendert Hayen, qui a plus que débloqué la situation quant à l'interprétation théorique de notre résultat et grandement contribué à l'écriture du PRL. Je remercie Wolfi pour sa contribution à l'expérience, à l'analyse et à la rédaction de l'article. Enfin, je remercie très chaleureusement Xavier Fléchar. Merci pour tout le temps que tu as passé à discuter avec moi sur l'analyse des données ; tant sur l'hélium 6 que sur l'hélium 8. Ta bonne humeur est contagieuse et j'ai beaucoup appris grâce à toi. Ce fut un plaisir de tous vous rencontrer.

La suite pour le GANIL. Je remercie la direction du GANIL, passée et présente, de m'avoir permis d'effectuer ma thèse dans des bonnes conditions. Je remercie tous les chercheurs, ingénieurs et techniciens avec qui j'ai pu échanger et collaborer ces trois dernières années. Je remercie bien évidemment tous les doctorants et post-docs, ceux arrivés avant moi et ceux arrivés après, pour toutes les discussions lors des repas du midi, des pauses cafés et des différentes sorties que l'on a pu faire ensemble. Une mention spéciale à ma génération de doctorant : Hope, (feu) Arpan et Antoine. C'était un plaisir de partager ces moments avec vous. Antoine, merci d'avoir écouté mes multiples plaintes sur ma thèse en dépit des nombreuses difficultés que tu as rencontré au cours de la tienne ; ta résilience me servira toujours de modèle. Bon courage pour la suite !

La suite pour mes amis. Un très grand merci à Alexis, Victor et Antoine de m'avoir soutenu et supporté ces dernières années. Les nombreuses discussions, soirées et parties m'ont été très précieuses et j'espère qu'on continuera à apprendre ensemble le stoïcisme et la valeur de l'argent. Je remercie également toutes les personnes qui, d'une manière

---

ou d'une autre, ont façonné et animé mon quotidien depuis des années. Vous nommer tous ici serait trop long, mais si vous vous retrouvez un jour à lire ces lignes, alors pas de doute : c'est de vous que je parle.

La fin pour ma famille. Je remercie du fond de mon cœur mes parents, Stéphane et Mylène. Vous avez toujours su me guider et me soutenir et ce, malgré tous les problèmes auxquels vous avez dû faire face ces dernières années. J'espère qu'un jour, je pourrai partager avec les autres toutes les belles choses que vous m'avez apportées. Je remercie aussi très fort mes deux frères Antoine et Rémi. Vous êtes mes premiers modèles et sachez qu'aujourd'hui encore je prends exemple sur vous deux. Enfin je remercie mes grands-parents qui ont aussi beaucoup participé à mon éducation. J'ai une pensée particulière pour mon papi, Yves, décédé en décembre 2023. D'une certaine façon, ton cursus étudiant a suscité le mien et je sais que tu aurais aimé me voir arriver au bout ; on se loupe de peu.

Merci à tous,  
Marius

*À ceux qui cheminent encore à mes côtés,  
à ceux qui veillent désormais de loin.*

# Contents

<b>Remerciements</b>	<b>i</b>
<b>General introduction</b>	<b>1</b>
<b>1 The neutron lifetime</b>	<b>3</b>
1.1 Elements of $\beta$ decay	4
1.1.1 General description	4
1.1.2 The $\beta$ decay of free neutrons	6
1.2 The neutron lifetime from experiment	8
1.2.1 The beam method	8
1.2.2 The bottle method	12
1.2.3 The neutron lifetime discrepancy	15
1.2.4 Other results and future lifetime experiments	19
1.3 Summary	20
<b>2 Attempts at resolving the discrepancy</b>	<b>21</b>
2.1 Beyond experimental effects	22
2.1.1 Radiative and bound-state $\beta$ decay	22
2.1.2 Mirror oscillations of free neutrons	23
2.1.3 Soft scattering between neutrons and dark matter	24
2.1.4 Existence of a neutron excited state	24
2.2 The neutron dark decay	25
2.2.1 Open mass range	26
2.2.2 Effective Lagrangians and decay rates	27
2.2.3 Investigations of the $n \rightarrow \chi\gamma$ and $n \rightarrow \chi e^+e^-$ decays	28
2.2.4 Neutron stars	29
2.3 Nuclear dark decays	31
2.3.1 Dark decay in $^{11}\text{Li}$ , $^{11}\text{Be}$ , $^{15}\text{C}$ and $^{17}\text{C}$	32
2.3.2 Discussing the $^{17}\text{C}$ case	33
2.3.3 Dark decay in $^6\text{He}$	34
2.4 Summary	35
<b>3 E819S experiment at GANIL</b>	<b>36</b>
3.1 Overview of the experiment	37
3.2 Neutron detector TETRA	39

3.2.1	Description . . . . .	39
3.2.2	Possible sources of background . . . . .	40
3.2.3	Calibration . . . . .	41
3.3	HPGe detector . . . . .	43
3.3.1	Data analysis and calibrations . . . . .	44
3.3.2	Comparison with classic threshold . . . . .	46
3.4	Other diagnostics . . . . .	49
3.4.1	Plastic scintillator . . . . .	49
3.4.2	Transformateur d'intensité . . . . .	49
3.4.3	Silicon detector . . . . .	50
<b>4</b>	<b><sup>8</sup>He analysis</b>	<b>51</b>
4.1	<sup>8</sup> He decay scheme . . . . .	52
4.2	Average <sup>8</sup> He beam intensity . . . . .	53
4.2.1	Analysis method . . . . .	53
4.2.2	Results of the calculations . . . . .	57
4.2.3	<sup>8</sup> He beam intensity versus primary beam intensity . . . . .	57
4.3	Detection efficiency of the plastic scintillator . . . . .	59
4.3.1	Data analysis of the plastic scintillator . . . . .	59
4.3.2	G4beamline simulations . . . . .	61
4.4	<sup>8</sup> He half-life measurement . . . . .	66
4.4.1	First analysis . . . . .	66
4.4.2	Deadtime corrections . . . . .	69
4.4.3	Summary and best <sup>8</sup> He half-life estimate . . . . .	73
<b>5</b>	<b><sup>6</sup>He analysis</b>	<b>75</b>
5.1	Overview of the model . . . . .	76
5.2	<sup>6</sup> He beam monitoring . . . . .	77
5.2.1	γ rays and bremsstrahlung detection with the HPGe . . . . .	77
5.2.2	Evaluation of $r_0$ from the plastic scintillator . . . . .	78
5.3	TETRA analysis . . . . .	79
5.3.1	Bremsstrahlung detection . . . . .	80
5.3.2	Anomalous counters with spurious events . . . . .	82
5.3.3	Searching for events above the background level . . . . .	84
5.4	Evaluation of $Br_\chi$ . . . . .	88
5.4.1	Fit procedure . . . . .	88
5.4.2	Results . . . . .	88
5.4.3	Stringent upper limit . . . . .	90
<b>6</b>	<b>Mass mixing constraint</b>	<b>92</b>
6.1	Overview . . . . .	93
6.2	Decay rate calculations . . . . .	93
6.2.1	General formula . . . . .	93
6.2.2	Decay amplitude in <sup>6</sup> He . . . . .	94

## CONTENTS

---

6.2.3	$\chi$ parameter space . . . . .	95
6.2.4	$\phi$ parameter space . . . . .	98
6.3	Dark decay in $^{17}\text{C}$ . . . . .	99
6.3.1	Monte Carlo simulations of the $^{17}\text{C}$ decay . . . . .	99
6.3.2	Result of the simulations . . . . .	100
6.4	Conclusion and perspective . . . . .	102
<b>General conclusion</b>		<b>104</b>
<b>A Compilation of <math>\lambda</math> measurements</b>		<b>106</b>
<b>B Calculation of <math>\Gamma_{n \rightarrow \chi\phi}</math></b>		<b>107</b>

# General introduction

Neutrons are electrically neutral particles discovered by James Chadwick in 1932. They are slightly heavier than protons and, because of that, can decay into the latter through  $\beta$  decay. The neutron lifetime is usually interpreted as the typical time it takes for a neutron to turn into a proton. Over the last 20 years or so, many experiments have been carried out to measure its value. They are generally divided into two categories according to their experimental design. On the one hand, bottle experiments access the neutron lifetime by measuring the rate at which a population of ultracold neutrons disappears from a trap where they are confined. On the other hand, beam experiments access the neutron lifetime by comparing the intensity of a cold neutron beam with the rate of charged particles emerging from this beam. Today, the accepted lifetime value falls just below 880 seconds and corresponds to a weighted average of eight measurements, all from bottle experiments.

Although much less numerous, averaging the beam results achieves a neutron lifetime of 888 seconds, higher than the lifetime from bottle measurements. This 1% difference between beam and bottle experiments is known as the neutron lifetime discrepancy. This discrepancy comes with a tension around the  $4\sigma$  level, suggesting the existence of systematic effects in either type of experiments. If this difference does not come from any overlooked issues in the technical design or data analysis of these experiments, then it might point to the existence of unknown neutron physics. New theories trying to address the neutron lifetime discrepancy usually imply changing the way we have conceptualized the neutron lifetime measurements. The focus of this PhD thesis lies under one particular model : the neutron dark decay.

Proposed in 2018 by Fornal and Grinstein, this theory suggests the existence of another possible decay mode for neutrons, involving neutral particles in the final state which could be dark matter candidates. This model implies that the neutron lifetime from bottle experiments corresponds to the total lifetime, whereas beam experiments only give the partial lifetime associated with the neutron  $\beta$  decay. If dark decays can happen for free neutrons, they could also occur for neutrons loosely bound in a selection of radioactive

## CONTENTS

---

nuclei. One possible candidate for investigating nuclear dark decays is the borromean  ${}^6\text{He}$  nucleus. A dark decay in this nucleus would result in the emission of a free neutron, providing a clean and unique signature, as this type of emission is not possible in a standard  ${}^6\text{He}$  decay from its ground state. In this thesis, we present the data analysis and the result of an experiment designed to look for this exotic process in  ${}^6\text{He}$  and how this experiment constrains the neutron dark decay paradigm.

# Chapter 1

## The neutron lifetime

The Standard Model (SM) is the theory of fundamental particles and describes how they interact with each other. The SM has proven incredibly successful at describing many features of nature, but, as with many theories, it does not answer everything and many questions remain unsolved. We will open this first chapter with an introduction to the  $\beta$  decay phenomenon and its formalism followed by a focus on the free neutron  $\beta$  decay and the various attempts at measuring its lifetime throughout the years.

### Contents

---

<b>1.1 Elements of <math>\beta</math> decay</b> . . . . .	<b>4</b>
1.1.1 General description . . . . .	4
1.1.2 The $\beta$ decay of free neutrons . . . . .	6
<b>1.2 The neutron lifetime from experiment</b> . . . . .	<b>8</b>
1.2.1 The beam method . . . . .	8
1.2.2 The bottle method . . . . .	12
1.2.3 The neutron lifetime discrepancy . . . . .	15
1.2.4 Other results and future lifetime experiments . . . . .	19
<b>1.3 Summary</b> . . . . .	<b>20</b>

---

## 1.1 Elements of $\beta$ decay

### 1.1.1 General description

The  $\beta$  decay model describes the transformation of one particle into another by the emission of a  $\beta^\pm$  particle or by electronic capture, to achieve stability. These decays occur at the level of fundamental quark and lepton particles due to the weak interaction mediated by a  $W$  boson. In a typical  $\beta^-(\beta^+)$  decay, a *down(up)*-like quark transforms into a *up(down)*-like quark with the emission of an electron (positron) and an antineutrino (neutrino). At the quark or nucleon level, this can be written as :

$$\begin{aligned} d &\rightarrow u + e^- + \bar{\nu}_e \text{ or } n \rightarrow p + e^- + \bar{\nu}_e, \\ u &\rightarrow d + e^+ + \nu_e \text{ or } p \rightarrow n + e^+ + \nu_e. \end{aligned} \tag{1.1}$$

The typical Feynman diagram corresponding to a  $\beta^-$  decay is shown in Figure 1.1. In an electronic capture process, an electron from an atomic shell is captured by a proton (or an  $u$  quark) resulting in the emission of a neutron (or a  $d$  quark) and a neutrino :

$$u + e^- \rightarrow d + \nu_e \text{ or } p + e^- \rightarrow n + \nu_e. \tag{1.2}$$

The vast majority of isotopes known today are unstable. Neutron-rich isotopes generally achieve stability due to  $\beta^-$  decay, while neutron-deficient isotopes will achieve stability through  $\beta^+$  decay and electronic capture.

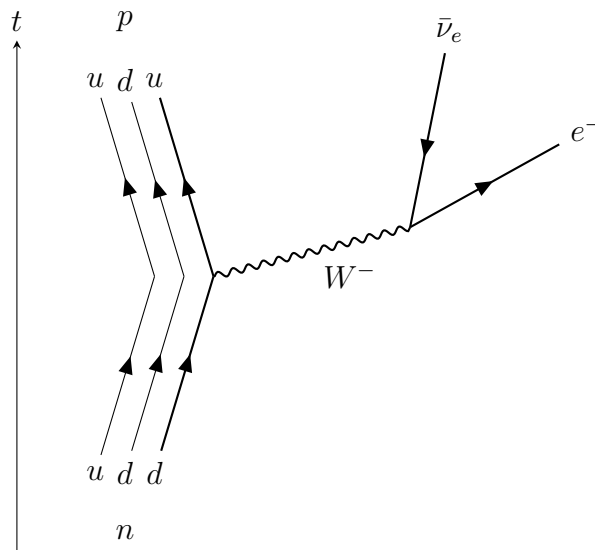


FIGURE 1.1 – First-order Feynman diagram of a  $\beta^-$  decay. A valence  $d$  quark inside the neutron is turned into an  $u$  quark by emission of a  $W^-$  boson. The  $W^-$  decays into an electron and an antineutrino afterward.

### Fermi theory of $\beta$ decay

The first successful theory that describes  $\beta$  decay was given by Fermi in 1934 [1] and is based on the existence of the neutrino as suggested by Pauli in 1931. His theory allowed physicists to compute the decay rate and the expected energy and momentum distributions for the emitted electron by considering the weak interaction as a 4-fermion contact interaction with an effective coupling strength  $G_F$  known as the Fermi constant. The total  $\beta$  decay rate can be formulated as :

$$\Gamma = \frac{G_F^2 |M_{fi}|^2}{2\pi^3 \hbar^7 c^3} \int_0^{p_{max}} F(Z_d, p_e) (Q - T_e)^2 p_e^2 dp_e, \quad (1.3)$$

where  $|M_{fi}|^2$  is the probability to go from one initial (parent nucleus) to a final (daughter nucleus) nuclear state also known as the nuclear matrix element and  $Q$  is the available energy.  $T_e$  and  $p_e$  represent the electron kinetic energy and momentum, respectively. The term  $F(Z_d, p_e)$  is a factor that takes into account the attraction (or repulsion in the case of a  $\beta^+$  decay) between the electron and the daughter nucleus. It is a function of the number of protons in the daughter nucleus  $Z_d$  and the momentum of the electron  $p_e$ . This integral is known as the Fermi integral and has been evaluated numerically for different values of  $Z_d$  and  $Q$ . It is typically written as :

$$f(Z_d, Q) = \frac{1}{m_e^5 c^7} \int_0^{p_{max}} F(Z_d, p_e) (Q - T_e)^2 p_e^2 dp_e, \quad (1.4)$$

where the  $1/(m_e^5 c^7)$  term has been added to make the integral dimensionless. Finally, the decay rate can be expressed as :

$$\Gamma = \frac{\ln(2)}{t_{1/2}} = \frac{2m_e^5 c^4 G_F^2 |M_{fi}|^2}{2\pi^3 \hbar^7} f(Z_d, Q), \quad (1.5)$$

where  $t_{1/2}$  is the nucleus half-life.

### Classification of $\beta$ decay

Since  $t_{1/2}$  and  $Q$  can be measured experimentally, multiplying  $t_{1/2}$  by the Fermi integral gives a quantity called the comparative half-life that depends only on the nuclear matrix element and allows to compare different nuclear  $\beta$  decays :

$$ft_{1/2} = \ln(2) \frac{2\pi^3 \hbar^7}{2m_e^5 c^4 G_F^2 |M_{fi}|^2}. \quad (1.6)$$

Furthermore,  $\beta$  decays are generally characterized and classified according to their angular momentum and parity transition. The conservation of angular momentum in  $\beta$  decays can be written :

$$\vec{J}_i = \vec{J}_f + \vec{L} + \vec{S} \Rightarrow \Delta\vec{J} = \vec{J}_i - \vec{J}_f = \vec{L} + \vec{S}, \quad (1.7)$$

where  $\vec{J}_i$  and  $\vec{J}_f$  are the initial and final state nuclei spin.  $\vec{L}$  and  $\vec{S}$  are the total orbital

and spin angular momentum of the lepton pair,  $\vec{L} = \vec{L}_e + \vec{L}_\nu$ ,  $\vec{S} = \vec{S}_e + \vec{S}_\nu$ . The parity conservation is :

$$\pi_i = \pi_f(-1)^L \Rightarrow \Delta\pi = \pi_i\pi_f = (-1)^L, \quad (1.8)$$

where  $\pi_i$  and  $\pi_f$  are the initial and final state parity respectively. A  $\beta$  decay is called a Fermi decay when  $S = 0$  and a Gamow-Teller decay when  $S = 1$ . When leptons in the final state are produced in a  $s$ -wave relative to the nucleus ( $L = 0$ ), the transition is called an *allowed* transition. When they are emitted with a higher orbital momentum ( $L \geq 1$ ), the transition is called a *forbidden* transition of order  $L$ . For example, a transition with  $L = 1$  is a *first forbidden*  $\beta$  decay. Here, the term *forbidden* simply means that these transitions are less likely to occur compared to *allowed* ones.

A qualitative indicator of the type of any  $\beta$  transition is the so-called  $\log ft$  value. Allowed  $\beta$  decays have a distribution of  $\log ft$  values between 2 and 13, whereas forbidden decays have  $\log ft$  values no smaller than 5 and up to 25. A recent review of this classification can be found in [2].

### Superallowed $\beta$ decay

A special case of *allowed* Fermi decays are the  $0^+ \rightarrow 0^+$  *superallowed*  $\beta$  decays. They are pure Fermi transitions with typical  $\log ft$  values between 3 and 4. It is convenient for *superallowed* decays to write the so-called "*corrected*" (or "*modified*")  $ft$  value [3] :

$$\mathcal{F}t = ft(1 + \delta'_R)(1 + \delta_{NS} - \delta_C), \quad (1.9)$$

where  $\delta'_R$  and  $\delta_{NS}$  are nucleus-dependent radiative correction terms and  $\delta_C$  is known as the isospin-symmetry breaking correction term.

### 1.1.2 The $\beta$ decay of free neutrons

Unlike its isospin doublet counterpart, a free neutron is unstable. A free neutron will undergo the following well-known  $\beta$  decay  $n \rightarrow pe^- \bar{\nu}$  with a lifetime  $\tau_n \sim 880$  seconds and a small release energy of 0.782 MeV. The Standard Model describes this process by the interactions of semileptonic weak currents. A useful scalar quantity used to characterize the nature of particles and describe their dynamics in a physical process is the Lagrangian density. At the quark level, the Lagrangian density of a  $\beta$  decay reads [4] :

$$\mathcal{L}_{d \rightarrow ue\bar{\nu}} = -\frac{G_F}{\sqrt{2}} V_{ud} [\bar{e}\gamma_\mu(1 - \gamma_5)\nu][\bar{u}\gamma^\mu(1 - \gamma_5)d], \quad (1.10)$$

where  $G_F = 1.166\,378\,8(6) \times 10^{-5} \text{ GeV}^{-2}$  is the Fermi constant known to great precision from muon decay [5, 6]. In the case of momentum transfers that are small compared to the mass of the  $W$  boson  $m_W \approx 80.4 \text{ GeV}$  (like  $\beta$  decay), the Fermi constant is related to the weak coupling constant  $g_w$  as  $G_F/\sqrt{2} = g_w^2/m_W^2$ . The other terms that appear in this Lagrangian are  $V_{ud}$ , the first component in the Cabibbo-Kobayashi-Maskawa (CKM) matrix [7], the gamma matrices  $\gamma_\mu$  and  $\gamma_5$ , and a Dirac spinor for each fermion  $d$ ,  $u$ ,  $\nu$  and  $e$ . This Lagrangian exhibits here the Vector - Axial Vector (V - A) nature of the

weak interaction through the term  $\gamma^\mu(1 - \gamma_5)$  that is the combination of a positive vector current ( $\bar{\phi}\gamma^\mu\psi$ ) and a negative axial vector current ( $-\bar{\phi}\gamma^\mu\gamma_5\psi$ ).

The CKM matrix describes the mass mixing of quarks. It relates the mass eigenstates of the quarks to their weak eigenstates, which are actually sensitive to the weak current. In its classic parameterization, it is written like :

$$\begin{pmatrix} d' \\ s' \\ b' \end{pmatrix} = \begin{pmatrix} V_{ud} & V_{us} & V_{ub} \\ V_{cd} & V_{cs} & V_{cb} \\ V_{td} & V_{ts} & V_{tb} \end{pmatrix} \begin{pmatrix} d \\ s \\ b \end{pmatrix}. \quad (1.11)$$

This simply corresponds to a rotation in the flavor space. Assuming that there is no 4-*th* generation of quarks and no physics beyond the standard model, the CKM matrix must be unitary. This implies that :

$$\sum_k V_{jk}^* V_{jk} = \sum_k V_{kj}^* V_{kj} = 1, \quad (1.12)$$

which is what is expected from a rotation matrix in a complex space. Now things are different at the nucleon level. Due to its complicated internal structure, the neutron  $\beta$  decay can not be described simply with a free quark current interacting with a leptonic current. For that reason, form factors must be taken into account to address this issue. At leading order, and considering that the momentum transfer is close to zero, the Lagrangian density can be written as [4] :

$$\mathcal{L}_{n \rightarrow pe\bar{\nu}} = -\frac{G_F}{\sqrt{2}} V_{ud} [\bar{e}\gamma_\mu(1 - \gamma_5)\nu][\bar{p}\gamma^\mu(g_V + g_A\gamma_5)n], \quad (1.13)$$

where  $g_V$  and  $g_A$  are known as the vector and axial vector coupling constants respectively. Numerous parameters are implicated in the theory of neutron  $\beta$  decay, some of which have been introduced previously. One of the most crucial variable in this theory is the lifetime of the free neutron. This parameter plays a very important role in many different fields of research from particle physics to cosmology [8]. Indeed, the neutron lifetime is involved in the early life of the Universe, affecting its primordial abundance of light elements like  $^4\text{He}$  and its evolution throughout time. According to the Standard Model, the neutron lifetime can be written in the form [4] :

$$\tau_n = \frac{5024.7 \text{ s}}{|V_{ud}|^2(1 + 3\lambda^2)(1 + \Delta_V^R)}, \quad (1.14)$$

where the numerator value corresponds to the product  $2\pi^3/(f G_F^2 m_e^5)$  where  $f = 1.6887(2)$  is a phase space factor [9] and  $\Delta_V^R = 0.02479(21)$  is an inner radiative correction term to the vector coupling [4]. The parameter  $\lambda$  represents the ratio of the axial-vector coupling constant  $g_A$  to the vector coupling constant  $g_V$ .

$$\lambda \equiv \frac{g_A}{g_V}, \quad (1.15)$$

with a value of  $\lambda = -1.2754(13)$  [10], in good agreement with the (V - A) nature of the weak interaction. This term plays an important role in the many different correlation and asymmetry terms involved in neutron decay. As an example, the  $\beta$  decay asymmetry term  $A$ , which describes the correlation between the neutron spin  $\sigma_n$  and the electron momentum  $p_e$ , can be written as  $A = 2\lambda(\lambda + 1)/(1 + 3\lambda^2)$ .

## 1.2 The neutron lifetime from experiment

Measuring the neutron lifetime has interested physicists since the first observation of its decay in 1948 by Snell and Miller [11] with a rough lifetime estimate between 15 and 30 minutes. Many different experiments have been performed over the past decades, moving the lifetime value from  $\tau_n = 1108 \pm 216$  in Robson's experiment in 1951 [12] down to the actual most precise evaluation at  $\tau_n = 877.75 \pm 0.28_{-0.16}^{+0.22}$  [13] from the UCN $\tau$  measurement in 2021. The lifetime value typically accepted and used by the community comes from the Particle Data Group (PDG). The value listed in their Review of Particle Physics usually takes into account the most recent and accomplished experiments. The evolution of the neutron lifetime as established by the PDG can be seen in Figure 1.2. On average, all neutron lifetime measurements can be roughly divided into two different categories depending on the experimental method used : the beam method and the bottle method. To this day, two papers have reviewed some of these lifetime experiments up to their date of publication. The interested reader should look into the following articles [8, 14].

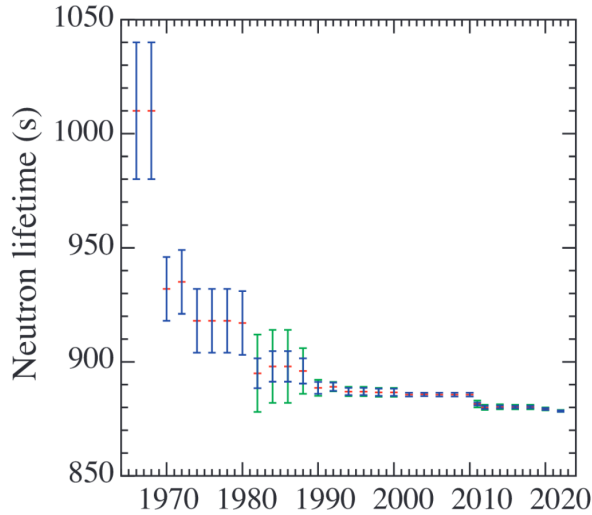


FIGURE 1.2 – Neutron lifetime over the years as established by the PDG from 1966 to 2022. The plot comes from [10].

### 1.2.1 The beam method

#### Description of the method

The beam method was the first to be used in an experiment dedicated to measuring the neutron lifetime [12] and has been used in several different facilities over the years. A beam

of cold neutrons ( $E_{th} \lesssim 25 \text{ MeV}$ ) is sent to a decay volume  $V$  where the decay products (protons and/or electrons) are detected and the lifetime is extracted by comparing the neutron count rate within the beam with the decay product count rate. The neutron beam activity can be expressed as :

$$A = \frac{N}{\tau_n} = \frac{\rho_n V}{\tau_n}, \quad (1.16)$$

where  $N$  and  $\rho_n$  are the cold neutron population and density in the beam at a certain time  $t$ . The neutron density was usually measured by detecting reaction products from a very thin neutron-absorbing foil. The foil material was chosen so that the absorption cross section would follow the  $1/v$  law :

$$\sigma_{abs}(v) = \frac{v_{th}}{v} \sigma_{th}, \quad (1.17)$$

where  $v$  is the neutron velocity and  $\sigma_{abs}$  is the absorption cross section proportional to the reference cross section  $\sigma_{th}$  known for the velocity  $v_{th} = 2200 \text{ m.s}^{-1}$ . The distribution of neutrons with velocity  $v$  within a sectional area of the beam can be written  $d\phi(v)/dv$  where  $\phi(v)$  has the dimension of particles per second and per unit of surface. Therefore, the neutron count rate is expressed as :

$$R_n = \varepsilon_n a \rho_{foil} \int \sigma_{abs}(v) \frac{d\phi(v)}{dv} dv, \quad (1.18)$$

where  $\varepsilon_n$  is detection efficiency for the reaction products,  $\rho_{foil}$  is the foil area density of atoms contributing to the neutron capture and  $a$  is the cross sectional area of the neutron beam. We can make the neutron density appear in the previous equation by injecting the definition of  $\sigma_{abs}$  and express it as a function of the neutron detection rate :

$$\rho_n = \frac{R_n}{\varepsilon_n a \rho_{foil} \sigma_{th} v_{th}}. \quad (1.19)$$

We now have the full expression for the right-hand side of the neutron beam equation 1.16. For the decay products, this activity measurement can simply be written as :

$$A = \frac{R_p}{\varepsilon_p}, \quad (1.20)$$

where  $R_p$  is the decay product detection rate and  $\varepsilon_p$  is the detection efficiency. Using  $V = aL$  where  $L$  is the length of the decay volume, we obtain the final equation for the neutron lifetime from a beam experiment :

$$\tau_n = \frac{L}{\rho_{foil} \sigma_{th} v_{th}} \frac{R_n \varepsilon_p}{R_p \varepsilon_n}. \quad (1.21)$$

### The beam experiment at NIST

The most recent in-beam experiment with a relative precision lower than 1% has reported a lifetime value of  $\tau_n = 886.3 \pm 1.2 \pm 3.2$  seconds in 2005 [15]. The experiment was carried out at the NIST Center for Neutron Research using fission neutrons cooled to thermal levels and transported away from the neutron source to the experimental area through  $^{58}\text{Ni}$  coated neutron guides. The cold neutron beam would pass through a segmented quasi-Penning trap with a well-defined length  $L$  as shown in Figure 1.3. A 4.6 T uniform magnetic field is applied along the neutron beam axis in the opposite direction. The protons emerging from the  $\beta$  decay of neutrons are first trapped and then guided to a silicon detector to be counted. Acceleration voltages ranging from  $-25$  to  $-35$  kV were used to give the protons enough energy to pass the detection threshold. Due to its design, the trap is believed to have a trapping efficiency of 100% everywhere except at both ends where edge effects occur for the potential gradient. The trap was segmented into 16 electrodes to deal with these edge effects by varying the length of the trap like  $L = nl + L_{end}$ , where  $n$  is the number of electrodes with length  $l$  and  $L_{end}$  is the effective length of the two end regions where the trapping efficiency is below unity. The intensity of the neutron beam was determined using a thin  $^6\text{LiF}$  foil coupled to four other silicon detectors to detect the alphas and tritons produced by the neutron absorption reaction with the  $^6\text{Li}$  deposit.

The neutron lifetime was first extracted by plotting the ratio of the measured proton to neutron count rates with respect to the number of electrodes used :

$$\frac{R_p}{R_n} = \frac{1}{\tau_n} \left( \frac{\varepsilon_p}{\rho_{foil}\sigma_{th}v_{th}\varepsilon_n} \right) (nl + L_{end}). \quad (1.22)$$

Many side effects were investigated and taken into account in the analysis, from the size of the neutron beam halo to the determination of losses inside the neutron detectors, resulting in many correction factors applied to the data. The last effect that was looked into is the proton detection efficiency value. Indeed, even if a proton is successfully trapped and sent into the silicon detector, it can still go undetected because of scattering effects. This effect was probed by making lifetime measurements with different silicon detectors (with different dead layer thicknesses), for various acceleration voltages. The

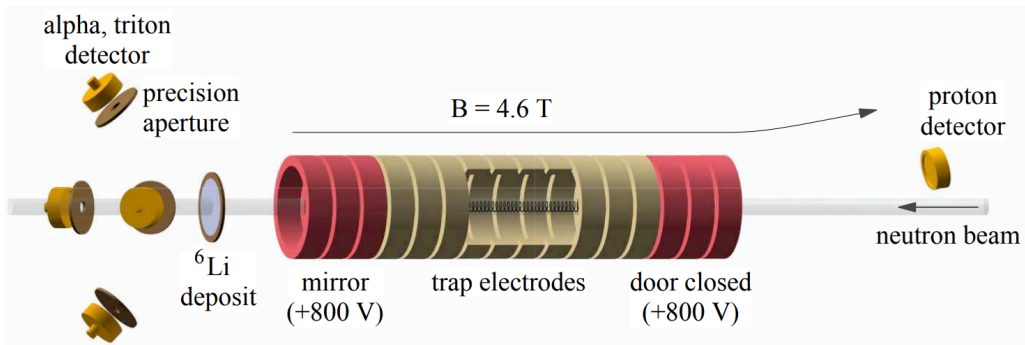


FIGURE 1.3 – Apparatus used to measure the neutron lifetime in a cold neutron beam experiment at NIST. The figure comes from [15].

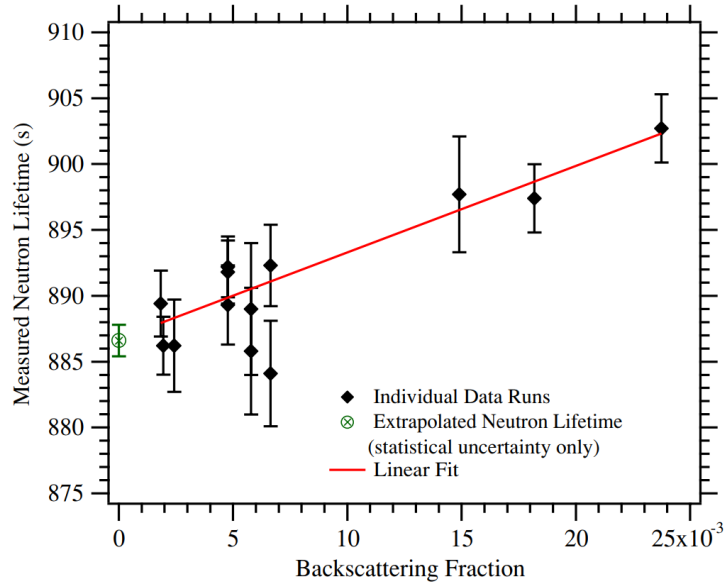


FIGURE 1.4 – Measured neutron lifetime values for different proton detection setups with respect to their calculated proton back scattering fraction [15].

proton backscattering fraction was assessed for each specific setup with SRIM simulations [16]. Finally, the neutron lifetime is evaluated by extrapolating the data to the zero proton backscattering fraction, as shown in Figure 1.4.

### Reassessment of the 2005 NIST result

This result was then reevaluated in a letter published in 2013 [17], mainly addressing the neutron counting part of the 2005 campaign. The neutron density in Equation 1.19 depends directly on the value of the  ${}^6\text{Li}(n, t){}^4\text{He}$  thermal cross section ( $\sigma_{th}$  in equation 1.17). The value used for their analysis was  $(941.0 \pm 1.3)$  b, which was modified to  $(938.5 \pm 1.3)$  b in the Evaluated Nuclear Data Library [18] shortly after publication of the 2005 result. The 2013 publication got rid of the  $\sigma_{th}$  dependence by directly measuring the observed rate of reaction products (alphas and tritons) with the same neutron monitor

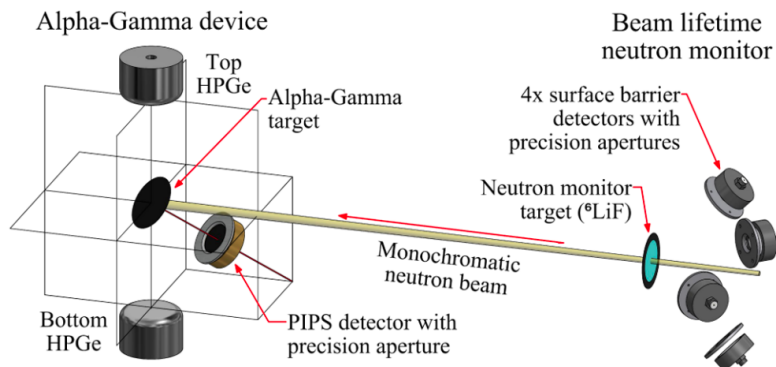


FIGURE 1.5 – Geometry of the experimental setup from 2005 campaign coupled with the Alpha-Gamma device during the 2013 measurements [17].

apparatus as in 2005 and the total neutron rate with the Alpha-Gamma device as shown in Figure 1.5. Correction factors on the solid angle for the reaction product detectors and on the  ${}^6\text{Li}$  target density were also taken into account, lifting the neutron lifetime value to  $\tau_n = 887.7 \pm 1.2 \pm 1.9$  seconds [17]. This result was recently criticized in a paper published in 2020 [19], raising potential problems in several aspects of the experiment. They mainly address all possible effects that can affect proton detection during the experiment, from potential proton interaction with residual gas inside the trap to proton loss effects within the silicon detector. All of these concerns were adequately answered by many co-authors of both original papers [15, 17], standing with their previous result in an article released in 2022 [20].

## 1.2.2 The bottle method

### Description of the method

In the bottle method, a population of ultracold neutrons (UCNs) with  $E_n \lesssim 100$  neV is sent inside a trap to live and die, and a neutron detector is used to monitor the surviving population of neutrons over time. In bottle experiments, the decay products are not detected and only the behavior of the neutron detection rate matters. This means that, contrary to in-beam experiments, bottle experiments are not constrained by detection efficiencies that need to be known precisely. Furthermore, bottle experiments do not rely on a precise evaluation of the neutron population introduced into the trap but rather focus on the neutron detection behavior. On the other hand, as the lifetime in bottle experiments comes from neutron monitoring, any side mechanism leading to neutron loss inside the trap must be thoroughly evaluated, as the apparent lifetime will vary as :

$$\frac{1}{\tau_m} = \frac{1}{\tau_n} + \sum_i \frac{1}{\tau_i}, \quad (1.23)$$

where  $\tau_m$  is the measured or apparent lifetime,  $\tau_i$  is the inverse of the loss rate due to a particular effect  $i$  and  $\tau_n$  is the real neutron lifetime.

In a typical bottle experiment, the neutrons are produced and sent into the trap and the surviving neutrons are counted after two different storage times  $t_1$  and  $t_2$ . The apparent lifetime is then assessed with the following equation :

$$\tau_m = \frac{t_2 - t_1}{\ln(N_1/N_2)}, \quad (1.24)$$

where  $N_1$  and  $N_2$  are the count rates of neutrons after  $t_1$  and  $t_2$  respectively. Bottle experiments can be divided into two categories that correspond to the way neutrons are confined inside the decay volume with either material or magnetic traps. In the former, the walls of the trap are designed so that ultracold neutrons can be almost entirely reflected on their surface. In the latter case, the neutrons are confined by using a strong magnetic field coupling with their magnetic moment. In both scenarios, the kinetic energy of the UCNs is small enough that even gravity plays a role in confining them vertically.

## Material trap

In material trap experiments, interactions between the bottle surface and neutrons are one of the leading causes of variation in the measured lifetime. Even if the trap is carefully designed, a loss probability term must be taken into account corresponding to inelastic scattering and neutron capture reactions.

In the Mambo1 campaign [21] (which stands for Mampe Bottle), it was experimentally evaluated using an almost model-independent method. The decay volume consisted of a glass box with walls coated with Fomblin oil to reflect neutrons as shown on the left-hand side of Figure 1.6. The box had fixed height and width of 30 and 40 cm, respectively, but the depth could be changed thanks to a moving wall. For an isotropic distribution of velocities, the mean free path of the UCNs in the trap can be expressed as  $l = 4V/S$ , where  $V$  and  $S$  are the volume and the surface area of the decay volume. Varying the trap volume for one set of storage times, the neutron lifetime can be assessed by extrapolating the data linearly to the infinite mean free path case (*i.e.* no collision). This data extrapolation can be seen on the right-hand side of Figure 1.6. The final result reported for this experiment was  $\tau_n^{\text{MAMBO1}} = 887.6 \pm 3$  seconds, which is in good agreement with beam lifetime values.

An article published in 2009 proposed different corrections to this result [22]. Monte Carlo simulations of the apparatus were used to investigate the impact of the gravitational potential with respect to the different storage times. They also investigated the presence of above-barrier neutrons in the initial velocity distribution and its evolution within the trap due to quasi-elastic scattering. This paper states that the result of [21] could be lowered to  $\tau_n^{\text{MAMBO1}} = 880.4 \pm 3.0$  seconds. In 2012, another paper included a theoretical description of ultracold neutron scattering on viscoelastic surfaces (like Fomblin oil) in a reanalysis of the Mambo1 experiment [23]. They reported a new value of  $\tau_n^{\text{MAMBO1}} = 882.5 \pm 2.1$  seconds (which is viewed as an official update of the MAMBO1 result), better aligned with the actual accepted neutron lifetime and other bottle results.

Other material trap experiments evaluated the loss probability term with a different

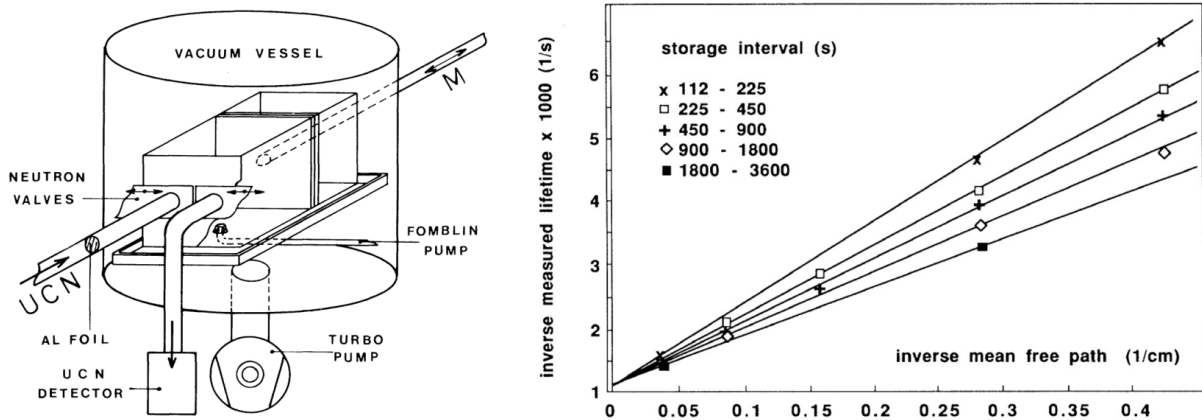


FIGURE 1.6 – LHS : Sketch of the experimental setup used in the Mambo1 neutron lifetime measurement. RHS : The measured decay rate with respect to the inverse mean free path for different values of neutron storage time. Both figures are from [21].

approach. In the first design of the Mambo2 experiment, the loss rate was measured directly by monitoring the number of leaked neutrons with several  $^3\text{He}$  counters outside of the trap. This method was also used in [24], using 18 thermal neutron counters SNM-57 around the trap to detect inelastically scattered neutrons escaping the bottle. Both experiments are based on measuring the supposedly constant ratio of wall losses probabilities  $\lambda_{wl}$  for two different geometry of the setup  $\xi = \lambda_{wl1}/\lambda_{wl2}$ . Once this ratio is measured, the neutron lifetime is obtained through :

$$\frac{1}{\tau_n} = \frac{\xi\lambda_1 - \lambda_2}{\xi - 1}, \quad (1.25)$$

where  $\lambda_1$  and  $\lambda_2$  are the total UCN loss probabilities defined as  $\lambda_i = \lambda_n + \lambda_{wli}$  for each geometry. They reported results of  $\tau_n^{\text{MAMBO2}} = 882.6 \pm 2.7$  seconds [25] in 1993 and  $\tau_n^{\text{ARZUMANOV}} = 880.2 \pm 1.2$  seconds in 2015 [24].

In Gravitrap 1 [26] and 2 [27], the loss rate is written in the form  $\lambda_{\text{loss}} = \eta(T)\gamma(E)$ , where  $\eta(T)$  is the loss factor that depends on the wall temperature  $T$  and  $\gamma(E)$  is the effective collision frequency that depends on the neutron energy and the geometry of the trap. Several  $\gamma$  values are obtained with respect to the UCN energy through Monte Carlo simulations and a mean effective collision frequency is calculated for each specific geometric configuration. Finally, the neutron lifetime is measured by linearly extrapolating the data to the zero collision case. They reported values of  $\tau_n^{\text{GRAV1}} = 878.5 \pm 0.7 \pm 0.3$  seconds and  $\tau_n^{\text{GRAV2}} = 881.5 \pm 0.7 \pm 0.6$  seconds in 2005 and 2018 respectively.

### Magnetic trap

In magnetic trap experiments, neutrons are confined using a strong magnetic field. The magnetic dipole moment of the neutron is  $|\mu_n| = 1.9130427(5)\mu_N$ , where  $\mu_N$  is the nuclear magneton. This corresponds to  $|\mu_n| \approx 60.3 \text{ neV} \cdot \text{T}^{-1}$ . Therefore, the kinetic energy of UCNs is not enough to escape the grasp of a magnetic field with a strength of a few Teslas. In theory, magnetic bottles do not have to worry about wall losses, but other vanishing mechanisms can still be present. In these experiments, the UCNs are usually polarized in one spin state (called low-field seekers), which are kept inside the bottle by the magnetic field, while neutrons in the other spin state (high-field seekers) are sent out of the trap. Therefore, neutron depolarization (or spin flip) can lead to a systemic bias during an experiment. Another loss mechanism in magnetic bottles comes from neutrons with a sufficiently high kinetic energy to overcome the gravitational potential with respect to the apparatus design.

Today's most precise neutron lifetime determination comes from the UCN $\tau$  collaboration in 2021 using a magnetogravitational trap at the Los Alamos Neutron Science Center [13] with data from two different experimental campaigns in 2017 and 2018. The setup used in 2018 is shown in Figure 1.7. UCNs produced by a proton beam-driven solid deuterium source with  $E_n \lesssim 180 \text{ neV}$  were first polarized to the low-field seeker state using a 5.5 T superconducting solenoid and a spin flipper. The polarized UCNs were then sent into a bowl-shaped Halbach array with NdFeB magnets that provided a surface field of  $\sim 1.0 \text{ T}$  to confine the UCNs and electromagnetic coils that produced an ambient field

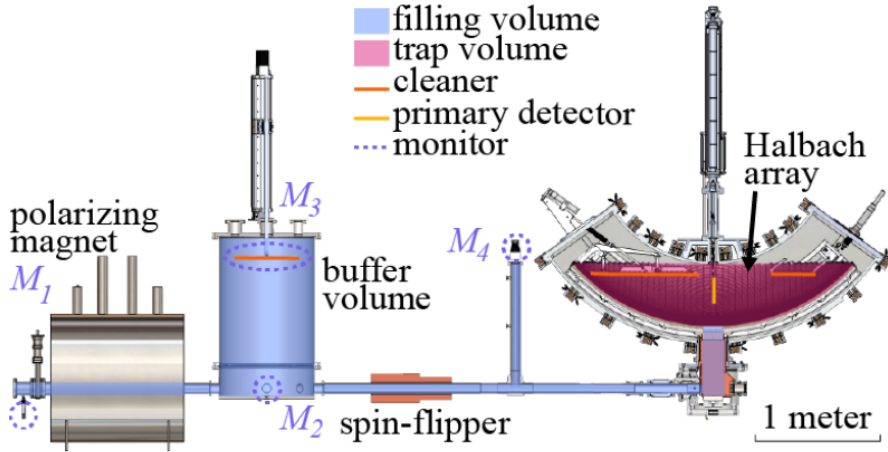


FIGURE 1.7 – The apparatus used in the 2018 experimental campaign of  $UCN\tau$  [13].  $M_1$  through  $M_4$  are UCNs monitor detector. The setup from 2017 is a little bit different and is described in [28].

of 60-120 G to prevent any neutron depolarization. A 50 seconds period was used to clean the UCNs with  $E_n \gtrsim 38$  neV and the remaining neutrons were counted using a movable  $^{10}\text{B}$ -coated-ZnS scintillator. They reported a value of  $\tau_n^{UCN\tau} = 877.75 \pm 0.28^{+0.22}_{-0.16}$  seconds, achieving the lowest relative precision  $\lesssim 0.04\%$  in a neutron lifetime experiment.

### 1.2.3 The neutron lifetime discrepancy

#### Synthesis of the experimental results

All of these neutron lifetime experiments can be compiled to compute a weighted mean neutron lifetime value. Right now, the PDG averages eight results, all bottle experiments with UCNs, with a mean lifetime of  $\tau_n^{\text{PDG}} = 878.4 \pm 0.5$  seconds. Recent beam experiments are much less numerous than bottle experiments. Using only two values from [29] in 1996 and from [17] described above in 2013, the mean lifetime value from beam experiments is  $\tau_n^{\text{beam}} = 888.0 \pm 2.0$  seconds. There is a difference  $\Delta\tau_n = 9.6 \pm 2.1$  seconds between these two mean values. All values shown in Figure 1.8 are listed in Table 1.1. This  $\sim 1\%$  difference as shown in Figure 1.8 between beam and bottle mean values is known as the neutron lifetime discrepancy. The strong tension of  $\sim 4.5\sigma$  suggests the existence of a systematic effect that is not taken into account in either type of experiment.

#### Discussion on $\lambda$ and $V_{ud}$

This neutron lifetime discrepancy can also be seen from the eyes of the Standard Model. Equation 1.14 relates the neutron lifetime to  $|V_{ud}|$  and  $\lambda$ , two other fundamental parameters of the SM, briefly described in section 1.1.2. Today's most precise determination of  $|V_{ud}|$  comes from superallowed  $0^+ \rightarrow 0^+$  beta decays with [3] :

$$|V_{ud}|_{0^+ \rightarrow 0^+} = 0.97373 \pm 0.00031. \quad (1.26)$$

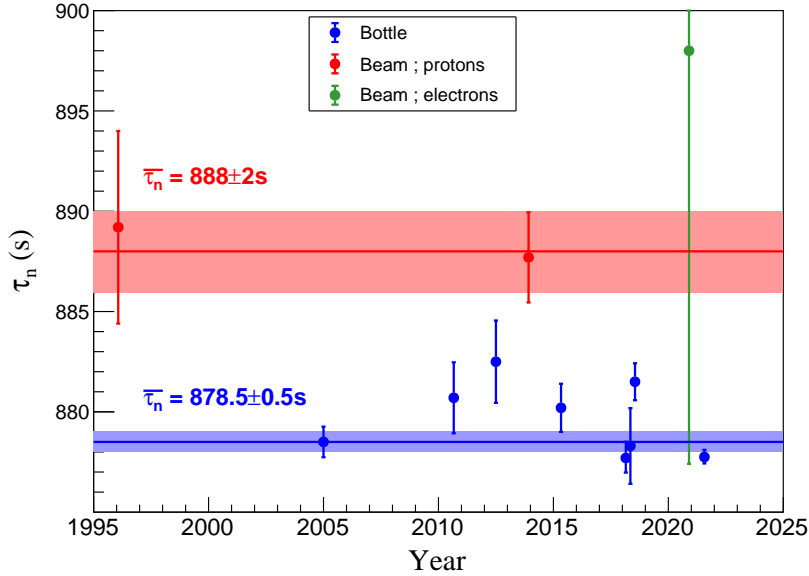


FIGURE 1.8 – The neutron lifetime discrepancy between beam and bottle mean lifetime values. The green point corresponds to a preliminary result from J-Parc [30] as discussed in Section 1.2.4. All bottle experiments appearing here are the ones taken into account in the latest PDG average.

For the axial-vector to vector ratio, the latest recommended value from the PDG is :

$$\lambda_{\text{PDG}} = -1.2754 \pm 0.0013. \quad (1.27)$$

This is a weighted mean value of several experiments that measure either the asymmetry or the angular correlation coefficients ( $A$  and  $a$ , respectively). All values used to compute  $\lambda_{\text{PDG}}$  are summarized in Table 1.2. We also provide a figure compiling these values in Appendix A. The plot illustrated in Figure 1.9 clearly shows that  $\lambda_{\text{PDG}}$  and  $|V_{ud}|_{0^+ \rightarrow 0^+}$  are in very good agreement with the actual mean value for the neutron lifetime.

However, this agreement can be challenged by questioning the validity of the values of  $\lambda$  and  $|V_{ud}|$ . All the values used to compute the actual  $\lambda_{\text{PDG}}$  are fairly evenly distributed between  $|\lambda| \approx 1.26$  and  $|\lambda| \approx 1.28$ . The most accurate determination of  $\lambda$  comes from the PERKEO III experiment with a reported value of  $\lambda = -1.27641 \pm 0.00045 \pm 0.00033$  [42] in 2019 and a level of precision  $\lesssim 0.045\%$ . This result is in line with 4 other values  $|\lambda| \gtrsim 1.275$  published after 2005. The 2020 result from the *ASPECT* spectrometer  $|\lambda| = 1.2677 \pm 0.0028$  [38] on the other hand, is better aligned with the remaining values  $|\lambda| \lesssim 1.27$ , all published before 2001. Using  $|V_{ud}|_{0^+ \rightarrow 0^+}$  as reference, it can be seen in Figure 1.10 that  $|\lambda| \lesssim 1.27$  values are in good agreement with  $\tau_n^{\text{beam}}$  whereas  $|\lambda| \gtrsim 1.27$  values show a better consistency with  $\tau_n^{\text{bottle}}$ .

Now, the discussion on  $|V_{ud}|$  is a bit different. As mentioned above, the value used in Figure 1.9 comes from the evaluation of  $\mathcal{F}t$  values in superallowed  $0^+ \rightarrow 0^+$   $\beta$  decays. It

Category	$\tau_n$ (s)	Comments	Ref.
Beam	$889.2 \pm 3.0 \pm 3.8$	Reevaluation of the NIST 1990 result [31]	[29]
	$887.7 \pm 1.2 \pm 1.9$	Reevaluation of the NIST 2005 result [15]	[17]
	$898 \pm 10_{-18}^{+15}$	JPARC preliminary result	[30]
Bottle	$878.5 \pm 0.7 \pm 0.3$	ILL gravitational trap	[26]
	$880.7 \pm 1.3 \pm 1.2$	ILL MAMBO2 material trap	[32]
	$882.5 \pm 1.4 \pm 1.5$	Reevaluation of the MAMBO1 1989 result [21]	[23]
	$880.2 \pm 1.2$	ILL material trap	[24]
	$881.5 \pm 0.7 \pm 0.6$	ILL gravitational trap	[27]
	$877.7 \pm 0.7_{-0.2}^{+0.4}$	Los Alamos Halbach array	[28]
	$878.3 \pm 1.6 \pm 1.0$	ILL magneto-gravitational trap	[33]
	$877.75 \pm 0.28_{-0.16}^{+0.22}$	Los Alamos UCN $\tau$	[13]

TABLE 1.1 – All neutron lifetime values used in Figure 1.8.

is assessed through Equation 1.9 which is also equals to :

$$\mathcal{F}t = \frac{K}{2G_F^2 |V_{ud}|^2 (1 + \Delta_V^R)}, \quad (1.28)$$

where  $K/(\hbar c)^6 = 2\pi^3 \hbar \ln 2 / (m_e c^2)^5$ . The average  $\bar{\mathcal{F}}t$  value has been very consistent for the last 30 years, leading to values of  $|V_{ud}|$  in the vicinity of 0.974 while the relative precision of  $\approx 0.1\%$  has improved to  $\approx 0.03\%$ . A recent nuclear charge radius measurement in  $^{26m}\text{Al}$  [44], one of the nuclei used in [3], challenged the accepted mean value of  $\bar{\mathcal{F}}t$  at the  $\mathcal{O}(10^{-4})$  level of precision, which makes it a good and different way to test future evaluations of  $|V_{ud}|$ .

The actual value of  $|V_{ud}|_{0^+ \rightarrow 0^+}$  is also in very good agreement with the nuclear structure independent  $\pi^+ \rightarrow \pi^0 e^+ \nu$  decay investigated by the PIBETA apparatus with a reported value of  $|V_{ud}|^{\text{PIBETA}} = 0.9728 \pm 0.0030$  in 2004 [45]. The main concern about  $|V_{ud}|$  is due to the existing  $2.2\sigma$  tension between  $|V_{ud}|^2 + |V_{us}|^2 + |V_{ub}|^2 = 0.9985 \pm 0.0007$  and the alleged unitarity of the CKM matrix. Addressing the discrepancy solely through  $|V_{ud}|$  would necessitate a value of approximately 0.9745 to resolve the tension. A value of  $|V_{ud}| \approx 0.971$  would be required to make it consistent with both  $\lambda_{\text{PDG}}$  and  $\tau_n^{\text{beam}}$ . However, such a difference toward a lower value seems very unlikely given the context.

Compiling these informations on  $\lambda$  and  $|V_{ud}|$  into the parameter space yields a rather different outcome than in Figure 1.9. The value  $|V_{ud}| \approx 0.9745$  required to achieve the unitarity of the CKM matrix and  $\lambda$  values from PERKEO III and aSPECT spectrometers have been added in Figure 1.10. Measurements with  $|\lambda| > 1.27$  are generally more recent, achieved a better level of precision than the other experiments, and are consistent with  $\tau_n^{\text{bottle}}$ . The remaining values clearly paint a different picture. Despite its precision being much lower than the PERKEO measurement, the  $\lambda^{\text{aSPECT}}$  result from 2020 remains compet-

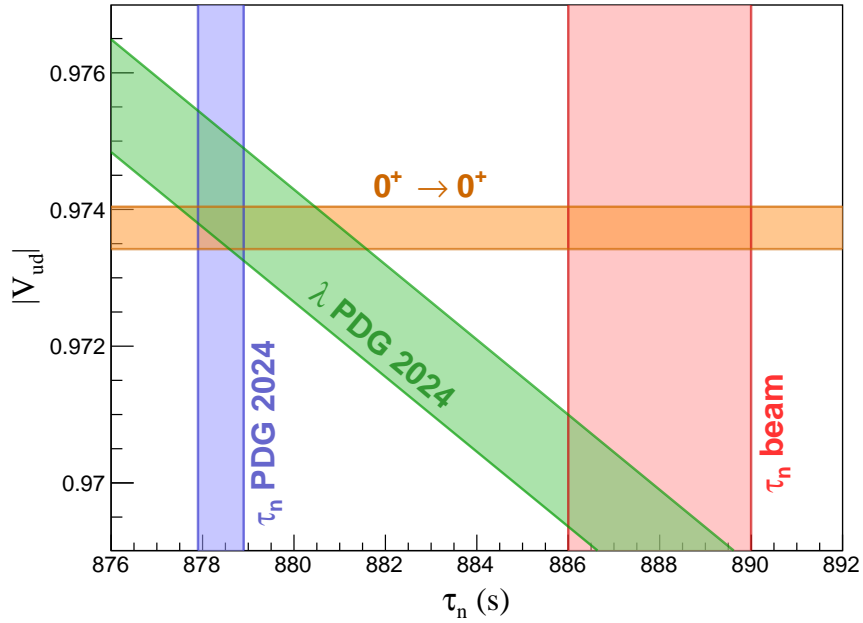


FIGURE 1.9 – The beam bottle discrepancy compared to the values of  $\lambda$  and  $|V_{ud}|$ , the other two main quantities needed to compute the theoretical value of the neutron lifetime. The actual most precise determination of  $V_{ud}$  and the PDG mean value of  $\lambda$  strongly disfavor the neutron lifetime from beam measurements.

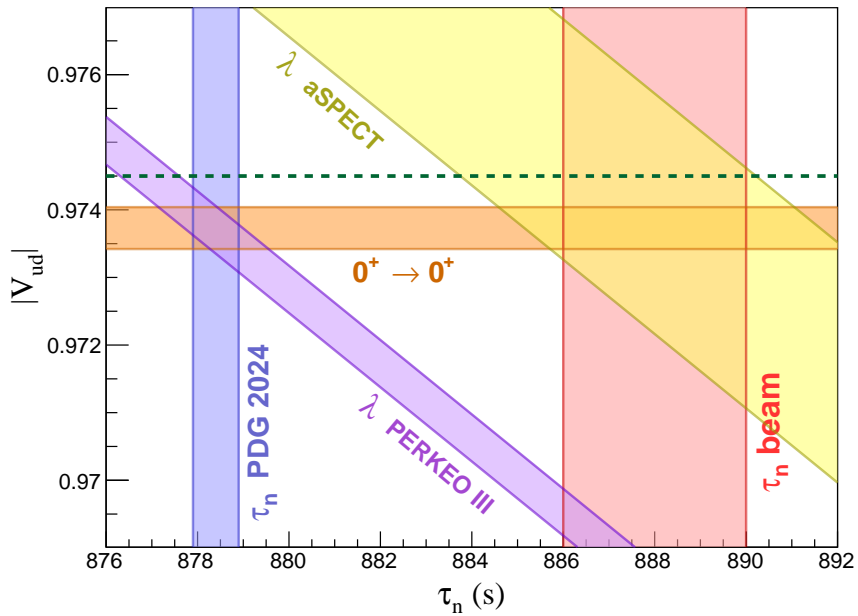


FIGURE 1.10 – The beam bottle discrepancy compared to the  $|V_{ud}|_{0^+ \rightarrow 0^+}$  as reference and  $\lambda$  values from the PERKEO III and aSPECT spectrometer. The dotted line shows the value required to achieve CKM unitarity through  $V_{ud}$  only.

	$\lambda$	$\Delta\lambda/\lambda(\%)$	Year	Ref.
	$-1.262 \pm 0.005$	0.39	1986	[34]
	$-1.2594 \pm 0.0038$	0.30	1997	[35]
$ \lambda  < 1.27$	$-1.266 \pm 0.004$	0.32	1997	[36]
	$-1.2686 \pm 0.0046 \pm 0.0007$	0.36	2001	[37]
	$-1.2677 \pm 0.0028$	0.22	2020	[38]
	$-1.275 \pm 0.006 \pm 0.015$	1.27	2008	[39]
	$-1.2748 \pm 0.0008^{+0.0010}_{-0.0011}$	0.11	2013	[40]
$ \lambda  > 1.27$	$-1.2772 \pm 0.0020$	0.16	2018	[41]
	$-1.27641 \pm 0.00045 \pm 0.00033$	0.04	2019	[42]
	$-1.2796 \pm 0.0062$	0.48	2021	[43]

TABLE 1.2 – All measurements of  $\lambda$  used to compute the actual PDG mean value.

itive compared to other  $|\lambda| > 1.27$  values and allows the possibility that  $\tau_n^{\text{beam}}$  represents the true neutron lifetime associated with the  $\beta$  decay process.

## 1.2.4 Other results and future lifetime experiments

### Space-based approach

Given the importance of the neutron lifetime, there is a clear need to further improve the accuracy of its determination and to solve the discrepancy between beam and bottle experiments. A recently highlighted but different approach, originally suggested by Feldman in 1990 [46], utilizes observations from space missions to determine the neutron lifetime. In this method, free neutrons produced by cosmic-ray spallation reactions around a planet atmosphere are observed with a spacecraft, and the neutron detection rate with respect to the distance between the planet and the spacecraft is used to assess the lifetime. A first

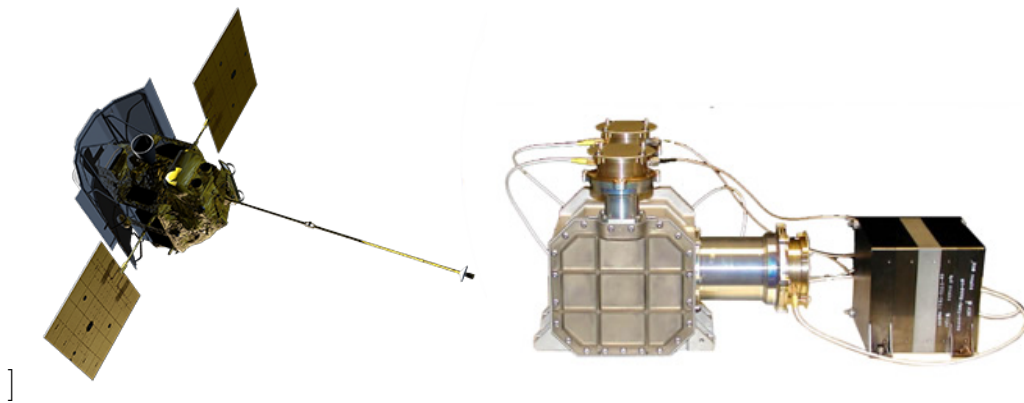


FIGURE 1.11 – LHS: NASA's MESSENGER spacecraft. RHS: The neutron spectrometer used to collect data during flybys of Venus and Mercury.

result using data from the neutron spectrometer on NASA’s MESSENGER mission during flybys of Venus and Mercury in 2007 and 2008 reported a lifetime of  $\tau_n^{\text{MESS}} = 780 \pm 60 \pm 70$  seconds in 2020 [47], demonstrating the feasibility of this approach. The spacecraft and the neutron spectrometer are shown in Figure 1.11. This result was directly followed by another one using data from the neutron spectrometer onboard NASA’s Lunar Prospector orbiting the Moon in 1998 with a reported lifetime of  $\tau_n^{\text{LP}} = 887 \pm 14 \begin{smallmatrix} +7 \\ -3 \end{smallmatrix}$  seconds [48]. Future space observations dedicated to measuring the neutron lifetime from Earth orbit, Venus orbit, or on the Moon surface should reduce both the statistical and systematic uncertainties to the 1s level, thus competing with laboratory experiments [49].

### Future lifetime experiments

Returning to Earth, many more experiments are planned in different facilities around the world to help clarify the situation. A beam experiment at J-PARC measuring both neutrons and electrons reported a preliminary result of  $\tau_n^{\text{J-PARC}} = 898 \pm 10 \begin{smallmatrix} +15 \\ -18 \end{smallmatrix}$  seconds using a pulsed neutron beam [30]. The apparatus has recently been updated to lower the uncertainty for a future experiment to the 0.1% level [50]. An improved cold neutron beam experiment, called BL3, is also on the way at the NIST facility, aiming to improve and better control every aspect of the 2005 experiment to reach a precision of  $\sim 0.3$  s [51]. A hybrid beam-bottle experiment, called UCNProBe and currently in development at Los Alamos, aims to monitor both the number of neutrons and the number of electrons (emitted from neutron  $\beta$  decay) within the bottle [52]. A paper demonstrating the ability of a YAP:Ce scintillator to monitor the population of UCNs was recently published [53]. Finally, another bottle experiment named  $\tau$ SPECT, using a three-dimensional magnetic field gradient to trap UCNs, reported a preliminary result of  $\tau_n^{\tau\text{SPECT}} = 859(16)$  seconds [54]. Both the UCNProBe and  $\tau$ SPECT experiments aspire to improve and achieve a precision level of 0.3 s in their future results.

## 1.3 Summary

Measuring an accurate value of the neutron lifetime has been an ongoing quest for the past 30 years or so and remains at the heart of many discussions in fundamental physics. The two primary methods for measuring the neutron lifetime are known as the bottle method and the beam method. The bottle method involves confining ultracold neutrons in a trap and counting how many have survived after a certain amount of time. The beam method, on the other hand, involves passing a beam of cold neutrons through a defined volume and detecting the decay products. These methods yield results with a slight difference at the 1% level, often referred to as the neutron lifetime discrepancy.

Moreover, if the neutron lifetime predicted by the SM seems to align with the bottle result, we have seen in this chapter that the internal disagreement between  $\lambda$  measurements and the discussion on  $V_{ud}$  can paint a different picture, favoring the beam result. The situation on the neutron lifetime should be clarified as many experiments with innovative and complementary approaches are planned in the near future.

# Chapter 2

## Attempts at resolving the discrepancy

This long-standing 1% discrepancy with a tension at the level of  $4.5\sigma$  between the lifetimes of the beam and the bottle experiments has not yet found an explanation. Assuming that this divergence is not caused by any overlooked systematic effects in the experimental design or data analysis, its origin must lie at a more fundamental level. In this chapter, we review different effects that could alter the measurement of the neutron lifetime and therefore be potential solutions to the discrepancy between beam and bottle experiments.

### Contents

---

<b>2.1 Beyond experimental effects</b>	<b>22</b>
2.1.1 Radiative and bound-state $\beta$ decay	22
2.1.2 Mirror oscillations of free neutrons	23
2.1.3 Soft scattering between neutrons and dark matter	24
2.1.4 Existence of a neutron excited state	24
<b>2.2 The neutron dark decay</b>	<b>25</b>
2.2.1 Open mass range	26
2.2.2 Effective Lagrangians and decay rates	27
2.2.3 Investigations of the $n \rightarrow \chi\gamma$ and $n \rightarrow \chi e^+ e^-$ decays	28
2.2.4 Neutron stars	29
<b>2.3 Nuclear dark decays</b>	<b>31</b>
2.3.1 Dark decay in $^{11}\text{Li}$ , $^{11}\text{Be}$ , $^{15}\text{C}$ and $^{17}\text{C}$	32
2.3.2 Discussing the $^{17}\text{C}$ case	33
2.3.3 Dark decay in $^6\text{He}$	34
<b>2.4 Summary</b>	<b>35</b>

---

## 2.1 Beyond experimental effects

The neutron lifetime discrepancy has triggered many different debates within the physics community in an effort to resolve the problem. As discussed in the previous chapter, some neutron lifetime experiments stand in a cross-fire between criticisms from the community and reevaluations of their past result. Experimentally speaking, neutrons are difficult to handle with probably many undermined technical effects. Improving our understanding of these effects is crucial, especially in a context where experiments are required to fulfill the constantly growing need for better precision levels. However, most of the debate does not actually focus on such problems. In fact, many discussions sparked by the discrepancy are actually about searching for new physical processes involving free neutrons, either in the confines of the Standard Model or beyond.

Right now, beam experiments are only sensitive to charged particles emitted after a  $\beta$  decay, whereas bottle experiments are sensitive to any neutron vanishing mechanism inside the trap. Therefore, discussions involving new neutron physics in the literature usually try to solve the discrepancy by considering either  $\tau_n = \tau^{\text{bottle}}$  or  $\tau_n = \tau^{\text{beam}}$  and introducing a new process to explain the difference from its counterpart.

### 2.1.1 Radiative and bound-state $\beta$ decay

#### Radiative $\beta$ decay

Particular aspects of neutron  $\beta$  decay are its radiative and bound version. In a radiative  $\beta$  decay, a photon is also emitted in the final state like :

$$n \rightarrow p + e^- + \bar{\nu}_e + \gamma \quad (2.1)$$

where the photon mainly comes from electron bremsstrahlung. This specific decay channel was thoroughly investigated in 2016 in an experiment at NIST [55]. The experiment covered a wide energy range between 0.4 keV and  $Q_\beta = 782$  keV and measured a total branching ratio  $\approx 1\%$  for this radiative mode. Even though the branching ratio is compatible with the actual neutron lifetime discrepancy, this decay mode is not responsible for it. In principle, an additional  $\gamma$  in the final state should not cause problems in any of the beam or bottle experiments.

#### Bound-state $\beta$ decay

In a bound-state  $\beta$  decay, the electron is not emitted into the continuum, but rather directly into an atomic orbital of the daughter nucleus. This exotic decay mode was first conceptualized in 1947 by R. Daudel [56], suggesting that the electron is not produced with sufficient energy to escape the attracting field of the nucleus. Following this idea, it was proposed in 1951 by S. G. Cohen [57] that such a process could also occur in free neutron decays like :

$$n \rightarrow \text{H}\bar{\nu}_e, \quad (2.2)$$

where the electron is located inside the K-shell of the hydrogen nucleus. This process is also called the neutron two-body decay. Cohen estimated the branching ratio for this decay mode to be  $6 \times 10^{-6}$  and later presented this idea as a potential way to probe the mass of the neutrino [58]. In 2009, a more sophisticated theoretical evaluation of this branching ratio was given with a value  $\approx 4 \times 10^{-6}$ , in good agreement with Cohen's work [59], but far below the actual neutron lifetime discrepancy. Despite being proposed nearly 80 years ago, experimental studies on bound-state  $\beta$  decay are relatively scarce. The first observation of this process was reported in 1992 in fully ionized  $^{163}_{66}\text{Dy}^{66+}$  nuclei [60]. It was also observed in  $^{187}_{75}\text{Re}^{75+}$  [61] and in  $^{205}_{81}\text{Tl}^{81+}$  [62].

An article published in 2024 investigated the impact of taking into account the second solution of the Dirac equation for the hydrogen atom in the calculation of the branching ratio [63]. These emitted atoms are usually called the Second Flavor of Hydrogen Atoms (SFHA) and supposedly remain dark, as they do not emit or absorb any electromagnetic radiation. The author in this article calculated a final probability that is increased by a factor of 3300 compared to previous calculations. This results in a branching ratio of  $\text{Br}_{b\beta} = (1.15 \pm 0.27)\%$ ; in good agreement with the actual neutron lifetime discrepancy.

On the experimental side, some designs have been suggested in the past two decades to detect hydrogen atoms resulting from the decay of free neutrons, but they have yet to be realized [64, 65, 66]. If bound-state  $\beta$  decays can occur in free neutrons, it should impact beam experiments that rely on the detection of charged particles to measure the neutron lifetime. If a bound state  $\beta$  decay is observed in a future experiment, it should resolve only a small fraction of the actual beam-bottle discrepancy, as the proposed SFHA cannot be detected.

### 2.1.2 Mirror oscillations of free neutrons

Neutron mirror oscillations refer to a hypothetical phenomenon in which neutrons can oscillate between their ordinary state  $n$  and a mirror state  $n'$ . This concept suggests the existence of a parallel sector of mirror particles that can interact through gravity with our ordinary matter [67]. It also provides a description of a mixing mechanism for neutral particles such as free neutrons with their mirror partner [68]. The strength of the interaction is known as the mixing angle  $\theta_m$  and spontaneous mirror oscillations could occur for nondegenerate mass partners such as :

$$m_n = m_{n'} + \Delta m, \quad (2.3)$$

where  $|\Delta m|$  is usually estimated to be in the 1-100 neV range. If an ordinary neutron oscillates into its mirror counterpart, it is therefore no longer detectable. Moreover, mirror neutrons could also decay like  $n' \rightarrow p'e'\bar{\nu}_e'$ .

The neutron lifetime discrepancy could therefore be the result of different behaviors of the mirror oscillation rate with respect to each beam and bottle experimental setup [69, 70, 71]. It could also be responsible for a potential discrepancy within bottle experiments between material and magnetic traps, as suggested in [71]. A direct experimental search for mirror oscillations in a 6.6 T magnetic field excluded the presence of mirror oscillations

for  $|\Delta m| \gtrsim 10$  neV [72], severely constraining this model in both beam and magnetic bottle experiments.

### 2.1.3 Soft scattering between neutrons and dark matter

Another way proposed in 2021 to solve the lifetime discrepancy considers a potential new interaction between neutrons and dark matter [73]. In this model, the authors assume the existence of a dark gauge vector particle  $A$  to which neutrons can couple through a dark electric dipole moment. In this scenario, GeV-scale dark matter could be able to transfer kinetic energy  $E_{\text{trans}} > 50$  neV to neutrons through a soft scattering process.

This effect would primarily play a role in bottle experiments, where UCNs are confined due to a potential of the order of 50-100 neV. The additional kinetic energy obtained through the scattering process allows the UCNs to escape the bottle, increasing the observed vanishing rate of the population inside the trap and resulting in a shorter lifetime.

### 2.1.4 Existence of a neutron excited state

Recently, it has been suggested that the beam bottle discrepancy might be resolved by the presence of an excited state in free neutrons [74]. In this scenario, neutrons in the excited state can release the energy either through an electromagnetic transition by  $\gamma$  emission to the ground state with a lifetime  $\tau_\gamma$  as  $n^* \rightarrow n\gamma$ , or as additional energy during the  $\beta$  decay  $n^* \rightarrow pe^-\bar{\nu}_e$  with a lifetime  $\tau_e$ . In this model, the  $\beta$  decay from the ground state is done with a lifetime  $\tau_g$ . If the lifetime of this excited state is long enough, it could play a role in the beam bottle discrepancy with respect to their experimental design.

Neutrons in beam experiments are usually detected shortly after their production in  $t_{\text{beam}} \approx 25$  ms. On the other hand, neutron monitoring in bottle experiments is usually

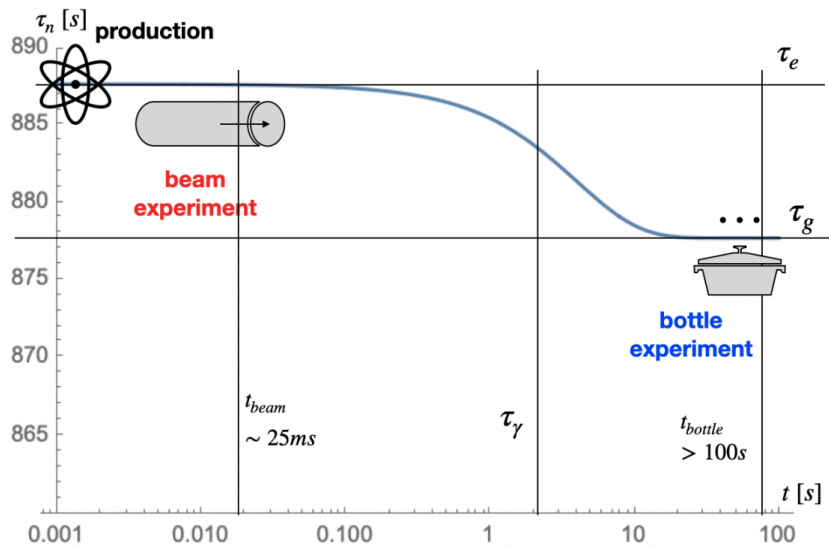


FIGURE 2.1 – Evolution of the observed neutron lifetime with respect to the time after neutron production. In this image, taken from [74], the authors assumed  $\tau_\gamma = 4$ s and that all neutrons at  $t = 0$  are in the excited state.

performed after a certain time  $t_{\text{bottle}} \gtrsim 100$  s, which is used to moderate and clean the neutron population after its production. If the following hierarchy is established :

$$t_{\text{beam}} \ll \tau_{\gamma} \ll t_{\text{bottle}} < \tau_g < \tau_e, \quad (2.4)$$

and if neutrons can populate both the ground state and the excited state after their production in beam and bottle experiments, then the cleaning time  $t_{\text{bottle}}$  could account for the shorter lifetime in bottle experiments as illustrated in Figure 2.1. This hypothesis was recently tested in [75] where data from the UCN $\tau$  experiment [13] was reanalysed, but found no evidence of a neutron excited state with  $t_{\gamma} \geq 139$ s with a 95% confidence level.

## 2.2 The neutron dark decay

To reconcile the beam and bottle lifetimes, Fornal and Grinstein proposed in 2018 that neutrons could have new decay channels that do not involve a proton in the final state [76]. This framework assumes that the correct neutron lifetime is the one computed with bottle results and interpret the beam value as a correct but partial lifetime associated with the neutron  $\beta$  decay. Therefore, the new decays should have a combined branching ratio compatible with the actual lifetime discrepancy :

$$\sum \text{Br}(n \rightarrow p) \lesssim 1\%. \quad (2.5)$$

The proposed decay channels are as follows :

$$n \rightarrow \chi\gamma, \quad n \rightarrow \chi e^+ e^-, \quad n \rightarrow \chi\phi, \quad (2.6)$$

where  $\chi$  is a dark fermion and  $\phi$  a light dark scalar. In an effective picture, these dark decays are the result of a mass mixing process between the neutron and the dark fermion. In the case of the third decay scenario  $n \rightarrow \chi\phi$ , mass mixing would first occur with an intermediate dark fermion  $\tilde{\chi}$ . The effective Lagrangian behind this process can be written as :

$$\mathcal{L}_{\text{eff}} = \varepsilon (\bar{n}\chi' + \tilde{\chi}'n), \quad (2.7)$$

where  $\varepsilon$  is the mass mixing term with dimension of mass and  $\chi'$  is either the intermediate or final state dark fermion. In the first proposed decay, the emission of a monoenergetic photon is made possible by coupling the neutron magnetic moment to the electromagnetic field. These scenarios are open under one model-independent condition : the stability of nuclei, which as we will see later, also encompasses the stability of the free proton. Unless stated otherwise, most of the following discussions and equations regarding the dark decay model can be found in the following references [76, 77, 78].

## 2.2.1 Open mass range

### Stability of ${}^9\text{Be}$

The condition of nuclear stability limits the total mass of the products  $m_f$  emitted in these new scenarios. It is an energy condition that ensures that a neutron inside a nucleus can undergo a dark decay only if the reaction is exothermic :

$$m_n - S_n < m_f < m_n, \quad (2.8)$$

where  $m_n = 939.565$  MeV is the mass of a neutron and  $S_n$  is the neutron separation energy for a specific nucleus. The stable nucleus with the lowest  $S_n$  value is  ${}^9\text{Be}$  with  $S_n({}^9\text{Be}) = 1.664$  MeV. Taking one neutron out of  ${}^9\text{Be}$  would lead to the creation of  ${}^8\text{Be}$  which is an unbound system corresponding to a  $2\alpha$  resonance. The impossible decay  ${}^9\text{Be} \rightarrow \alpha\alpha f$ , where  $f$  are the particles emitted after a neutron dark decay, further constrains Equation 2.8 by 93 keV which becomes :

$$937.993 \text{ MeV} < m_f < 939.565 \text{ MeV}. \quad (2.9)$$

This inequality was first written  $937.900 \text{ MeV} < m_f$  in the original publication by Fornal and Grinstein considering the dark decay not available  ${}^9\text{Be} \rightarrow {}^8\text{Be}f$ . Some references in this chapter used this condition before the 93 keV adjustment proposed by Pfützner and Riisager [79]. In this manuscript, we will align with the latter and stronger constraint.

### Proton and dark matter stability

The open mass range in Equation 2.8 is compatible with the stability of the proton. Indeed, assuming that a proton could also go through a dark decay like  $p \rightarrow fe^+\nu$  would require  $m_f < m_p - m_e = 937.761$  MeV which is smaller than the lower bound in Equation 2.9 and therefore not permitted. Finally, the fermion  $\chi$  and the scalar  $\phi$  in the final state can be viable dark matter candidates by making them stable against the following  $\beta$  decay  $\chi \rightarrow pe^-\nu$ . This condition is written in a slightly different manner according to the dark decay scenario. In the  $n \rightarrow \chi\gamma$  decay, one simply needs  $m_\chi < m_p + m_e$ , while in the case of  $n \rightarrow \chi\phi$ , this condition can be written as  $|m_\chi - m_\phi| < m_p + m_e$ . Both lead to the same upper limit at  $m_p + m_e = 938.783$  MeV.

The open mass range equations for the dark particles following both the stability of nuclei and dark matter conditions are :

$$937.993 \text{ MeV} < m_\chi < 938.783 \text{ MeV}, \quad (2.10)$$

for the  $n \rightarrow \chi\gamma$  and the  $n \rightarrow \chi e^+e^-$  channels and

$$937.993 \text{ MeV} < m_\chi + m_\phi < 939.565 \text{ MeV} \quad \text{with} \quad |m_\chi - m_\phi| < 938.783 \text{ MeV}, \quad (2.11)$$

for the  $n \rightarrow \chi\phi$  decay.

### Available energy for the $\gamma$ and $e^+e^-$ pair

These mass ranges for dark particles can now be used to set constraints on the  $\gamma$  and the  $e^+e^-$  pair emitted in the corresponding dark decay channels. Combining Equations 2.9 and 2.10, we can deduce the energy range for the  $\gamma$  :

$$0.782 \text{ MeV} < E_\gamma < 1.572 \text{ MeV}. \quad (2.12)$$

For the  $e^+e^-$  pair, this equation becomes :

$$1.022 \text{ MeV} < E_{e^+e^-} < 1.572 \text{ MeV}, \quad (2.13)$$

which, in a classical approach, can be written like  $E_{e^+e^-} = 2m_e + T_{e^+e^-}$ , where  $T_{e^+e^-}$  is the total kinetic energy of the  $e^+e^-$  pair that should not exceed 550 keV. It is also important to note that in the  $n \rightarrow \chi\phi$  channel, there is no specific mass hierarchy to respect. One could have  $m_\phi \ll m_\chi$ ,  $m_\phi \approx m_\chi$  or any other combinations consistent with Equation 2.10 whereas, in the other channels, we must have  $m_\chi \lesssim m_n$ .

## 2.2.2 Effective Lagrangians and decay rates

### Dark fermion + Gamma

The decay channel  $n \rightarrow \chi\gamma$  can be described by an effective Lagrangian containing the mass mixing interaction from Equation 2.7 and the neutron magnetic moment :

$$\mathcal{L}_I^{\text{eff}} = \bar{n} \left( i\not{\partial} - m_n + \frac{g_n e}{8m_n} \sigma^{\mu\nu} F_{\mu\nu} \right) n + \bar{\chi}(i\not{\partial} - m_\chi)\chi + \varepsilon(\bar{n}\chi + \bar{\chi}n), \quad (2.14)$$

where  $g_n$  is the neutron g-factor,  $\sigma^{\mu\nu} = i/2[\gamma^\mu, \gamma^\nu]$  with the Dirac gamma matrices  $\gamma^i$  ( $i = 0, 1, 2, 3$ ) and  $F_{\mu\nu}$  is the electromagnetic field tensor. A tree level Feynman diagram of this process is shown in Figure 2.2. The dark decay rate for this channel can be written like :

$$\Gamma_{n \rightarrow \chi\gamma} = \frac{g_n^2 e^2}{128\pi} \left( 1 - \frac{m_\chi^2}{m_n^2} \right)^3 \left( \frac{\varepsilon}{m_n - m_\chi} \right)^2 m_n. \quad (2.15)$$

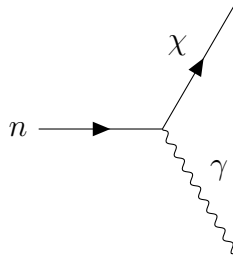


FIGURE 2.2 – Feynman diagram of the decay  $n \rightarrow \chi\gamma$ .

### Dark fermion + Dark scalar

A tree level Feynman diagram of the  $n \rightarrow \chi\phi$  channel is shown in Figure 2.3. The effective Lagrangian for this process can be written using  $\mathcal{L}_I^{\text{eff}}$  with the mass mixing process occurring with the intermediate dark fermion  $\tilde{\chi}$  later decaying into  $\chi$  and  $\phi$  :

$$\mathcal{L}_{II}^{\text{eff}} = \mathcal{L}_I^{\text{eff}}(\chi \rightarrow \tilde{\chi}) + (\lambda_\phi \tilde{\chi} \chi \phi + \text{h.c.}) + \tilde{\chi}(i\not{\partial} - m_\chi)\chi + \partial_\mu \phi^* \partial^\mu \phi - m_\phi^2 |\phi|^2, \quad (2.16)$$

where  $\lambda_\phi$  is the coupling between  $\tilde{\chi}$ ,  $\chi$  and  $\phi$ . This yields the following decay rate :

$$\Gamma_{n \rightarrow \chi\phi} = \frac{|\lambda_\phi|^2}{16\pi} \sqrt{[(1+x)^2 - y^2][(1-x)^2 - y^2]^3} \left( \frac{\varepsilon}{m_n - m_{\tilde{\chi}}} \right)^2 m_n, \quad (2.17)$$

where  $x = m_\chi/m_n$  and  $y = m_\phi/m_n$ . We provide a step-by-step demonstration on how to achieve this last decay rate in Appendix B.

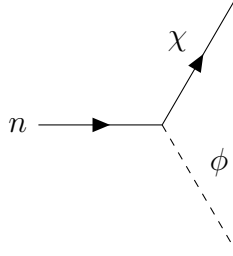


FIGURE 2.3 – Feynman diagram of the decay  $n \rightarrow \chi\phi$ .

### 2.2.3 Investigations of the $n \rightarrow \chi\gamma$ and $n \rightarrow \chi e^+ e^-$ decays

The energy conditions given previously provide a clear signature with typical SM particles that can be used to probe two out of the three proposed decay scenarios in a free neutron decay experiment. In the same year following the release of [76], two experiments looking for the emission of a  $\gamma$  or a  $e^+e^-$  pair published severe constraints on both dark decays. The first corresponds to an experiment performed at the Los Alamos UCN facility and was looking for the emission of a monoenergetic  $\gamma$  ray from the decay of UCNs trapped inside a nickel-phosphorous-coated bottle [80] located upstream of the UCN $\tau$  Halbach array [13]. A lead shielded, Compton-scattering-suppressed HPGGe detector was used to monitor the emission of any  $\gamma$  rays in the  $0.782 \text{ MeV} < E_\gamma < 1.664 \text{ MeV}$  range, compatible with  $\chi$  being a dark matter candidate. Their findings showed to be conflicting with the 1% required to solve the neutron lifetime anomaly, excluding the  $n \rightarrow \chi\gamma$  decay as a solution to the beam-bottle discrepancy with a 97% confidence level.

Shortly after, the Ultracold Neutron Asymmetry (UCNA) collaboration published an article investigating the  $n \rightarrow \chi e^+ e^-$  decay mode [81]. The apparatus, first designed to measure the neutron  $\beta$  asymmetry parameter, can also be used to look for the emission of a  $e^+e^-$  pair following a neutron dark decay. Using data from an experimental campaign carried out in 2012-2013, they also excluded the  $n \rightarrow \chi e^+ e^-$  decay as a solution to the neutron lifetime discrepancy for  $(E_{e^+e^-} - 2m_e) \gtrsim 100 \text{ keV}$ . A third paper, further con-

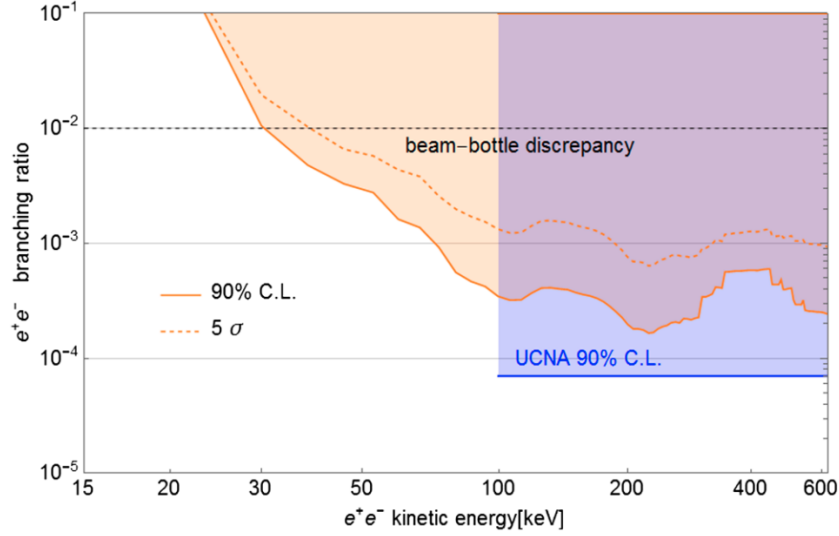


FIGURE 2.4 – Exclusion diagram for the  $n \rightarrow \chi e^+ e^-$  channel from the PERKEO publication [82]. Exclusion zones from UCNA [81] and PERKEO II are displayed in blue and beige respectively. The horizontal grey dotted line correspond to the actual beam-bottle discrepancy.

straining the  $n \rightarrow \chi e^+ e^-$  decay was published about a year later [82]. Data collected by the PERKEO II experiment, also designed to measure the neutron  $\beta$  asymmetry parameter, were used again to look for the signature  $e^+ e^-$  pair. Their analysis gave results consistent with UCNA, extending their constraint for  $(E_{e^+ e^-} - 2m_e) \gtrsim 30$  keV as shown in Figure 2.4. There is still a small  $\sim 30$  keV window left unprobed by both experiments, but it seems very unlikely that it contains the whole dark decay.

Both of these investigated dark decay scenarios were experimentally proven to be inconsistent with the actual neutron lifetime discrepancy, reaching levels of  $\mathcal{O}(10^{-4})$  for the open dark branching ratio. The only remaining option to reconcile the dark decay model with the beam-bottle discrepancy is the  $n \rightarrow \chi \phi$  decay. This branch contains only undetectable particles in the final state. Therefore, it can not be probed in a free neutron decay experiment similarly to the two other decays. However, alternative approaches can be used to test the dark decay model, including the remaining  $n \rightarrow \chi \phi$  decay. Investigating the effects of dark decays in different systems, such as neutron stars or radioactive nuclei, can serve as a viable strategy to validate or refute the model.

## 2.2.4 Neutron stars

A relevant discussion questioning the validity of the dark decay hypothesis comes from the study of neutron stars. This approach does not directly investigate the proposed decays by trying to observe an emitted SM particle, but rather looks for the consequences that a neutron dark decay would lead to in these stellar objects. Neutron stars are remnants of massive supergiant stars that have undergone supernova explosions. As their name suggests, neutron stars are predominantly composed of neutrons, but they also contain a significant presence of ions and electrons. These objects are extremely dense, with

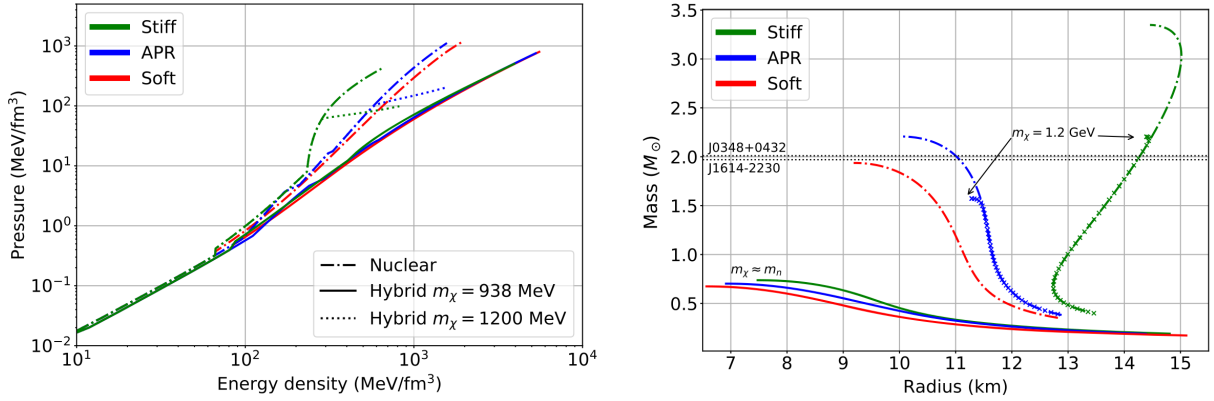


FIGURE 2.5 – LHS : Standard (APR) and boundary (Stiff and Soft) EoS. The dash-dotted curves contains only standard nuclear matter whereas a dark fermion with  $m_\chi = 938$  MeV or  $m_\chi = 1200$  MeV have been added in solid and dotted curves respectively. RHS : The mass-radius distribution obtained from the EoS shown on the LHS. EoS with  $m_\chi = 938$  MeV completely fails to reproduce neutron stars with a  $2M_\odot$  mass. Both images are from [85].

masses on the order of  $\sim \mathcal{O}(M_\odot)$  confined within a sphere with a radius of about 10 kilometers. A major interest in neutron star research is to correctly model the relationship between the pressure  $P$  and the energy density  $\varepsilon$ . This  $P(\varepsilon)$  relationship is known as the equation of state (EoS) and is still an active field of research today. There are many different EoS models, all with their own intricacies, which will not be discussed here. Once an EoS is established, it can be used to compute its associated theoretical (Mass – Radius) distribution of neutron stars. This is done by numerically solving the Tolman-Oppenheimer-Volkoff (TOV) set of relativistic equations of hydrostatic equilibrium [83, 84].

Shortly after the publication of Fornal and Grinstein, a paper investigating the effect of a neutron dark decay in neutron stars was released [85]. They used the APR model [86] (named after Akmal, Pandharipande and Ravenhall) as an EoS of reference and used two other EoS (namely, "soft" and "stiff") that served as boundary scenarios in line with the knowledge of uncertainties in nuclear interactions at the time of publication. These three EoS were then used to compute their corresponding (Mass – Radius) distributions, all capable of reproducing neutron stars with  $M_{\text{NS}} \approx 2M_\odot$  as shown in Figure 2.5. This mass of  $2M_\odot$  is in agreement with some of the heaviest known neutron stars in 2018 [87] with accurately established masses such as the J0348+0432 system ( $M = 2.01 \pm 0.04 M_\odot$  [88]) and the J1614-2230 ( $M = 1.908 \pm 0.016 M_\odot$  [89]). Taking into account the emission of a dark fermion  $\chi$  with a  $\chi - n$  coupling compatible with the neutron lifetime discrepancy and  $m_\chi \lesssim m_n$  strongly softens the EoS. It also fails to reproduce neutron stars with  $M \approx 2M_\odot$ , with predictions in the range  $0.65 \lesssim M_{\text{NS}}^{\text{max}} \lesssim 0.75$  solar mass. This result nearly ruled out the dark decay as a standalone model to explain the neutron lifetime discrepancy, but was followed by many other papers trying to reconcile the dark decay idea with neutron stars.

To align the dark decay with neutron stars, the community proposed to change and/or add ingredients to the model. Some investigated the effect of adding a repulsive dark

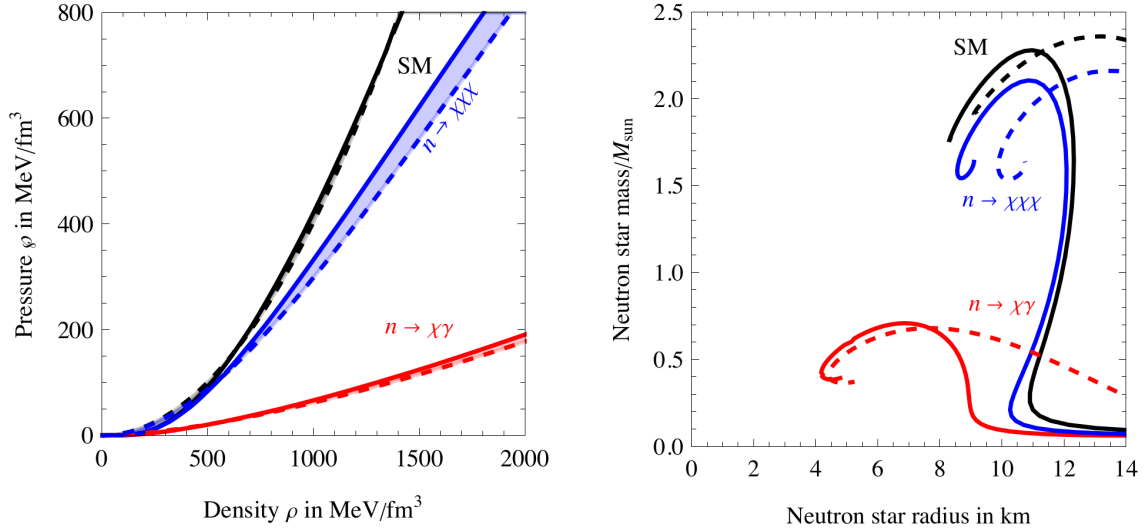


FIGURE 2.6 – LHS : EoS for standard nuclear matter in black, with  $n \rightarrow \chi\gamma$  in red and with  $n \rightarrow \chi\chi\chi$  in blue. The solid and dashed curves correspond to two different model of EoS. RHS : The mass-radius distribution for each EoS. Red lines agree nicely with the results from [85] and blue lines are able to produce neutron stars with  $2M_{\odot}$ . Both figures are from [90].

matter self-interaction or repulsive interaction between dark matter and neutrons inside the star [91, 92, 93]. Taking these interactions into account in the EoS allows to generate neutron stars with  $2M_{\odot}$ , hence reconciling the dark decay model with these stellar objects. A modified neutron dark decay was also proposed, with 3 dark fermions in the final state like :  $n \rightarrow \chi\chi\chi$  with  $m_{\chi} \approx m_n/3$  [90]. This different channel was able to reproduce neutron stars with  $2M_{\odot}$  without additional interactions, as shown in Figure 2.6. Other papers also investigated different aspects such as the presence of a dark photon in the final state [94] or the impact of dark decays on the temperature and rotational speed of neutron stars [95]. Although neutron stars are considered valuable tools for investigating dark sectors [96], they currently do not provide conclusive evidence against the neutron dark decay model.

## 2.3 Nuclear dark decays

In the original paper proposing the dark decay model [76], it was suggested that such exotic processes could also be investigated in weakly bound radioactive nuclei with  $S_n < 1.665$  MeV. Fornal and Grinstein first brought forward the  $^{11}\text{Li}$  nucleus with  $S_n(^{11}\text{Li}) = 0.396$  MeV considering the following decay chain  $^{11}\text{Li} \rightarrow ^{10}\text{Li} + \chi \rightarrow ^9\text{Li} + n + \chi$  [76]. The idea of dark decays in radioactive nuclei was then further developed by Pfützner and Riisager [79]. They first proposed the 93 keV stronger constraint on  $S_n$  in Equation 2.9. The upper limit on  $S_n$  then moved from  $S_n < 1.664$  MeV to  $S_n < 1.572$  MeV to allow the occurrence of dark decays in radioactive nuclei. Then, they provided a list of 5 nuclei in agreement with  $S_n < 1.572$  MeV :  $^6\text{He}$ ,  $^{11}\text{Be}$ ,  $^{15}\text{C}$ ,  $^{17}\text{C}$  and the already proposed  $^{11}\text{Li}$ .

### 2.3.1 Dark decay in $^{11}\text{Li}$ , $^{11}\text{Be}$ , $^{15}\text{C}$ and $^{17}\text{C}$

The discussion about nuclear dark decays is based on finding a candidate with sufficiently low  $S_{n/2n}$  value, preferably  $\lesssim 0.782$  MeV to probe the entire mass range for  $m_\chi$  (see Equation 2.10), while giving a clear and unique signature that a dark decay has occurred. The four nuclei mentioned here are potential candidates proposed to investigate the dark decay model. Unfortunately, discussions in [79] have shown that it would be impractical to use them or that they would probe too little of the open mass range. We review here the causes behind this case. For each candidate, the maximum branching ratio for the dark decay was estimated in [79] simply through :  $\text{Br}_\chi = t_{1/2}^{(i)}/t_{1/2}^{n\chi}$ , where  $t_{1/2}^{(i)}$  is the half-life of the  $i$ -th nucleus and  $t_{1/2}^{n\chi}$  is the partial half-life of the free neutron dark decay.

**$^{11}\text{Li}$**  A dark decay in this nucleus would be such that :  $^{11}\text{Li} \rightarrow ^9\text{Li} + n + \chi$  (as  $^{10}\text{Li}$  is an unbound system) with  $S_{2n}(^{11}\text{Li}) = 369.3(6)$  keV and an estimated branching ratio upper limit  $\approx 10^{-7}$ . The low  $S_{2n}$  value allows this decay to probe the entire mass range for  $\chi$  to be a DM particle. Unfortunately, other decay channels could lead to the creation of the same particles in the final state. Indeed,  $\beta n$  and  $\beta d$  decay leading to the emission of a neutron or the production of  $^9\text{Li}$  respectively are already possible from the  $^{11}\text{Li}$  ground state. Also, the open but unobserved yet  $\beta p$  decay channel would result in the emission of both a  $^9\text{Li}$  nucleus and a free neutron, just like the dark decay. Therefore, experimenting with  $^{11}\text{Li}$  would require disentangling all decay channels, making it very difficult to isolate and observe the potential dark decay.

**$^{11}\text{Be}$**  Here, the dark decay can be written like :  $^{11}\text{Be} \rightarrow ^{10}\text{Be} + \chi$  and has an estimated branching ratio upper limit at  $\approx 10^{-4}$ . As with  $^{11}\text{Li}$ , the first neutron separation energy  $S_n(^{11}\text{Be}) = 501.6(3)$  keV allows to probe 100% of the open  $m_\chi$  range for  $\chi$  to be a DM particle. Detecting  $^{10}\text{Be}$  nuclei correlated with the decay of a  $^{11}\text{Be}$  population could have made this nucleus a very interesting candidate to test the neutron dark decay. Unfortunately, the small  $8.3(9) \times 10^{-6}$   $\beta p$  decay channel also feeds the production of  $^{10}\text{Be}$  nuclei [97]. Although not as complex as with  $^{11}\text{Li}$ , isolating the dark decay channel with great accuracy from  $\beta p$  channel would remain a difficult task.

**$^{15}\text{C}$**  Similarly to  $^{11}\text{Be}$ , a dark decay in  $^{15}\text{C}$  would be like :  $^{15}\text{C} \rightarrow ^{14}\text{C} + \chi$ . The upper limit for this decay is estimated at  $\approx 10^{-5}$ .  $^{15}\text{C}$  only has multiple but simple  $\beta$  decay channels open, all feeding either the ground state of the stable nucleus  $^{15}\text{N}$  or some of its excited states. The proton emission threshold  $S_p(^{15}\text{N}) = 21.08(2)$  MeV far exceeds  $Q_\beta(^{15}\text{C}) = 9.77$  MeV, making it impossible for  $^{15}\text{C}$  to feed the production of  $^{14}\text{C}$  nuclei from its ground state except via a dark decay. Therefore,  $^{15}\text{C}$  could serve as a suitable candidate to investigate the dark decay by observing the emergence of long-lived  $^{14}\text{C}$  isotopes in its decay. Regrettably, the relatively high  $S_n(^{15}\text{C}) = 1.218(1)$  MeV restricts about 55% of the open mass range, making this a "low-risk low-reward" isotope.

$^{17}\text{C}$  The dark decay with this nucleus would result in the production of the radioactive  $^{16}\text{C}$  like  $^{17}\text{C} \rightarrow ^{16}\text{C} + \chi$  with an estimated upper limit at  $\approx 10^{-6}$ . The  $S_n(^{17}\text{C}) = 0.734(18)$  MeV value makes this nucleus sensitive to all the open mass range. The  $A = 16$  carbon isotope would then mostly decay into the stable  $^{15}\text{N}$  nucleus through the  $\beta n$  channel, or into the unstable  $^{16}\text{N}$  via a simple  $\beta$  decay which can later feed the production of  $^{16}\text{O}$  or  $^{12}\text{C}$  stable isotopes. Although unobserved yet, the  $\beta 2n$  channel is energetically open from the ground state of  $^{17}\text{C}$  and feeds the production of  $^{15}\text{C}$  and 2 free neutrons since  $Q_\beta(^{17}\text{C}) = 13.2$  MeV is greater than  $S_{2n}(^{15}\text{N}) = 8.4$  MeV. The authors in [79] make the point that, due to this potential decay channel,  $^{17}\text{C}$  would not be a practical choice to investigate nuclear dark decays. This point is challenged in the next section.

### 2.3.2 Discussing the $^{17}\text{C}$ case

First decay	$t_{1/2}$ (s)	Second decay
	$(^{17}\text{C}) = 0.193(5)$	
$^{17}\text{C} \rightarrow ^{16}\text{C} + \chi$	$(^{16}\text{C}) = 0.750(5)$	$(\beta) \rightarrow ^{16}\text{N}$ (see next lines) $(\beta n) \rightarrow ^{15}\text{N}$ stable
$^{17}\text{C} \rightarrow ^{17}\text{N} + \beta + \bar{\nu}_e$	$(^{17}\text{N}) = 4.171(3)$	$(\beta) \rightarrow ^{17}\text{O}$ stable $(\beta n) \rightarrow ^{16}\text{O}$ stable $(\beta\alpha) \rightarrow ^{13}\text{C}$ stable
$^{17}\text{C} \rightarrow ^{16}\text{N} + \beta + \bar{\nu}_e + n$	$(^{16}\text{N}) = 7.13(1)$	$(\beta) \rightarrow ^{16}\text{O}$ stable $(\beta\alpha) \rightarrow ^{12}\text{C}$ stable
$^{17}\text{C} \rightarrow ^{15}\text{N} + \beta + \bar{\nu}_e + 2n$	$(^{15}\text{N}) \equiv \text{stable}$	none

TABLE 2.1 – All  $^{17}\text{C}$  decay channels including the unobserved  $\beta 2n$  and the potential dark decay.

The authors in [79] argued that the formation of  $^{15}\text{N}$  nuclei could result from dark decays or  $\beta 2n$  decays in  $^{17}\text{C}$ , thus depriving this nucleus of any distinctive decay products caused by a dark decay. Although  $^{17}\text{C}$  does not appear to be a favorable candidate to investigate the dark decay model, we will now discuss a potential way to do it based on the different half-lives of all nuclei involved in the  $^{17}\text{C}$  decay. The  $\beta$  and  $\beta n$  as well as the unobserved  $\beta 2n$  and the dark decay from the  $^{17}\text{C}$  ground state are listed in Table 2.1. From this table, we can see that all the particles present after a dark decay also appear in all the standard decay channels. Although there is no unique particle emission that can be linked to a dark decay, it would be possible to detect and isolate a signal correlated to a dark decay through the several neutron emission channels involved in the  $^{17}\text{C}$  decay scheme.

Neutron emission in such decays implies going through very short-lived states with typical lifetimes much shorter than the lifetime of any nuclei in Table 2.1. As a result, all neutron emissions discussed here can largely be considered as following the half-life of the parent nucleus only. Therefore, without any dark decays, neutron detection in a simple implantation and decay experiment should only follow the half-lives  $t_{1/2}({}^{17}\text{C}) = 0.193(5)$  s and  $t_{1/2}({}^{17}\text{N}) = 4.171(3)$  s. In the case of a dark decay, a third component following the half-life  $t_{1/2}({}^{16}\text{C}) = 0.750(5)$  s should also be detected. There is a factor  $\approx 4$  between each lifetime value, which in the case of neutron detection should leave no ambiguity about the decay channel involved. The feasibility and expected outcomes of such an experiment are discussed in more detail at the end of this manuscript as a perspective.

### 2.3.3 Dark decay in ${}^6\text{He}$

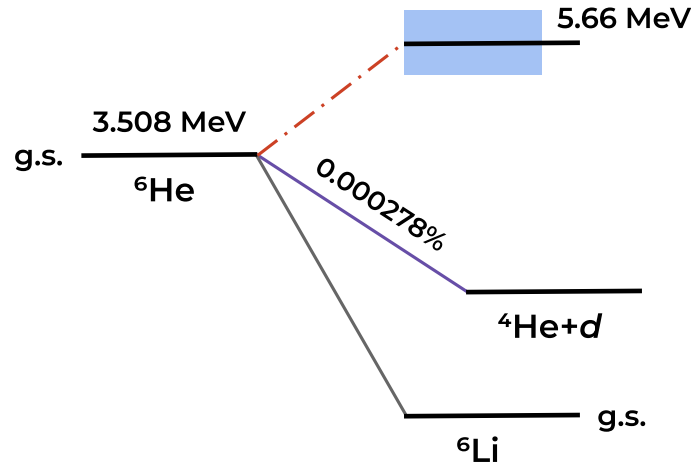


FIGURE 2.7 – Decay scheme of the  ${}^6\text{He}$  nucleus. The  $S_n({}^6\text{Li})$  value is located 5.66(5) MeV above the  ${}^6\text{Li}$  ground state, making it unreachable for a  ${}^6\text{He}$  nucleus at rest.

The  ${}^6\text{He}$  nucleus is a Borromean system composed of a  ${}^4\text{He}$  core and a halo of two neutrons. The  $S_n({}^6\text{He}) = 1.7$  MeV actually does not meet the energy requirement, but the  $S_{2n}({}^6\text{He}) = 0.975$  MeV does. A dark decay in this nucleus would therefore take the form of the following 3-body decay :



where a  ${}^4\text{He}$  nucleus in its ground state and a free neutron are emitted without going through the unbound  ${}^5\text{He}$  system as an intermediate step. In its ground state, the  ${}^6\text{He}$  nucleus decays predominantly to the  ${}^6\text{Li}$  ground state with a small  $\beta d$  channel that results in the emission of free  $\alpha$  and deuteron particles. The neutron emission threshold  $S_n({}^6\text{Li}) = 5.66(5)$  MeV is well above the  ${}^6\text{He}$  ground state, making it unreachable without additional energy. The  ${}^6\text{He}$  decay scheme is shown in Figure 2.7.

Neutron emission is not allowed in a standard  ${}^6\text{He}$  decay except via the channel proposed in Equation 2.18. In contrast to  ${}^{11}\text{Li}$  and  ${}^{11}\text{Be}$ , it is not necessary to rely on

complementary measurements required to distinguish the dark decay signal from a standard decay channel. In this framework, detecting free neutrons emitted from the decay of  ${}^6\text{He}$  nuclei would therefore be a unique and clear signature of dark matter creation. In addition,  $S_{2n}({}^6\text{He}) = 0.975$  MeV enables the investigation of approximately 75% of the available mass range for  $\chi$  to be a potential dark matter candidate. Finally, the emitted neutron is expected to have a kinetic energy  $E_n \lesssim 0.6$  MeV.

## 2.4 Summary

Many different scenarios presented in this chapter could provide a solution (complete or partial) to the neutron lifetime discrepancy. An idea that has gained a lot of attention in the past 6 years is the neutron dark decay model presented by Fornal and Grinstein in 2018 [76]. This model assumed that the bottle results discussed in the first chapter give the correct total neutron lifetime, whereas the beam results give the partial neutron lifetime from  $\beta$  decay. Hence, explaining the discrepancy with new channels required neutral or invisible particles in the final state.

Although the decay channels that involve SM particles in the final state have already been severely constrained [80, 81, 82], alternative approaches are needed to test the last open channel with invisible particles only in the final state. Right now, studying the impact of neutron dark decays in neutron stars does not provide sufficient information to confirm or disprove the model. The only possibility left to further investigate it is through nuclear dark decays. The discussion in [79] and reviewed in this chapter have shown that the  ${}^6\text{He}$  nucleus is an ideal candidate to test the dark decay, as it proposes a clean and unique signature while covering a large part of the open mass range for the dark fermion.

# Chapter 3

## E819S experiment at GANIL

The E819S experiment took place at the Grand Accélérateur National d'Ions Lourds (GANIL) and lasted one week in June 2021. In this chapter, we will give a description of this experiment, from beam production to the experimental setup. The calibration of each detector used during the campaign is also discussed.

### Contents

---

<b>3.1 Overview of the experiment</b> . . . . .	<b>37</b>
<b>3.2 Neutron detector TETRA</b> . . . . .	<b>39</b>
3.2.1 Description . . . . .	39
3.2.2 Possible sources of background . . . . .	40
3.2.3 Calibration . . . . .	41
<b>3.3 HPGe detector</b> . . . . .	<b>43</b>
3.3.1 Data analysis and calibrations . . . . .	44
3.3.2 Comparison with classic threshold . . . . .	46
<b>3.4 Other diagnostics</b> . . . . .	<b>49</b>
3.4.1 Plastic scintillator . . . . .	49
3.4.2 Transformateur d'intensité . . . . .	49
3.4.3 Silicon detector . . . . .	50

---

### 3.1 Overview of the experiment

#### Production of the ${}^6\text{He}^+$ and ${}^8\text{He}^+$ radioactive beams

The aim of this study is to investigate the possible existence of a neutron emission decay branch in the disintegration of the  ${}^6\text{He}$  nucleus, which can be related to dark matter creation through the model of Fornal and Grinstein [76]. The GANIL facility is capable of producing a low-energy, high-intensity radioactive  ${}^6\text{He}$  beam ( $\sim 10^8$  pps), which is required to probe this dark decay mode, since its branching ratio is expected to be very low ( $\text{Br}_\chi \leq 1.2 \times 10^{-5}$ ).

The production technique is first based on an Electron Cyclotron Resonance (ECR) ion source coupled to a compact cyclotron is used to produce a primary  ${}^{13}\text{C}$  beam at an energy lower than 1 MeV/A. This beam is then sent to the CSS1 and CSS2 separated sector cyclotrons to be accelerated at an energy of 95 MeV/A. Finally, the primary beam is delivered to the SPIRAL1 facility to produce the secondary radioactive beam using the Isotope Separation On-Line (ISOL) method [98]. The primary beam hits the Nanogan3 target-ion source composed of a thick and multilayered  ${}^{12}\text{C}$  target to produce  ${}^{6,8}\text{He}$  atoms through nuclear reactions. These radioactive atoms are then released from the target by effusion and stochastically enter the ECR ion source part, where they are ionized, extracted, and separated by a dipole magnet to form a pure beam of  ${}^6\text{He}^+$  or  ${}^8\text{He}^+$ . The secondary beam is not post-accelerated by the CIME cyclotron. Instead, it is transported directly to the experimental setup through the Ligne d'Ions Radioactifs A Très basse énergie (LIRAT) line dedicated to low-energy beams, as shown in Figure 3.1. The beam energy was  $\sim 25$  keV and  $\sim 19$  keV for  ${}^6\text{He}^+$  and  ${}^8\text{He}^+$  ions, respectively.

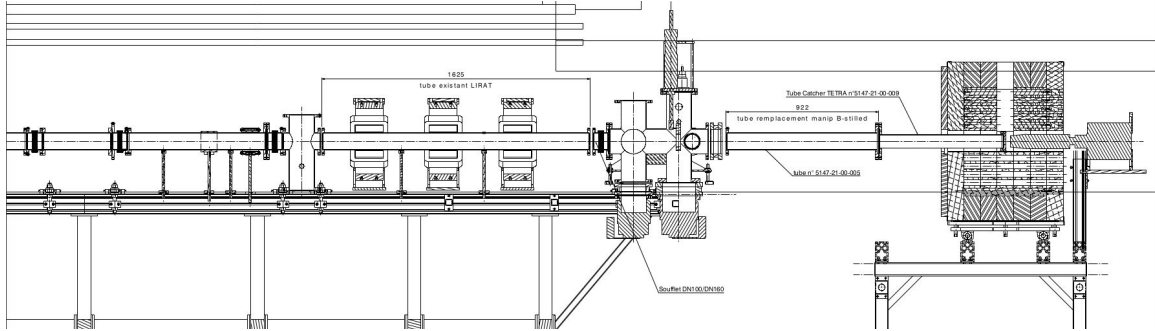


FIGURE 3.1 – Mock-up of the LIRAT line at the time of the experiment. The experimental setup with the neutron detector TETRA is located at the end of the line on the right.

#### The experimental setup and method

The LIRAT line is composed of many dipole and quadrupole magnets to transport the low-energy beam with an efficiency greater than 80%. Beam monitors placed along the line were used to measure the spatial distribution of the beam. A silicon detector was also used to provide an online assessment of the secondary beam intensity before sending it to the experimental setup. During the campaign, the end of the line consisted of a thin  $150 \mu\text{m}$  aluminum foil that served as a beamcatcher, as shown on the top right corner of

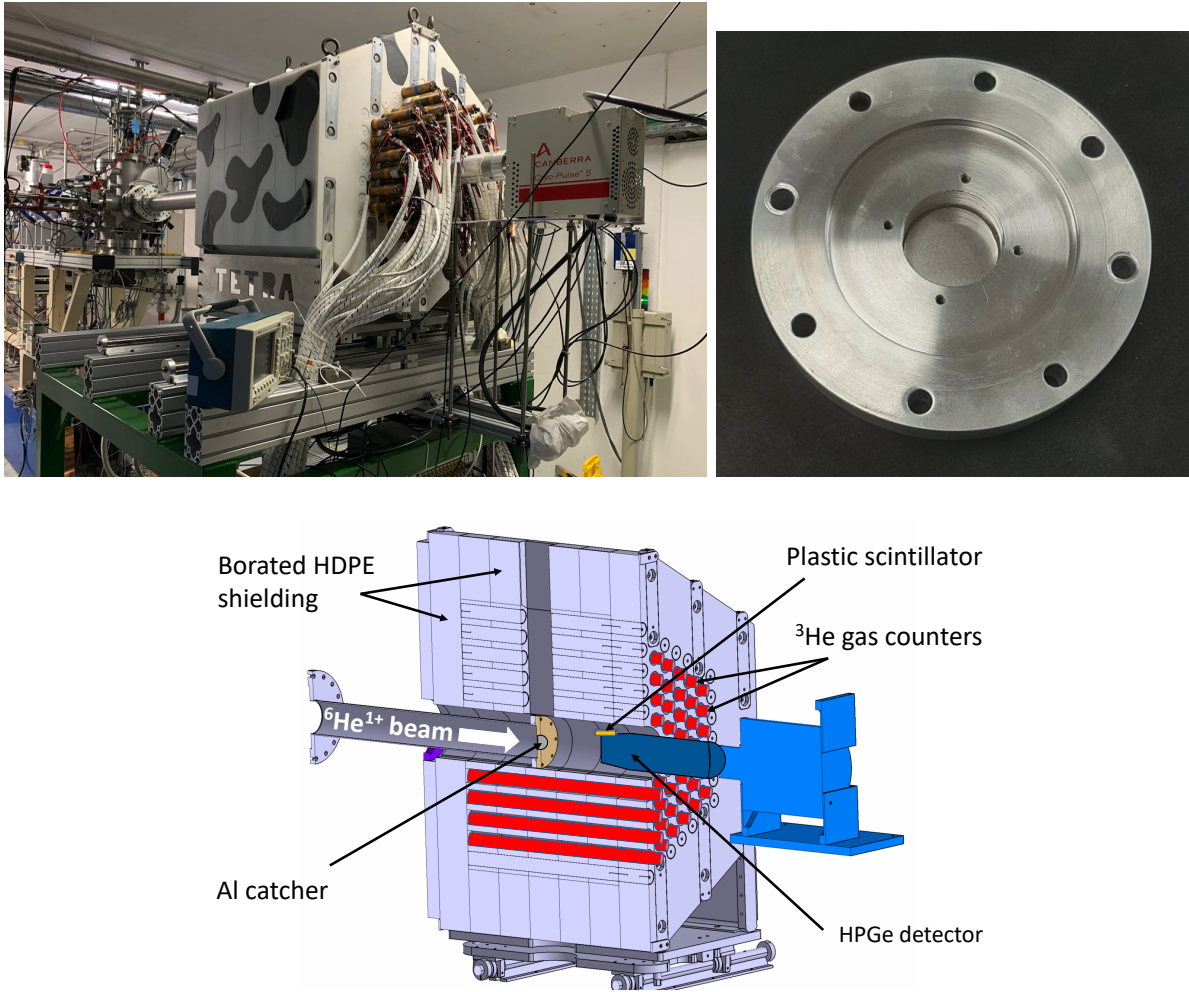


FIGURE 3.2 – Top left : Picture of the experimental setup. The neutron detector TETRA is in the middle, the LIRAT line is on the left, and the HPGe can be seen on the right part of the picture. Top right : Picture of the thin aluminum foil in which the radioactive ions were implanted and located at the center of TETRA. Bottom : Sectional view of the neutron detector TETRA. This view also includes the HPGe, the plastic scintillator and the aluminum catcher.

Figure 3.2. The low-energy ions were implanted and stopped inside this foil, where they did not undergo any nuclear reactions, apart from decaying.

The experimental setup was built around the beamcatcher to observe the decay products. A fast electric deflector located upstream of the last dipole magnet was used to cut the beam off and on. In a typical cycle, the ions were implanted for 3 seconds before being cut for 7 seconds. In the dark decay scenario, free neutrons should be emitted at a rate proportional to the implanted and surviving  ${}^6\text{He}$  population in the catcher. Otherwise, the detected neutron should only come from the ambient background at a constant rate. Therefore, the aim of this experiment was to measure neutron signals that follow the  ${}^6\text{He}$  lifetime within an implantation cycle. For this purpose, the main component of our experimental setup was the high-efficiency  $4\pi$  neutron detector called TETRA. In

addition, we also used a high purity germanium (HPGe) semiconductor to detect  $\gamma$  rays, and a small solid angle plastic scintillator to monitor  $\beta$  particles, as shown at the top of Figure 3.2. The signals collected by these detectors were sent to a FASTER digital data acquisition (DAQ) system [99]. Furthermore, the intensity of the primary  $^{13}\text{C}$  beam on the  $^{12}\text{C}$  target and a pulse corresponding to the beginning of each implantation cycle were recorded in the same FASTER DAQ. The data from the silicon detector placed in the LIRAT line was registered with a different DAQ.

## 3.2 Neutron detector TETRA

### 3.2.1 Description

TETRA is an array of gas-filled counters arranged in 5 hexagonal layers that is dedicated to the detection of slow neutrons. Counters are 500mm long steel cylinders with a 32mm diameter. There is a thin tungsten wire in the middle that plays the role of the anode, which is directly connected to its own preamplifier. The counters are filled with an admixture of  $^3\text{He}$  ( $\sim 99\%$ ) and  $\text{CO}_2$  ( $\sim 1\%$ ) at a nominal pressure of 7 atm. Therefore, neutron detection with TETRA is solely based on the following neutron capture reaction with  $^3\text{He}$  :



The cross section of this neutron capture reaction varies as  $\propto E^{-1/2}$ , where  $E$  is the kinetic energy of the incident neutron [100]. This means that the lower the neutron energy, the higher the cross section. One advantage of this is that there is no threshold for neutron detection with  $^3\text{He}$ , but neutrons have to be slowed to thermal levels ( $\sim 0.025$  eV) to have a better chance of being captured. For that reason, all  $^3\text{He}$  counters are embedded within a single-piece polyethylene structure that serves as a neutron moderator. Moreover, this structure is placed inside a 15 cm thick layer of borated polyethylene (high-density polyethylene + boron) used to shield the detector in order to highly suppress the detection of background neutrons.

The reaction shown in Equation 3.1 is destructive, which means that there is no possible cross-talk between the counters when it comes to neutron detection. It is also an exothermic reaction. The H isotopes produced will be released into the gas with kinetic energies of  $E(^3\text{H}) = 0.191$  MeV and  $E(^1\text{H}) = 0.573$  MeV that are large enough to ionize it. A high voltage of +1720V was applied to each counter, which corresponds to the proportional counting regime. Then, the ionization products are collected by the tungsten wire and give rise to a signal sent to the preamplifier. TETRA has its own internal electronic system after the preamplifier with multiple layers to treat and record an event. The signals after amplification usually have an amplitude  $0.01 \leq A \leq 5$  Volts with a rise and a down time of  $\sim 2\mu\text{s}$  and  $\sim 5\mu\text{s}$ , respectively.

The signals from each counter were recovered directly after the amplification stage and sent to the FASTER DAQ through a CRRC4 spectroscopy module connected to a Mosahr board. The CRRC4 module is an analogic-to-digital converter (ADC) designed to process signals every 8 ns (125 MHz). When a signal exceeds the detection threshold,

an ADC window of  $20\mu\text{s}$  is opened, which corresponds to the average time it takes for the baseline to be fully restored. During this time, both the timestamp and the maximum amplitude are encoded. The thresholds for each counter were set as low as possible ( $\sim 100$  mV) so that they could be better adjusted offline during the data analysis.

### 3.2.2 Possible sources of background

The following is a simple list of the possible sources of background that can be detected with TETRA. The evaluation of the background rate with respect to the deposited energy in TETRA is discussed in Section 3.2.3.

**Neutron from the production cave** In addition to neutron events coming from a radioactive source or beam, a neutron flux can also be detected coming from the production cave at a constant rate where the target-ion source is located and somewhat close to the experimental setup. Two types of background runs were performed accordingly, with and without the primary  $^{13}\text{C}$  beam hitting the target to evaluate the difference.

**Cosmic radiations** Although TETRA is a shielded detector and was located underground during the experiment, cosmic-rays could still be detected from time to time. Furthermore, even though they are randomly distributed in time, these radiations are scarce and can produce a large number of events in a short period of time, locally increasing the detection rate. Therefore, they can potentially add too much weight during the implantation time and mimic the dark decay in  $^6\text{He}$ .

**Microdischarges** A common source of background in gaseous detector in proportional counting regime. Similarly, to cosmic radiations, the rate of these events can be very disparate and alter the energy spectrum in the neutron detection range. It is possible to discriminate these spurious events directly from their pulse shape and risetime after the preamplifier [101]. This technique could not be used during the experiment as we did not digitise the pre-amplified signal.

**Photon detection** Each counter can also be triggered by photons that can ionize the gas. These photons can be  $\gamma$ -rays that come from a nuclear transition. They can also source their origin from a  $\beta$ -decay, which, in turn, leads to the emission of bremsstrahlung photons from the interaction of the emitted  $\beta$ -particle with the surrounding matter. Due to a very high  $^6\text{He}$  beam intensity ( $\approx 10^8$  pps, see Section 5.2.2), we detected a lot of bremsstrahlung radiations with TETRA. Although the gas admixture in the counters was specifically chosen in order to allow for a very good discrimination in the signal amplitude between photon and neutron events [102], there is still a small probability that such radiations can lead to events within the expected neutron detection range and mimic the dark decay we are trying to observe <sup>1</sup>. Similarly to microdischarges, these events could have been partially discriminated thanks to the same pulse shape analysis method [101].

<sup>1</sup>MCNP simulations of TETRA to test the gamma ray sensitivity. X. Ledoux (GANIL) private communication

### 3.2.3 Calibration

TETRA arrived at GANIL with 82  $^3\text{He}$  counters, two of which were not usable. The remaining 80 counters were tested and calibrated in both efficiency and deposited energy using a  $^{252}\text{Cf}$  neutron source. Eight other counters were not taken into account due to an inappropriate response function or additional noise found during the  $^6\text{He}$  beam analysis. In the end, unless otherwise stated, a total of 72 counters were used in the following work.

#### Properties of the $^{252}\text{Cf}$ source

The source used to calibrate TETRA had an initial activity given by the GANIL Radiation Protection Service (SPR) at 21633 Bq 16 days before the experiment with a relative uncertainty of 10%. The source contains 92.295% of  $^{252}\text{Cf}$  isotopes, which is the main neutron emitter for sources no older than 20 years [103]. The  $A = 252$  isotope has a half-life of 2.645(8) years. It has a spontaneous fission rate of 3.086(8)% with a mean number of neutrons emitted per fission of 3.7675(40). The 16 days between the SPR source activity assessment and the calibration runs were taken into account, reducing the activity to 21386 Bq. Therefore, at the time of the experiment, the source had an emission rate of  $r_n = 2295.9 \pm 248.8$  neutrons per second.

#### Deposited energy calibration

TETRA was working in the proportional counting regime, which means that the amplitude of each signal is directly proportional to the energy deposited by the particle ionizing the gas. For that reason, all TETRA counters were calibrated in deposited energy with a simple linear model as :

$$E_{dep} = aC, \tag{3.2}$$

where  $E_{dep}$  is the deposited energy in keV,  $C$  is the channel number attributed to the signal amplitude and  $a$  is the conversion coefficient to be determined. Using the  $^{252}\text{Cf}$  neutron source, we can assess for each counter its coefficient  $a$  using the 765 keV full energy peak from the neutron capture reaction. The same approach was used directly with the  $^8\text{He}$  data with runs performed before and after the experiment with the  $^6\text{He}$  beam. The calibration coefficients returned were consistent with the one assessed by the  $^{252}\text{Cf}$  run performed at the beginning of the experimental campaign, except for some runs at the very end of the experiment after an electronic shift and a reboot of TETRA electronics. These last runs gave coefficients in agreement with two  $^{252}\text{Cf}$  runs performed at the very end of the experiment and were used accordingly to ensure comparability during the analysis.

#### Efficiency calibration

Background runs were performed to assess the background rate recorded by TETRA. For all events with deposited energy less than 1 MeV, the rate was 40 Hz (mainly due to pedestal effects), with only 1 Hz contributing to the background in the neutron detection deposited energy range (between  $\sim 150$  and  $\sim 820$  keV). We observed a small increase in

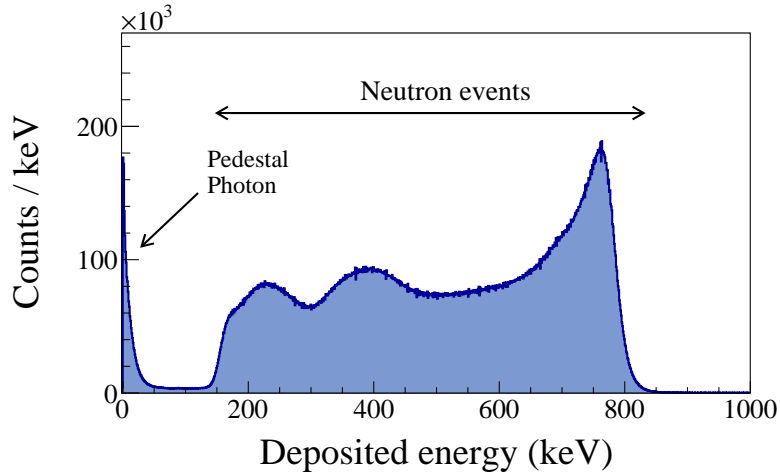


FIGURE 3.3 – Calibrated energy spectrum obtained with the  $^{252}\text{Cf}$  neutron source. Events with  $E_{dep} \lesssim 150$  keV are either from a pedestal effect or photon detection. Events in the range  $150 \lesssim E_{dep} \lesssim 850$  keV come from ionization induced by the proton and triton from the neutron capture reaction with the  $^3\text{He}$  gas.

the latter value to  $\approx 1.1$  Hz when the primary  $^{13}\text{C}$  beam hit the target in the production cave. Comparing the total number of events recorded with an energy deposition between 150 and 820 keV (corresponding to the ionization initiated by the neutron capture reaction), to the source neutron rate  $r_n$  and the duration of the run, we obtain the following neutron detection efficiency of TETRA  $\varepsilon_n = (46.89 \pm 5.09)\%$  with 72 counters.

The detection efficiency of TETRA has been shown to depend on the initial neutron energy through MCNP simulations [105]. The detection efficiency is constant for an initial energy below 1 MeV and then slowly decreases by a factor  $\sim 2$  for energies between 1 and

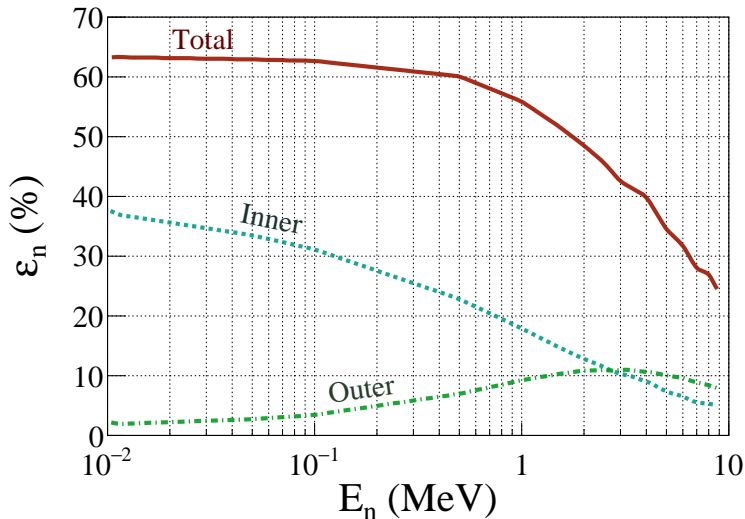


FIGURE 3.4 – Detection efficiency of TETRA with respect to the initial neutron energy  $E_n$ . The red line shows the efficiency curve of all TETRA whereas the blue and green dotted lines show the efficiency of the inner and outer ring of counters, respectively. This picture is a reproduction of Figure 6 in [104].

10 MeV, as can be seen in Figure 3.4. In the case of a neutron dark decay in  ${}^6\text{He}$ , the neutron emitted in the final state is expected to have a kinetic energy under 0.6 MeV which is in this constant detection efficiency range. The neutrons emitted from the radioactive  ${}^{252}\text{Cf}$  have a continuous kinetic energy distribution with a mean energy around 2 – 3 MeV [100, 106]. Therefore, the detection efficiency presented above is underestimated but will serve as a conservative value for the  ${}^6\text{He}$  analysis.

### 3.3 HPGe detector

A high purity germanium semiconductor was used during the experiment to detect any  $\gamma$  rays emitted during the  ${}^{6,8}\text{He}$  runs. The germanium crystal can be modeled simply by a cylinder with a radius of 36.5 mm and a length of 56 mm. It is encapsulated in an aluminum cap with a thin carbon window on the front. The crystal was cooled to 10 – 100 kelvin using a Canberra cryocooler apparatus with liquid nitrogen. The signal is sent to a FASTER trapezoidal spectroscopy module connected to a Mosahr board and operating in the Constant Fraction Discriminator (CFD) mode. In a simple threshold mode, pulses that cross the threshold level and remain above this level during a predefined time are treated. In the CFD mode, the signals from the Trigger module are modified according to the following model :

$$S_{\text{CFD}}(t) = s(t - \theta) - f \cdot s(t), \quad (3.3)$$

where  $s(t)$  is the amplitude of the incoming signal at time  $t$  and  $S_{\text{CFD}}(t)$  is its modified value after the CFD. The constant fraction parameter is denoted as  $f$  and was set at  $f = 1/2$  during the experiment, and  $\theta$  is the delay parameter set to 8 ns. This trigger mode is supposed to give a better assessment of the signal timestamp which corresponds to the 0 amplitude crossing, as this treatment somewhat ensures that the amplitude just before the signal is negative. The use of this mode, compared to a simple threshold, led to some problems during the experiment, which will be discussed later in this chapter. The germanium was calibrated in energy and efficiency using a  ${}^{152}\text{Eu}$  source. A total of 9 different  $\gamma$  lines were used for the calibration. These lines with their respective energies and intensities are summarized in Table 3.1. The uncertainties on the energy are typically very low ( $< 10^{-5}$ ) and are not shown in the table. On the other hand, the uncertainties on their associated intensities are given.

$E_\gamma$ (keV)	121.78	244.70	344.28	411.12	778.91	867.38	964.08	1112.08	1408.01
$I_\gamma$ (%)	28.41	7.55	26.59	2.238	12.97	4.243	14.50	13.41	20.85
$\Delta I_\gamma$	0.13	0.04	0.12	0.010	0.06	0.023	0.06	0.06	0.08

TABLE 3.1 – Energies and intensities of the  $\gamma$  lines used for the HPGe calibration. Intensities correspond to the number of  $\gamma$  rays emitted every 100 decays. All values can be found in [107].

### 3.3.1 Data analysis and calibrations

#### Energy and efficiency calibrations

Data were collected for 13483 seconds and 75264 seconds at the 20 and 40 cm positions respectively. The detector was calibrated in energy using the following linear model :

$$E = aC + b, \quad (3.4)$$

where  $a$  is the slope of the curve in keV/channel,  $b$  is an offset value in keV,  $C$  is the channel number corresponding to signal amplitude and  $E$  is its corresponding energy in keV. The peaks are fitted using a Gaussian model laid on top of a background described with either a  $0^{th}$  or  $1^{st}$  order polynomial in the region of the peak. The Gaussian distribution is written in the form :

$$G(x) = G_0 e^{-\frac{(x-\mu)^2}{2\sigma^2}}, \quad (3.5)$$

where  $G_0$  is the amplitude of the peak,  $\mu$  its mean value along the  $x$ -axis and  $\sigma$  is the standard deviation. The energy of each  $\gamma$  line is then plotted with respect to their measured  $\mu$  parameter returned by the fit. Finally, the data are fitted using a first-order polynomial. The values for  $a$  and  $b$  returned by the fit at both positions are given in the next table. The calibration coefficient values returned for both fits are very consistent together with only a very small difference in the offset.

Position (cm)	$a$ (keV/channel)	$b$ (keV)
21.7	0.0234(1)	0.8303(42)
43.7	0.0234(1)	0.9189(43)

TABLE 3.2 – HPGe energy calibration parameters with respect to its position.

To obtain the detection efficiency curve at both positions, all  $\gamma$  lines were treated as follows to retrieve the measured statistics. Each bin of the peak in the region  $\mu \pm 3\sigma$  is modified by removing the background from the total statistic. The background value for each bin is given thanks to the fit procedure described above. The bin error is also modified to take into account the error related to the background evaluation. We obtain the contribution of each  $\gamma$  line by adding all modified bin contents in the same  $\mu \pm 3\sigma$  region. Finally, the detection efficiency value is computed by comparing the measured statistics with the estimated number of  $\gamma$  emitted during the acquisition with the following equation :

$$N_{\gamma, det} = A t I_{\gamma} \varepsilon_{tot}, \quad (3.6)$$

where  $N_{\gamma, det}$  is the number of  $\gamma$  measured,  $A$  is the  $^{152}\text{Eu}$  source activity,  $I_{\gamma}$  is the corresponding  $\gamma$  intensity and  $\varepsilon_{tot}$  its corresponding detection efficiency value. The detection efficiency curves assessed at both positions are shown in Figure 3.5.

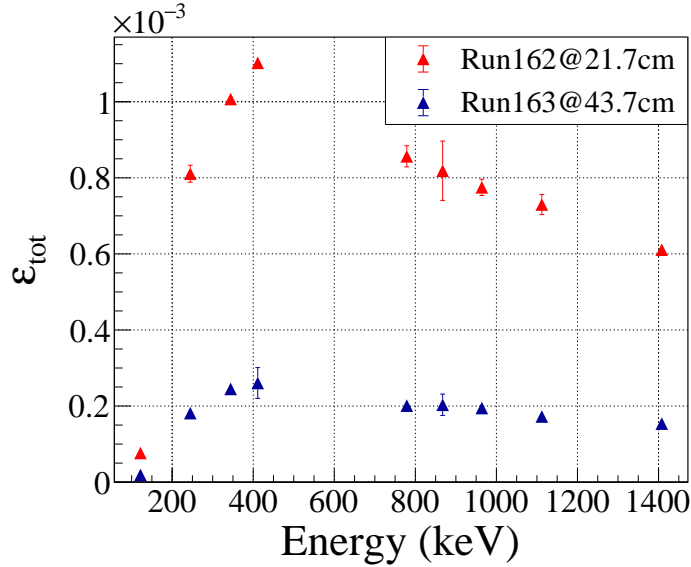


FIGURE 3.5 – Total detection efficiency with respect to the gamma energy at both positions.

### Intrinsic detection efficiency

The flange at the end of the line was replaced before carrying out the radioactive source runs, changing the distance to the HPGe by 2 millimeters. To account for this different geometry, we computed the intrinsic detection efficiency values as defined in Knoll [100] :

$$\varepsilon_{tot} = \varepsilon_{int}\varepsilon_{\Omega}, \quad (3.7)$$

where  $\varepsilon_{int}$  is the intrinsic detection efficiency and  $\varepsilon_{\Omega}$  corresponds to the geometrical efficiency defined as the fraction of solid angle encompassed by the detector  $\varepsilon_{\Omega} = \frac{\Omega}{4\pi}$ , where  $\Omega$  is the solid angle covered by the germanium crystal. In our case, the solid angle covered by a cylindrical detector is given by :

$$\Omega = 2\pi(1 - \cos \alpha) = 2\pi\left(1 - \frac{d}{\sqrt{d^2 + r^2}}\right), \quad (3.8)$$

where  $2\alpha$  is the apex angle,  $d$  is the distance between the source and the center of the germanium crystal and  $r$  is the radius of the germanium crystal. Using these equations, we obtain two sets of intrinsic detection efficiency values shown on the left in Figure 3.6, which can be compared to verify the model. All intrinsic detection efficiency values at the same energy match nicely considering the error bars. To obtain the final detection efficiency values at 21.9 and 43.9 cm, we first average the two sets of intrinsic efficiency values and their uncertainties. Then, since we need the efficiency at 477.6 and 980.8 keV (which are the only gamma rays emitted in the decay of  ${}^8\text{He}$ ), we fit the data between the two  $\gamma$ -rays at 411.12 and 1408.01 keV with a second order polynomial. Finally, using the fit parameters, we calculate the intrinsic efficiency at 477.6 and 980.8 keV and the geometrical efficiency at 21.9 and 43.9 cm using Equation 3.8. The final values for both energies and distances are summarized in the following table. The mean relative uncertainty calculated

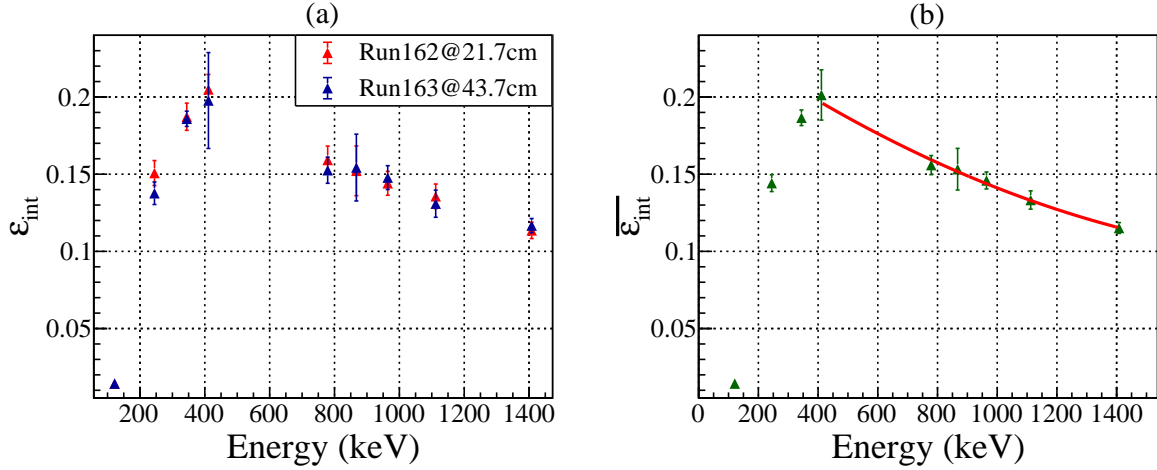


FIGURE 3.6 – (a) Intrinsic detection efficiency with respect to the gamma energy at both positions. (b) Average intrinsic efficiency with a second order polynomial fit between 400 keV and 1400 keV.

at 4.7% is attributed to all the final values.

Position (cm)	21.9	43.9
477.6 keV	$(9.63 \pm 0.46) \times 10^{-4}$	$(2.42 \pm 0.12) \times 10^{-4}$
980.8 keV	$(7.26 \pm 0.34) \times 10^{-4}$	$(1.83 \pm 0.09) \times 10^{-4}$

TABLE 3.3 – Final detection efficiency values for both gamma present in the  $^8\text{He}$  decay at both positions of the HPGe.

### 3.3.2 Comparison with classic threshold

#### Energy spectrum, efficiency and resolution

The detection efficiency curve that we obtain from the  $^{152}\text{Eu}$  source runs does not correspond to what was expected with this detector. The detection efficiency completely decreases for energies below 400 keV instead of going up. To investigate this effect, new runs were performed with the same HPGe plugged into a FASTER DAQ with two different signal acquisition thresholds running at the same time. The first is the same as the one presented earlier in this paper, and the second is a classic threshold. The runs were carried out with a  $^{152}\text{Eu}$  source or with a sample of thorium placed in front of the HPGe at a distance of around 20 centimeters. The detection rates in these runs were around 200 Hz for the classic threshold and around 60 Hz for the CFD. First, we can compare the calibrated energy spectrum obtained for the different signal treatment methods with the  $^{152}\text{Eu}$  radioactive source, as shown in Figure 3.7. The base count level is a little bit smaller for energies higher than 400 keV in the CFD mode but the number of counts radically drops for energies below 400 keV. The detection efficiency for each mode evaluated with the  $^{152}\text{Eu}$  source is shown on the left-hand side of Figure 3.8. The efficiency ratio

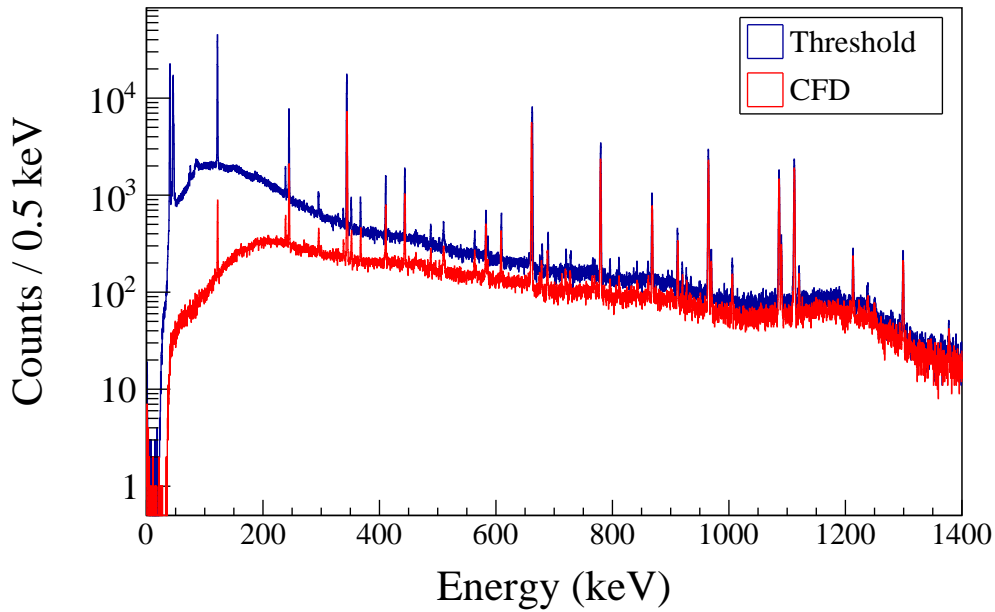


FIGURE 3.7 – Energy spectrum between 0 and 1400 keV obtained with a  $^{152}\text{Eu}$  source with a classic threshold (blue line) and with the CFD (red line).

between the two modes is shown on the right-hand side of the same figure with both the  $^{152}\text{Eu}$  source and the Thorite sample. These figures show that the way the CFD was set up strongly cut the detection efficiency of our acquisition system, especially in the 0-400 keV range.

The resolution of the HPGe measured with both radioactive samples in both acquisition modes is shown in Figure 3.9. The resolution values are not affected overall, except for energies lower than 400 keV, where the detection rate drops, but the smaller number of events could be the reason for the observed difference.

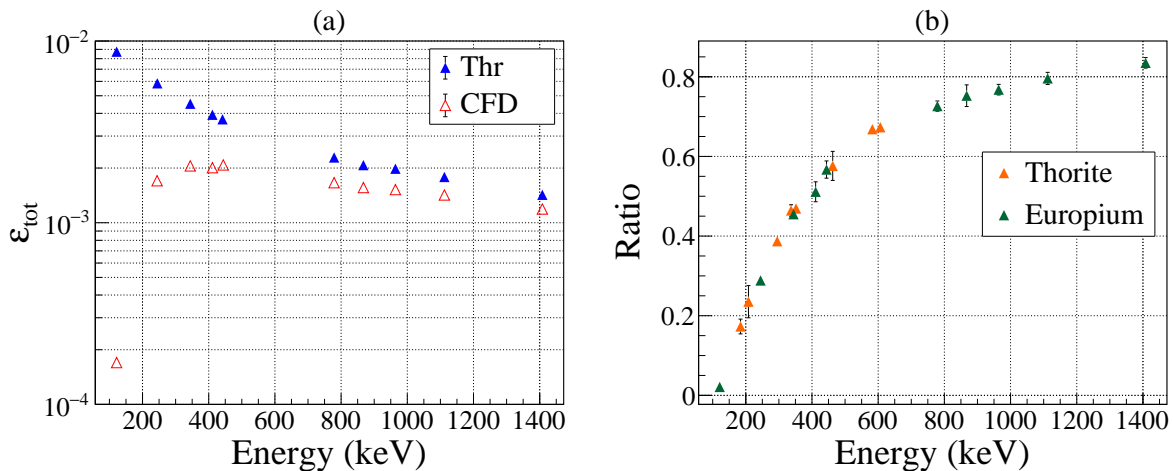


FIGURE 3.8 – (a) Total detection efficiency plot measured with the  $^{152}\text{Eu}$  source with both data treatment methods. (b) The ratio of detection efficiency assessed with the CFD mode over the classic threshold with both the Europium and Thorite sources.

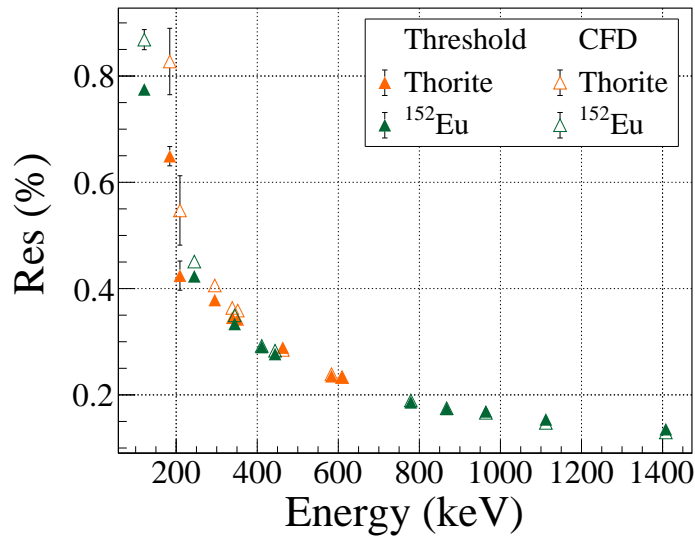


FIGURE 3.9 – Resolution of the HPGe with respect to the energy assessed with the Europium and the Thorium samples in both acquisition modes and a detection rate at  $\approx 200$  Hz.

### Distortion effect

In addition to the difference in observed statistics and in detection efficiencies, we also observed a peak distortion effect in the CFD mode compared to the classic threshold. We used a  $^{137}\text{Cs}$  source emitting a single 661.6 keV gamma-ray to investigate this phenomenon. The HPGe position was adjusted so that the detection rate remained the same between the two modes to ensure comparability. In Figure 3.10, we show the gamma line obtained with a 200 Hz detection rate in both acquisition modes. As can be seen, the line acquired

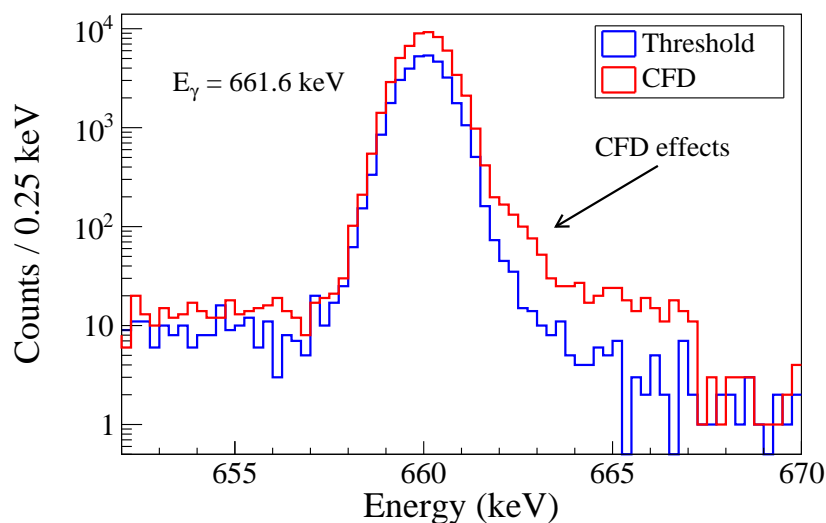


FIGURE 3.10 – Detection of the 661.6 keV gamma-ray obtained with a  $^{137}\text{Cs}$  source with a class threshold (blue line) and with the CFD (red line). The detection rate in both acquisitions was around 200 Hz. The CFD acquisition shows a small distortion effect.

with the CFD shows a small distorted area. This effect alters less than 0.1% of the events here. We also observed that this effect increase with the detection rate, though it still concerns only a fraction of the recorded events. Although the CFD mode was shown to alter the detection of gamma with the HPGe in a mostly negative way, it had little to no significant repercussion in the following  $^{6,8}\text{He}$  analysis.

## 3.4 Other diagnostics

### 3.4.1 Plastic scintillator

On top of the HPGe was placed a small solid angle plastic scintillator coupled with a Hamamatsu photomultiplier tube as shown in Figure 3.11 and dedicated to the detection of  $\beta$  particles. It is a rectangular scintillator with dimensions  $0.5 \times 0.5 \times 1.5$  cm that was covered with aluminized tape. The signal was sent to the FASTER DAQ through a QDC-TDC module connected to a Caras board. The QDC module is an ADC specifically designed for charge integration and is able to process signals every 2ns (500MHz). Calibration runs were performed with radioactive sources of  $^{36}\text{Cl}$  and  $^{90}\text{Sr}$ . Unfortunately, these runs were performed at the end of the experiment with different settings for signal treatment within FASTER from radioactive ion beam runs. The trigger threshold width in the last  $^8\text{He}$  runs was moved from an initial 2 ns value used throughout the experiment to 4 ns. This different setting considerably changed the background level. Moreover, the background level has been shown to depend on the position of the plastic scintillator with a much higher rate at the farthest position. Therefore, the data analysis of the calibration and background runs performed mainly at the end of the experiment was not conclusive. As we relied on the scintillator to evaluate the intensity of the  $^6\text{He}$  beam, its detection efficiency was therefore evaluated using the  $^8\text{He}$  data and will be discussed later in the manuscript.



FIGURE 3.11 – The small solid angle plastic scintillator used during the experiment. It was placed on top of the HPGe aluminum cap and held in place using tape.

### 3.4.2 Transformateur d'intensité

The "*Transformateur d'intensité*" (Ti), is a charge collecting device that was used to measure the primary  $^{13}\text{C}$  beam intensity onto the  $^{12}\text{C}$  target in  $\mu\text{A}$ . The beam intensity was first measured directly in  $\mu\text{A}$  every 14 minutes with a different DAQ with a precision of 50 nA. The signal from the Ti was also sent into our own FASTER acquisition in which the intensity was encoded thanks to a rate meter. The calibration curve shown in

Figure 3.12 is obtained by matching the periodic measurement in  $\mu\text{A}$  from the external acquisition to the engagement rate in Hz from the FASTER DAQ.

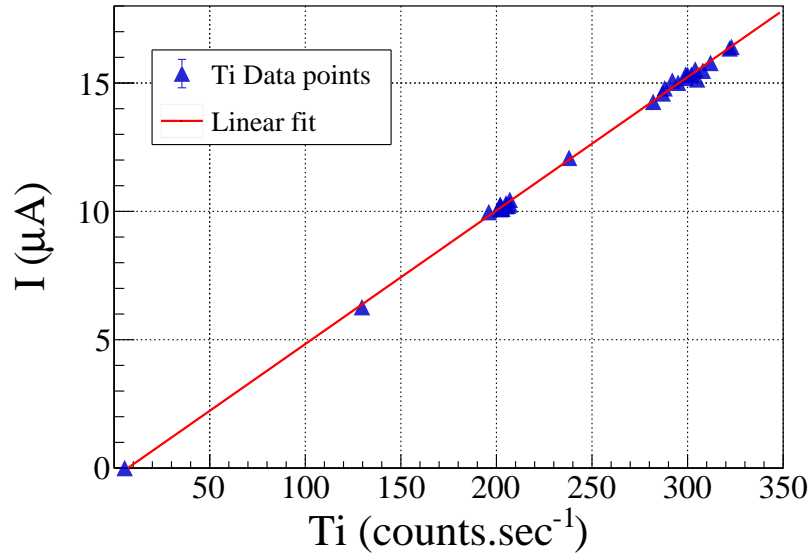


FIGURE 3.12 – Calibration curve obtained for the Ti. The first data point comes from a background in which the cyclotrons were not running.

### 3.4.3 Silicon detector

A silicon detector was placed directly inside the LIRAT line, a few meters ahead of the experimental setup with TETRA. It was used as an online tool to give a rough assessment of the intensity of the  ${}^6,8\text{He}$  beam. The focal point of the beam could easily be changed by using the different optical elements along the line to switch between the catcher at the end of the line and another thin aluminum foil placed right in front of the silicon detector.

We will see later that the average beam intensity values were around  $10^5$  and  $10^8$  particles per second for the  ${}^8\text{He}$  and  ${}^6\text{He}$  beams, respectively. Mechanical and electrostatic reducers with known reduction factors were used to scale down the beam intensity to ensure good measurement with the silicon detector and ensure that it would not break down. Assuming a rough detection efficiency of  $\sim 50\%$ , the beam intensity could therefore be assessed simply from the detection rate scaled by these reduction factors.

The data collected with the silicon detector were registered by a VXI DAQ external to the main FASTER acquisition, as it was not part of the experimental setup dedicated to the dark decay investigation. A pulser was also used to send a signal in the VXI DAQ to evaluate the number of missed events due to deadtime effects. The runs performed with the silicon detector were short and were a simple tool to quickly tune and adjust the beamline elements to improve the transport of the beam and its intensity online. The data measured with the silicon detector were used mainly to further check the consistency of the experimental setup through  ${}^8\text{He}$  beam runs.

# Chapter 4

## $^8\text{He}$ analysis

The first data analysis was performed with the  $^8\text{He}$  data to benchmark the experimental setup by comparing the implantation rate assessed with TETRA, the HPGe and the silicon detector in the LIRAT line. It also allowed us to compare the radioactive beam intensity with the primary beam intensity on target. The detection efficiency value for the plastic scintillator was also estimated with the  $^8\text{He}$  data. Finally, we present a new measurement for the  $^8\text{He}$  half-life with an improvement in precision compared to the existing values in the literature.

### Contents

---

<b>4.1</b>	<b><math>^8\text{He}</math> decay scheme</b>	<b>52</b>
<b>4.2</b>	<b>Average <math>^8\text{He}</math> beam intensity</b>	<b>53</b>
4.2.1	Analysis method	53
4.2.2	Results of the calculations	57
4.2.3	$^8\text{He}$ beam intensity versus primary beam intensity	57
<b>4.3</b>	<b>Detection efficiency of the plastic scintillator</b>	<b>59</b>
4.3.1	Data analysis of the plastic scintillator	59
4.3.2	G4beamline simulations	61
<b>4.4</b>	<b><math>^8\text{He}</math> half-life measurement</b>	<b>66</b>
4.4.1	First analysis	66
4.4.2	Deadtime corrections	69
4.4.3	Summary and best $^8\text{He}$ half-life estimate	73

---

## 4.1 ${}^8\text{He}$ decay scheme

The  ${}^8\text{He}$  nucleus is generally described as a  ${}^4\text{He}$  core surrounded by four valence neutrons forming a neutron skin. The half-life of  ${}^8\text{He}$  is  $119.1 \pm 1.2$  ms and its decay scheme from its ground state is shown in Figure 4.1. The main decay branch is a  $\beta$  decay with a branching ratio of 84(1)% [108] leading to the first excited state of  ${}^8\text{Li}$  at 980.8 keV followed by the emission of a  $\gamma$ -ray and by the  $\beta$  decay of the  ${}^8\text{Li}$  daughter nucleus. The second decay branch is a  $\beta$  delayed neutron emission branch with a branching ratio of 16(1)% [108]. This decay actually feeds different energy levels of  ${}^8\text{Li}$  above its neutron emission threshold ( $S_n = 2.032$  MeV). The levels that lead to neutron emission are the 3.21 and 5.4 MeV levels [108], but to date no measurement has given their respective contribution. This neutron emission produces  ${}^7\text{Li}$  either in its ground state or in its first excited state at 477.6 keV. It was measured that  $(32 \pm 3)\%$  of the  $\beta$  delayed neutron emission populates the first excited state of  ${}^7\text{Li}$  [108]. Finally, a small  $\beta$  delayed triton emission was also observed with a branching ratio of  $(0.9 \pm 0.1)\%$  in a different experiment [109]. The only branching ratio that was actually measured in [108] is the total 16% of the two  $\beta n$  branches. The emission probability of 84% for the simple  $\beta$  branch was therefore deduced from the first simply by calculating  $(1-0.16)$ . As the  $\beta t$  branch was measured later in a separate experiment, we reduced the probability of 84% to 83.1% to preserve unity in the following analysis. Therefore, each  ${}^8\text{He}$  decay is followed by a  ${}^8\text{Li}$  decay 83.1% of the time giving an average number of 1.831 electron emitted for each  ${}^8\text{He}$  decay.

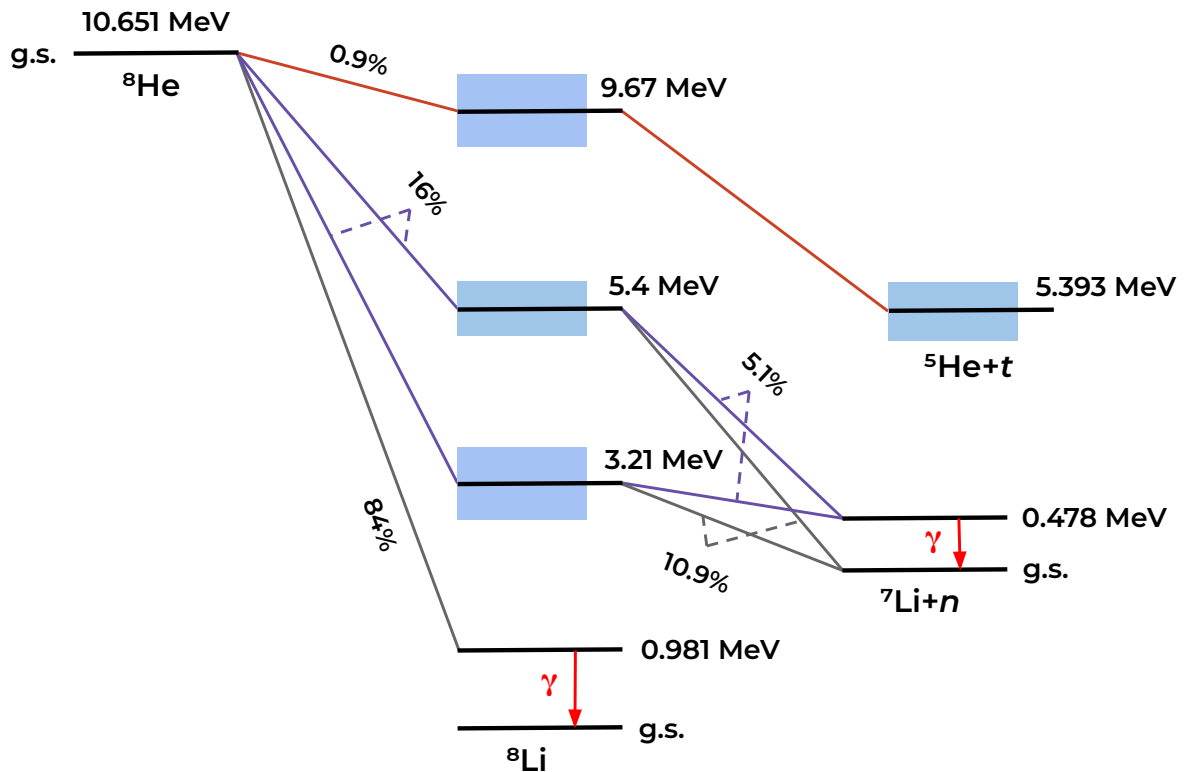


FIGURE 4.1 – Decay scheme of the  ${}^8\text{He}$  nucleus from its ground state.

## 4.2 Average $^8\text{He}$ beam intensity

To first check the consistency of the experimental setup, we computed the average  $^8\text{He}$  beam intensity implanted in the aluminum catcher with all detectors at our disposal. The two possible  $\gamma$ -rays emitted from the decay of  $^8\text{He}$  in its ground state were observed with the HPGe detector. Neutron events from the  $\beta n$  branch were measured with TETRA. Finally, the number of electrons emitted in the decay of both  $^8\text{He}$  and  $^8\text{Li}$  was monitored with the silicon detector along the LIRAT line and the plastic scintillator on top of the HPGe.

In the following sections, we explain how the number of events  $N_{\text{det}}$  related to  $^8\text{He}$  or  $^8\text{Li}$  decay is obtained for each detector and for each run. Once  $N_{\text{det}}$  is established, the average  $^8\text{He}$  beam intensity  $r_0$  during the run is calculated as :

$$r_0 = \frac{N_{\text{det}}}{\varepsilon \text{Br} t_{\text{run}}}, \quad (4.1)$$

where  $\varepsilon$  is the detection efficiency of the detector, Br is the branching ratio of the observed decay branch and  $t_{\text{run}}$  is the duration of the run. When the radioactive beam was implanted in cycles within the aluminum catcher, we used  $t_{\text{run}} = N_{\text{cycles}} \times t_{\text{ON}}$  where  $N_{\text{cycles}}$  is the number of implantation cycles in the run and  $t_{\text{ON}}$  is the duration of the implantation. For the detection of electrons with the plastic scintillator, the branching ratio value used during the analysis is 1.831, which takes into account the  $\beta$  decay of  $^8\text{Li}$ . The total uncertainty on  $r_0$  values presented hereafter includes the uncertainty on the branching ratio, the detection efficiency and on the number of detected events.

### 4.2.1 Analysis method

#### $E_\gamma = 980.8 \text{ keV}$

The most dominant  $\gamma$ -ray emitted in the  $^8\text{He}$  decay comes from the simple  $\beta$  branch that feeds the first excited state of  $^8\text{Li}$  at 980.8 keV above its ground state. Observation of this  $\gamma$ -ray with the HPGe is shown in Figure 4.2. The two smaller lines at 964.72 and 968.98 keV are identified as  $\gamma$ -rays emitted from  $^{228}\text{Ac}$  nuclei contained within the concrete around the setup. These lines were also observed in background runs, with and without the cyclotrons running.

Some events can be observed very close to the 980.8 keV line. These events were not observed in any background runs. Furthermore, in runs where the radioactive beam was implanted as discussed in Section 3.1, these events distinctly follow the implantation cycle. Therefore, they are clearly related to the detection of the 980.8 keV  $\gamma$ -ray. Events above the peak are identified as pile-up events. The two small "bumps" below the peak around 975 keV are events with incorrectly measured energy due to the CFD technique used to trigger the electronic chain of the HPGe coupled with a relatively high detection rate.

All events above the flat background in the 972 to 990 keV range are considered to be true 980.8 keV events. Therefore, the data in this area were not fitted with a

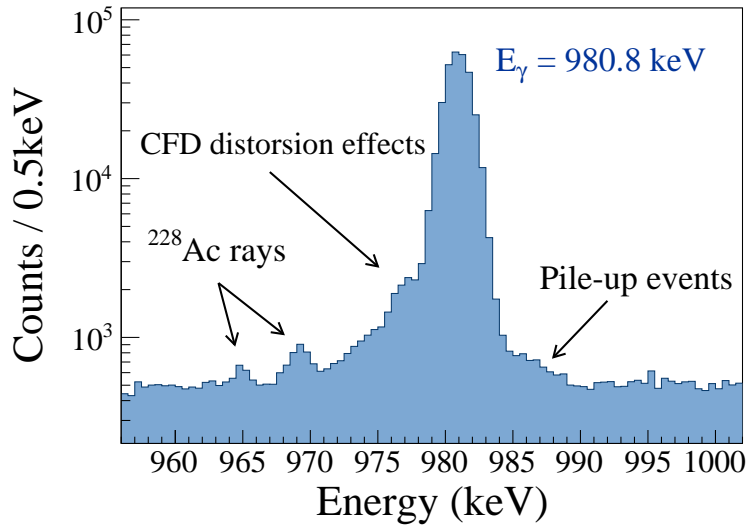


FIGURE 4.2 –  $\gamma$  spectrum at the vicinity of the 980.8 keV line. The 964.72 and 968.98 keV lines are background rays emitted from  $^{228}\text{Ac}$  nuclei present in the concrete of the experimental room. The small slope above the 980.8 keV line are pile-up events and the ”bumps” under are CFD distorsion effects as shown in Figure 3.10.

simple Gaussian distribution over a constant background, as this would overestimate the background parameter. Instead, the background per bin was first estimated by fitting the data with a constant in two 18 keV energy windows above and below 980.8 keV, where no lines can be observed. The two very close values were then averaged to obtain a final background parameter. This background is then subtracted from each bin in the observed statistics between 972 and 990 keV to obtain the final contribution of the 980.8 keV  $\gamma$ -ray. Finally, the bin error is modified to  $u'_{\text{bin}} = \sqrt{N_{\text{bin}} + u_{\text{bck}}^2}$ , where  $u_{\text{bck}}$  is the uncertainty on the background parameter returned by the fit and  $N_{\text{bin}} = u_{\text{bin}}^2$  is the original number of events in the bin.

### $E_\gamma = 477.6$ keV

Observation of the 477.6 keV  $\gamma$ -ray with the HPGe is shown in Figure 4.3. The 511 keV  $e^+e^-$  annihilation line is also shown in this figure as a comparison point. Fits with a Gaussian distribution were performed on both  $\gamma$ -rays. The standard deviation obtained for the 477.6 keV line is about 3 times larger than the resolution obtained for the 511 keV line. This peak broadening for the 477.6 keV  $\gamma$ -ray has already been observed in [108] studying the  $^8\text{He}$  decay.

This  $\gamma$ -ray comes from the deexcitation of a  $^7\text{Li}$  nucleus that is produced by the  $\beta n$  branches shown in Figure 4.1. Since  $m_{\text{Li}} \approx 7m_n$ , the kinetic energy is not completely taken away by the emitted neutron. Although smaller, a non-negligible fraction is also transferred to the  $^7\text{Li}$  nucleus as recoil energy. Therefore, the 477.6 keV  $\gamma$ -ray can be considered as emitted in flight inside the aluminum catcher, and the peak broadening observed in Figure 4.3 is only the result of a Doppler effect. Similarly to the 980.8 keV line, the background parameter per bin, modeled with a constant and returned by the

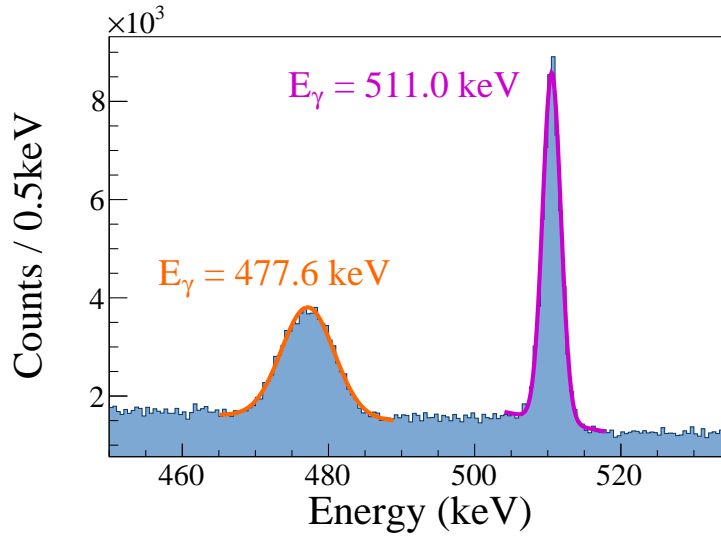


FIGURE 4.3 –  $\gamma$  spectrum at the vicinity of the 477.7 keV line. The 511 keV line comes from the  $e^+e^-$  annihilation. Fits with a Gaussian distribution performed on both lines are shown in orange for the 477.6 keV  $\gamma$  and in purple for the 511 keV  $\gamma$ .

fit, was used to measure the number of detected 477.6 keV photons between 468 and 478 keV. The bin error was also modified as described above for the 980.8 keV line.

### Neutron detection analysis

The energy spectra obtained from the  $^8\text{He}$  runs, displayed in Figure 4.4, looks very similar to those obtained with a  $^{252}\text{Cf}$  neutron source. The only main difference is in the low-energy peak, which contains more events in the  $^8\text{He}$  data because of a higher exposure to bremsstrahlung and  $\gamma$  radiations than with the neutron source. For each run, the total number of events within  $150 \leq E_{dep} \leq 820$  keV is taken into account, and the background is subtracted from the total number of events in that range. Removing the background had very little effect on the final statistics, since its contribution was usually about  $10^4$  times smaller than the total number of recorded events in that  $E_{dep}$  range.

### Silicon detector analysis

In the context of this analysis, the silicon detector measured the energy deposition of electrons emitted by  $^8\text{He}$  and  $^8\text{Li}$  nuclei. Data were analyzed using Geant4 simulations that reproduced the geometry of both the detector and its environment within the LIRAT beam line. It also reproduces the spatial distribution of the beam inside the aluminum foil. In the following, the simulation will be compared with data from two runs where the beam intensity reduction factors from the mechanical and electrostatic reductors were applied.

First, the detector was calibrated in energy by matching the positions of two different notable points observed in both the experimental data and the simulated data : the end point and the  $\approx 1.5$  MeV energy peak where most of the observed events are located. Then, each bin content in the histogram obtained with the simulation is scaled by a

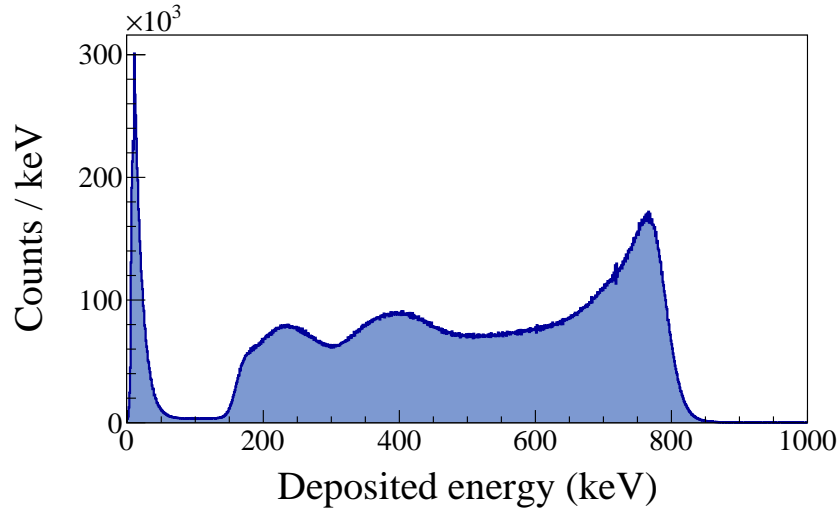


FIGURE 4.4 – Calibrated energy spectrum of TETRA obtained with one  $^8\text{He}$  run. The relative contribution of the peak with  $E_{dep} \leq 100$  keV is higher here than in Figure 3.3. This is because of the higher level of bremsstrahlung radiation during the  $^8\text{He}$  than with the  $^{252}\text{Cf}$  neutron source used for the calibration.

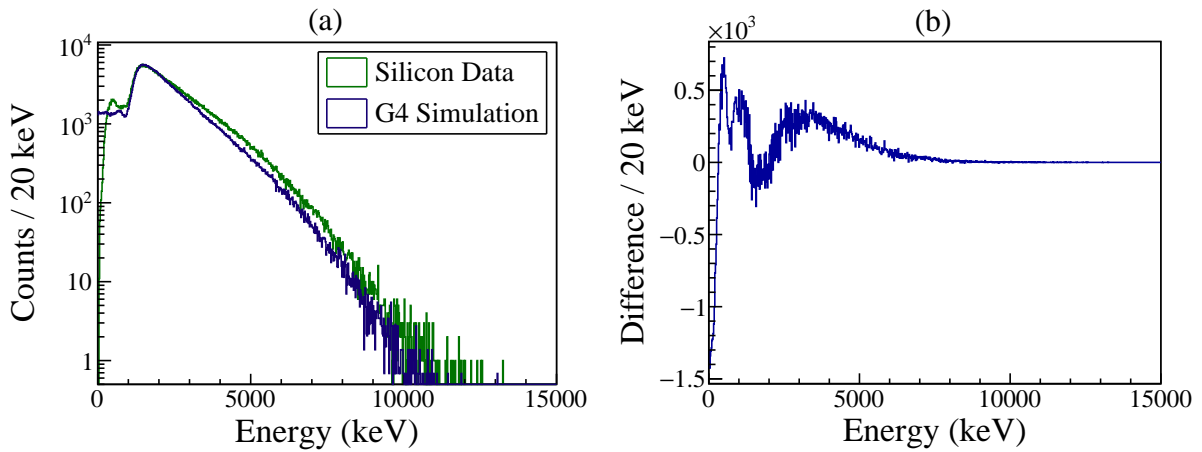


FIGURE 4.5 – (a) Measured (green line) and simulated (blue line) energy spectrum with the silicon detector for one  $^8\text{He}$  run. Each bin content in the simulated histogram are scaled down by a factor allowing to match the amplitude of the main peak around 1.5 MeV. (b) The difference in each bin between the measured and the simulated histogram after the scaling.

factor  $c_s$  to match the amplitude of the  $\approx 1.5$  MeV peak from the measured energy spectrum, as shown in Figure 4.5 (a). This scaling is performed only on a selection  $t_{\text{sel}}$  with sufficient statistics where the detection rate is stable to perform deadtime corrections while maintaining comparability between the simulated and observed energy spectrum. Finally, the average  $^8\text{He}$  beam intensity is calculated as follows :

$$r_0 = \alpha_R \alpha_{\text{DT}} \frac{c_s N_{\text{sim}}}{t_{\text{sel}}}, \quad (4.2)$$

where  $\alpha_R$  is the reduction factor and  $\alpha_{\text{DT}}$  is the deadtime correction factor. Finally,  $N_{\text{sim}}$  is the initial number of  $^6\text{He}$  nuclei used in the simulation. The difference between the simulated and the measured energy spectrum is then used to quantify the uncertainty.

## 4.2.2 Results of the calculations

All values for the average  $^8\text{He}$  beam intensity  $r_0$  obtained from the 980.8 keV line with the HPGe and neutron detection with TETRA are displayed in Table 4.1. Two values obtained separately with the silicon detector are also shown in that table. The values computed with neutron and  $\gamma$  monitoring agree well with each other. The relative discrepancies are mostly around 10%, which largely corresponds to the overall uncertainty level of the branching ratios and the detection efficiencies used for the calculations. Therefore, we can conclude that our results agree well with the branching ratios for the  $\beta$  and  $\beta n$  branches from [108].

Conversely, we observe a large discrepancy between the beam intensities obtained from the two  $\gamma$ -ray lines. For each run, the intensity values obtained from the 477.6 keV line were on average  $\approx 1.51$  times higher than those obtained from the 980.8 keV line. The ratios  $r_0(477.6\text{keV})/r_0(980.8\text{keV})$  for each run are shown in Figure 4.6. Changing the model from a constant to a first-order polynomial for the background parameter in the 477.6 keV line analysis had little to no impact on the final result. Furthermore, different models were used to evaluate the detection efficiency at both HPGe positions, with relative variations around  $\lesssim 3\%$  and therefore not enough to explain this large difference. The last component that can play a role here is the  $\text{Br}(477.6\text{keV}) = 5.1(6)\%$  branching ratio used to feed the first excited state of  $^7\text{Li}$ . In fact, since the  $r_0$  values computed with the 980.8 keV line match relatively well with the  $r_0$  values from neutron detection, if a systematic effect was not taken into account in the HPGe analysis, it should alter the  $r_0$  values from both the 477.6 keV line and the 980.8 keV line. Therefore, explaining this difference only through the branching ratio would require a new value of  $\text{Br}(477.6\text{keV}) = 7.7(9)\%$ .

## 4.2.3 $^8\text{He}$ beam intensity versus primary beam intensity

To compare the  $r_0$  values obtained with the silicon detector with those computed with TETRA and the HPGe, we plot them with respect to the primary  $^{13}\text{C}$  beam intensity on the  $^{12}\text{C}$  target measured with the Ti. For every run, we calculated the mean primary beam intensity over the entire run duration. The result is shown in Figure 4.7. In a few runs, we observed some failures of the complementary heating system of the target-ion

HPGe position	Run index	$r_0 \times 10^{-3} (^8\text{He}\cdot\text{s}^{-1})$			Implantation cycle
		HPGe	TETRA	Silicon	
21.9 cm	1	$152 \pm 8$	$190 \pm 24$		Continuous
	2	$193 \pm 9$	$216 \pm 27$		$t_{\text{ON}} = 0.3\text{s} + t_{\text{OFF}} = 5\text{s}$
	3	$185 \pm 9$	$207 \pm 26$		$t_{\text{ON}} = 0.3\text{s} + t_{\text{OFF}} = 5\text{s}$
43.9 cm	4	$470 \pm 24$	$550 \pm 68$		Continuous
	5	$468 \pm 24$	$545 \pm 67$		Continuous
	6	$479 \pm 24$	electronic shift		$t_{\text{ON}} = 3\text{s} + t_{\text{OFF}} = 7\text{s}$
	7	$403 \pm 21$	electronic shift		$t_{\text{ON}} = 3\text{s} + t_{\text{OFF}} = 7\text{s}$
	8	$371 \pm 19$	$399 \pm 46$		$t_{\text{ON}} = 3\text{s} + t_{\text{OFF}} = 7\text{s}$
	9	$385 \pm 20$	$414 \pm 48$		$t_{\text{ON}} = 3\text{s} + t_{\text{OFF}} = 7\text{s}$
	10	$404 \pm 21$	$438 \pm 54$		$t_{\text{ON}} = 3\text{s} + t_{\text{OFF}} = 7\text{s}$
	11	$402 \pm 21$	$435 \pm 54$		$t_{\text{ON}} = 3\text{s} + t_{\text{OFF}} = 7\text{s}$
	Si1			$239 \pm 14$	Continuous
	Si2			$445 \pm 61$	Continuous

TABLE 4.1 – Average  $^8\text{He}$  beam intensity  $r_0$  from neutron detection with TETRA, observation of the  $E_\gamma = 980.8$  keV line with the HPGe and electron monitoring with the silicon detector in the LIRAT line.

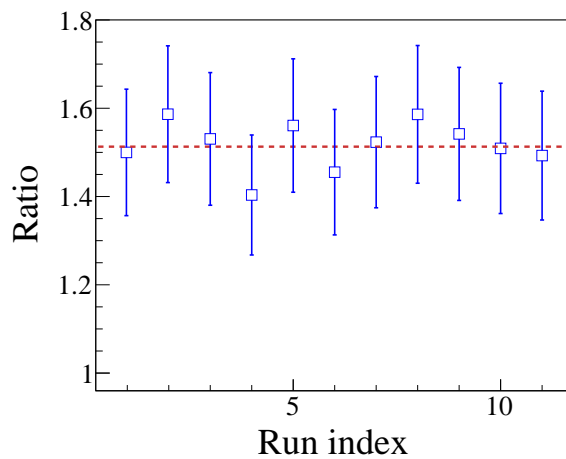


FIGURE 4.6 – Ratios of average  $^8\text{He}$  beam intensities  $r_0$  computed from the two different  $\gamma$  lines emitted in the  $^8\text{He}$  scheme. The dashed line in red is a fit performed with a constant. The value returned by the fit is  $1.51 \pm 0.05$ .

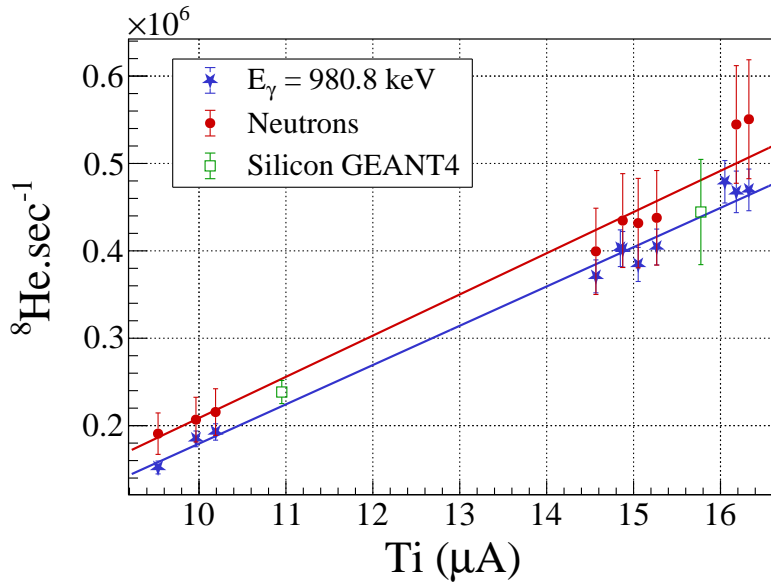


FIGURE 4.7 – Average  $^8\text{He}$  beam intensity with respect to the primary  $^{13}\text{C}$  beam intensity on target measured with the Ti. The red and blue lines are linear fits performed merely to guide the eye more than to show a particular trend.

source. Although the primary beam was still hitting the target as monitored by the Ti, we saw a complete drop in the detection rate with all detectors, slowly increasing back to normal as the temperature of the source went back up. These periods were excluded from the analysis and the  $r_0$  values presented in Table 4.1 have already been adjusted accordingly. In conclusion, the two  $r_0$  values measured using the silicon detector nicely match the trend observed for the values obtained using TETRA and the HPGe, improving the confidence we have in their calculations.

## 4.3 Detection efficiency of the plastic scintillator

### 4.3.1 Data analysis of the plastic scintillator

In the following analysis, only the runs in which the  $^8\text{He}$  beam was implanted periodically were used. The runs where the plastic scintillator was closest to the aluminum catcher are labeled 2 and 3 in Table 4.1. The runs labeled 6 to 11 were performed with the plastic scintillator in the farthest position, but only runs 6, 7 and 8 were performed with the trigger threshold width at 2 ns, as runs 2 and 3. Runs 9, 10 and 11 were carried out with a trigger width of 4 ns. The distributions of the detected events with respect to their time  $t_c$ , in each implantation cycle, are shown in Figure 4.8 where each panel corresponds to a particular position and trigger width of the plastic scintillator. In addition, each panel represents the aggregation of all runs performed within the same configuration, but the following analysis was performed on each individual run. In Figure 4.8 (a) and (c) the

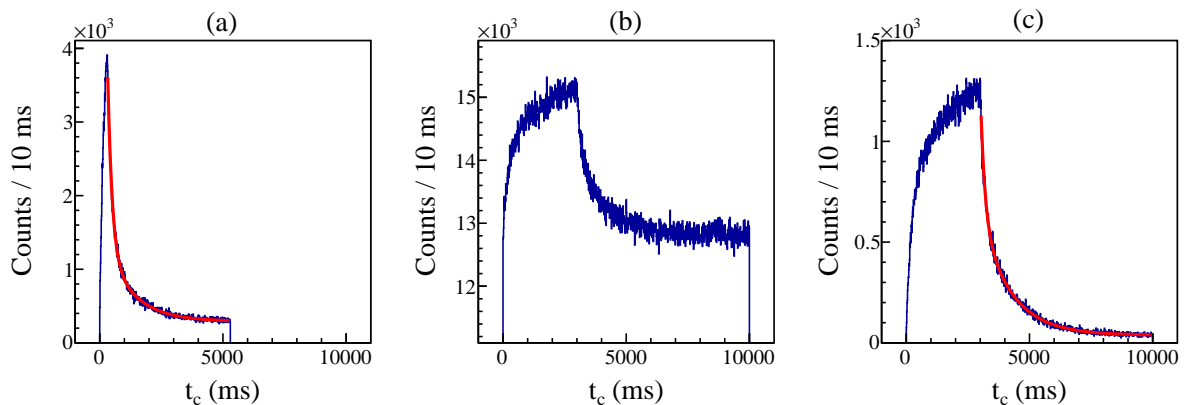


FIGURE 4.8 – Sum of all  $t_c$  histograms acquired with the plastic scintillator with respect to its position and trigger threshold width. (a) was obtained with runs 2 and 3 when the plastic was in the closest position from the catcher with a 2 ns trigger width. (b) was obtained with runs 6, 7 and 8 when the plastic was in the farthest position from the catcher with a 2 ns trigger width. Finally, (c) was obtained with runs 9, 10 and 11 when the plastic was also at the farthest position but with a trigger width of 4 ns. The solid red lines in (a) and (c) are fits performed using Equation 4.3

data between  $t_{\text{ON}}$  and  $t_{\text{ON}} + t_{\text{OFF}}$  were fitted using the following model :

$$N(t_c) = \sum_{i=^8\text{He}, ^8\text{Li}} N_i e^{-\lambda_i(t_c - t_{\text{ON}})} + b, \quad (4.3)$$

where  $\lambda_i$  is the radioactive constant and  $N_i$  is the amplitude at  $t_c = t_{\text{ON}}$  of the  $i$ -th nucleus, and  $b$  represents the background parameter per bin. All fits were performed using the log likelihood method provided by ROOT without constraining any of the parameters in the model. All fits returned  $^8\text{He}$  and  $^8\text{Li}$  lifetimes that were consistent with what can be found in the literature. For unclear reasons, the fits for runs 6, 7 and 8 did not converge even when the parameters were constrained. Consequently, the background parameter was estimated by fitting the data within  $8\text{ s} \leq t_c \leq 10\text{ s}$  with a simple constant. In addition, panels (a) and (b) show data acquired over approximately the same period of time, highlighting the behavior of the background level as a function of the plastic position. Although uncertain, this effect could be due to a possible cable issue leading to a higher level of pedestal effects. This is also emphasized by the difference between panels (b) and (c), where the change in the trigger threshold width drastically reduced the background level.

Once the background parameter is estimated, we can use it to calculate the contribution of the  $^8\text{He}$  and  $^8\text{Li}$  nuclei in each run. Finally, the detection efficiency of the plastic scintillator was calculated using Equation 4.1 for all runs. We used the average  $^8\text{He}$  beam intensities assessed from the 980.8 keV line and compared them with the statistics corresponding to the detection of electrons with the plastic scintillator. All detection efficiency values are listed in Table 4.2. We calculate the mean detection efficiency  $\bar{\epsilon}$  for each group of runs performed under the same configuration. From this we obtain two efficiency values that correspond to the two different positions of the plastic scintillator

Plastic position	Trigger width (ns)	Run index	$(\varepsilon_\beta \times 10^4)$	$(\bar{\varepsilon}_\beta \times 10^4)$
Closest	2	2	$10.3 \pm 0.5$	$10.3 \pm 0.5$
		3	$10.3 \pm 0.5$	
		6	$2.11 \pm 0.11$	
Farthest	2	7	$2.07 \pm 0.11$	$2.05 \pm 0.11$
		8	$1.97 \pm 0.10$	
		9	$1.01 \pm 0.05$	
Farthest	4	10	$1.10 \pm 0.05$	$1.07 \pm 0.05$
		11	$1.09 \pm 0.05$	

TABLE 4.2 – Detection efficiency values of the plastic scintillator for each run with respect to its position and its trigger threshold width. The last column is an average efficiency value for a specific configuration.

with a trigger width threshold of 2 ns, which are the configurations of the plastic scintillator during the  $^6\text{He}$  runs. The first value in the closest position (HPGe at  $\approx 23$  cm) is  $\varepsilon_\beta^C = (1.03 \pm 0.05) \times 10^{-3}$  and the second in the farthest position (HPGe at  $\approx 43$  cm) is  $\varepsilon_\beta^F = (2.05 \pm 0.11) \times 10^{-4}$ . Finally, the analysis of runs 9 through 11 shows that both the background level and the detection efficiency are completely different with a 4 ns trigger width. This explains why the analysis of the radioactive  $\beta$  source runs performed at the very end of the experiment was not conclusive.

### 4.3.2 G4beamline simulations

The efficiency values obtained from the analysis above were obtained for  $\beta$  decay with predominant  $Q_\beta$  values of  $\approx 10$  MeV for the  $^8\text{He}$  decay and  $\approx 13$  MeV for the  $^8\text{Li}$  decay. In contrast, the  $^6\text{He}$  nucleus has a smaller value of  $Q_\beta = 3.5$  MeV. We performed G4beamline simulations [110] to investigate how this difference in  $Q_\beta$  values can affect the detection efficiencies of the plastic scintillator. G4beamline is an open source Geant4-based simulation program designed to be more accessible and user-friendly than Geant4. It is mainly used to simulate the transport and interaction of particles in beamlines, but it can also be used for different purposes, as it includes all Geant4 physics lists.

#### Geometry of the simulation

The purpose of this simulation was to assess a correction factor for the plastic scintillator due to the difference in  $Q_\beta$  values between the involved nuclei. For this purpose, the geometries of TETRA and of the HPGe have been simplified to reproduce the immediate environment of the  $\beta$ -particles. In this simulation, TETRA simply consists of a polyethylene cylinder with an inner radius of 65 mm and an outer radius of 480 mm. In this simulation, no  $^3\text{He}$  counters were included. The beamline and the catcher at the end were reproduced according to the official plans of the experiment. The center of the aluminum

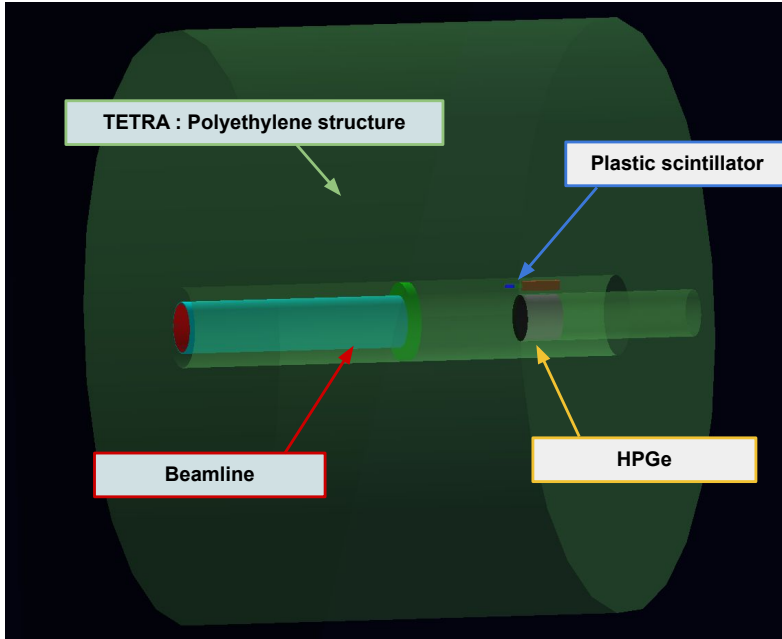


FIGURE 4.9 – Geometry of the experimental setup with the HPGe and plastic scintillator at the closest position from the catcher used in the G4beamline simulations.

catcher at the end of the line was placed at the point of origin with coordinates  $(0, 0, 0)$  in the Cartesian coordinate system. In the simulation, HPGe consists of a germanium crystal in the form of a cylinder with no inner radius and an outer radius value of 36.5 mm. The crystal was encapsulated in an aluminum cap that was also modeled with a cylinder of inner radius 37.8 mm and outer radius 38.1 mm. The thin 0.6 mm carbon window in front of the crystal was also included. The plastic scintillator is placed on top of the HPGe and consists of a vinyltoluene plastic box with a  $5 \times 5 \text{ mm}^2$  surface in the  $xy$  plane and 15 mm length along the  $z$  axis. This plastic box was encapsulated in an aluminized tape modeled with an aluminum box. The photomultiplier tube of the plastic scintillator was modeled by a copper box with a surface  $15 \times 15 \text{ mm}^2$  in the  $xy$  plane and a length 60 mm along the  $z$  axis. The relative position of the plastic scintillator with respect to the HPGe does not change when the HPGe is in the closest or farthest position from the catcher. The final geometry with the HPGe at  $\approx 22 \text{ cm}$  from the catcher is shown in Figure 4.9.

### Rejection method to reproduce the $^6,8\text{He}$ and $^8\text{Li}$ decays

The decay of radioactive isotopes is not implemented in G4beamline. To simulate the production of  $\beta$  particles, one has to produce its own input file that the software can call on. Each line of this file corresponds to the nature of the simulated particle (an electron, a proton, etc.), the initial position (using  $x$ ,  $y$  and  $z$  coordinates) and the initial momentum (using  $p_x$ ,  $p_y$  and  $p_z$  coordinates). In Monte Carlo simulations, the rejection method allows the generation of events with specific characteristics that fit to a known probability distribution function. In our case, we need to simulate the initial properties of an electron emitted in the  $\beta$  decay of one of the nuclei involved. More specifically, we

used the rejection method to produce an initial distribution of electrons with respect to their momentum.

The probability density function (pdf) with respect to the momentum of the electron  $\omega(p_e)$  produced in a  $\beta$  decay can be written as :

$$\omega(p_e) = p_e^2 \left( Q_\beta - (\sqrt{p_e^2 + m_e^2} - m_e) \right)^2, \quad (4.4)$$

where  $p_e$  is the electron momentum,  $m_e$  the electron mass and  $Q_\beta$  is the total energy available in the corresponding decay branch. This function reproduces the bell-shaped electron momentum distribution. In our case, it is not required that the pdf is normalized. To randomly generate a  $p_e$  distribution, one first evaluates the maximum momentum value :

$$p_{e,max} = \sqrt{(Q_\beta + m_e)^2 - m_e^2}, \quad (4.5)$$

as well as the maximum value of the pdf  $\omega_{max}$  which can be readily obtained by visualizing the pdf. Next, using the TRandom3 random generator class available in ROOT, random  $p_{e,rand}$  and  $\omega_{rand}$  values are generated in the intervals  $[0, p_{e,max}]$  and  $[0, \omega_{max} + \delta_\omega]$ , respectively, where  $\delta_\omega$  is a small positive number to ensure that there are no edge effects altering the production of our distribution. The amplitude of  $\delta_\omega$  only affects the time it takes to produce the desired number of events in the distribution. Finally,  $\omega(p_{e,rand})$  is compared to  $\omega_{rand}$ . If  $\omega_{rand} \leq \omega(p_{e,rand})$ , the event is saved as it falls under the pdf; otherwise it is rejected.

### Initial position and direction

Once a  $p_e$  value is saved we can randomly generate angles  $\theta$  and  $\phi$  corresponding to the polar and azimuthal angle respectively in the spherical coordinate system. We consider all the involved  $\beta$  decay branch as isotropic. The following equations are therefore used to formulate their distribution :

$$\theta = \arccos(2R_\theta - 1), \quad (4.6)$$

$$\phi = 2\pi R_\phi, \quad (4.7)$$

where  $R_\theta$  and  $R_\phi$  are randomly generated numbers between 0 and 1. Projection of the initial electron momentum value over the  $x$ ,  $y$  and  $z$  axes are computed as follows :

$$p_{ex} = p_e \sin(\theta) \cos(\phi), \quad (4.8)$$

$$p_{ey} = p_e \sin(\theta) \sin(\phi), \quad (4.9)$$

$$p_{ez} = p_e \cos(\theta). \quad (4.10)$$

Finally, the initial position of the electron inside the aluminum catcher along the  $x$ ,  $y$  and  $z$  axes can be generated as well. In our simulation, the plane formed by the  $x$  and  $y$  axes corresponds to the plane formed by the catcher. In this plane, the density of particles within the catcher is modeled as a 2D Gaussian centered in the middle of the beam catcher with  $\sigma_x = \sigma_y = 3.82$  mm, which is consistent with measurements made with

Parent nucleus	Decay branch	$Q_\beta$ (MeV)	Probability
$^8\text{He}$	$\beta$	9.68	0.831
	$\beta n$	6.36	0.16
	$\beta t$	0.99	0.009
$^8\text{Li}$	$\beta$	12.98	1
$^6\text{He}$	$\beta$	3.51	1

TABLE 4.3 – All  $Q_\beta$  values used to produce the initial  $p_e$  distributions for each decay branch with their associated emission probability.

beam profilers in the LIRAT line. To simplify the implantation of  $^6\text{He}$  or  $^8\text{He}$  inside the catcher, we consider the probability that the initial position with respect to the  $z$  axis of the decay is the same over the entire width ( $150\mu\text{m}$ ) of the catcher.

### Numerical values for each decay branch

To date, no experiment has measured the separate branching ratio for each  $\beta n$  branch. A recently published paper shows how it implemented the decay of  $^8\text{He}$  in Geant4 using the same emission probability at 8% for each branch. The real decay scheme of  $^8\text{He}$  is expected to be more complicated than what is actually available in the literature. A better determination of all involved levels and their associated branching ratio is currently under examination at the ISOLDE decay station, since this nucleus (along with  $^9\text{Li}$ ) plays an important role in reactor antineutrino experiments. To simplify the picture and since these particular branches represent  $\lesssim 9\%$  of all events in the simulation, they were aggregated into one intermediate state at around 4.3 MeV above the  $^8\text{Li}$  ground state with a branching ratio of 16%. The other  $Q_\beta$  and branching ratio values involved in the  $^8\text{He}$  decay remain as discussed in Section 4.1. The  $\beta$  decay of the  $^8\text{Li}$  daughter nucleus is taken to feed the 3.03 MeV level of the unbound  $^8\text{Be}$  nucleus 100% of the time. Finally, the  $^6\text{He}$  decay is as described in Section 2.3.3 but the  $\beta d$  channel is not reproduced in the following work as its branching ratio is very small. All the values involved in the following G4beamline simulations are summarized in Table 4.3.

### Result of the simulations

A total of four G4beamline simulations were performed. Each simulation corresponds to a specific isotope ( $^6\text{He}$  or  $^8\text{He} + ^8\text{Li}$ ) at a certain position of the plastic scintillator. Two files corresponding to  $10^8$  decays of  $^6\text{He}$  and  $^8\text{He}$  were produced using the rejection method described above. In the  $^8\text{He}$  file, a total of  $0.831 \times 10^8$  events are also generated to reproduce the decay of  $^8\text{Li}$ . The course of the electron is processed by the software until it has lost all of its kinetic energy, and the simulation continues with the next electron in the input file. For each electron, we register the total energy the particle loses inside the plastic scintillator. The energy spectra obtained for each simulation are shown in Figure 4.10.

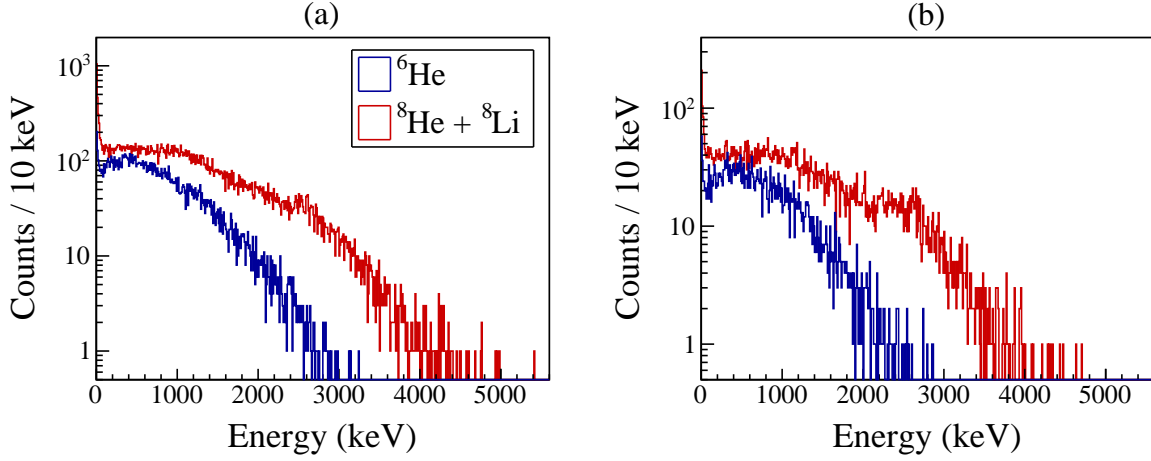


FIGURE 4.10 – Results of the G4beamline simulations. (a) and (b) show the energy spectra obtained with the plastic scintillator in the closest and farthest position from the catcher, respectively, for each isotopes.

Position	$\alpha_\varepsilon(E_{dep} \geq 10 \text{ keV})$	$\alpha_\varepsilon(E_{dep} \geq 1 \text{ keV})$	$(\varepsilon_{\text{plastic}} \times 10^4)$
Closest	$0.85 \pm 0.01$	$0.84 \pm 0.01$	$8.67 \pm 0.44$
Farthest	$0.77 \pm 0.02$	$0.76 \pm 0.02$	$1.57 \pm 0.09$

TABLE 4.4 – Correction factors with respect to the position and threshold of the plastic scintillator. The last column gives the corrected efficiency values obtained with  $\alpha_\varepsilon(E_{dep} \geq 10 \text{ keV})$ .

From these spectra, we can evaluate a correction factor that can be applied to the detection efficiencies obtained in Section 4.3 to achieve efficiency values that are more appropriate for the  ${}^6\text{He}$  analysis. To do this, we simply need to compare the number of events recorded by the plastic scintillator at the same position between the two different parent nuclei. Therefore, the correction factor  $\alpha_\varepsilon$  can be written as :

$$\alpha_\varepsilon = \frac{N({}^6\text{He})}{N({}^8\text{He} + {}^8\text{Li})} \times 1.831. \quad (4.11)$$

We roughly estimate the energy threshold of the plastic scintillator to be around 10 keV. Therefore, the correction factor at both positions will be computed considering only events with  $E_{dep} \geq 10 \text{ keV}$ . The results are compiled in Table 4.4. In addition, the correction factors for events with  $E_{dep} \geq 1 \text{ keV}$  are also computed, showing that they have little to no dependence with respect to the threshold. Finally, these simulations allow us to compute the final detection efficiency values for the plastic scintillator that will be used in the following  ${}^6\text{He}$  analysis :  $\varepsilon_\beta^C = (8.67 \pm 0.44) \times 10^{-4}$  and  $\varepsilon_\beta^F = (1.56 \pm 0.09) \times 10^{-4}$ .

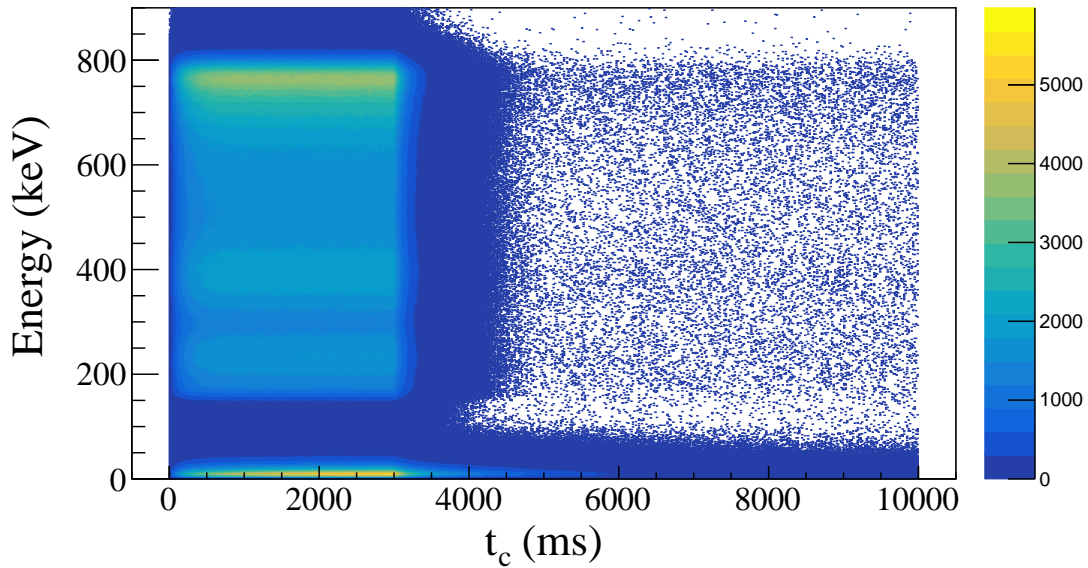


FIGURE 4.11 – Deposited energy (keV) of an event in TETRA with respect to its time  $t_c$  within an implantation cycle. This figure shows all data obtained with the 4 runs

## 4.4 $^8\text{He}$ half-life measurement

The  $^8\text{He}$  nucleus is an unstable nucleus with a half-life value of  $119.1 \pm 1.2$  ms [111]. We aim to improve this value using data from the neutron detector TETRA and runs in which the radioactive beam was implanted periodically. A total of 6 runs are used for the analysis. Two at the beginning of the experiment with an implantation cycle of 5.3 seconds ( $t_{\text{ON}} = 0.3$  second of beam implantation and  $t_{\text{OFF}} = 5$  seconds of decay time) with an average  $^8\text{He}$  beam intensity of around  $2.0 \times 10^5$  pps. Four at the end of the campaign with an implantation cycle of 10 seconds ( $t_{\text{ON}} = 3$  seconds of beam implantation and  $t_{\text{OFF}} = 7$  seconds of decay time) with an average  $^8\text{He}$  beam intensity of around  $4.0 \times 10^5$  pps. For each run, the data was stacked in one histogram giving the number of detected events with respect to their time  $t_c$  in the implantation cycle. Events recorded in TETRA can arise from different sources : i) neutron detection from the  $^8\text{He}$  decay or the ambient background, ii) bremsstrahlung detection due to  $\beta$  particles emitted from the  $^8\text{He}$  and  $^8\text{Li}$  decay. The purity of the  $^8\text{He}$  beam ensures that no other neutron-emitting nuclei were implanted in the catcher during the experiment. The measured deposited energy in the  $^3\text{He}$  gas can be used to discriminate the origin of the event between i) and ii). Spurious events from microdischarges, spallations, or any other unknown origin can also be recorded with TETRA but do not have specific deposited energy or temporal signatures.

### 4.4.1 First analysis

#### Event selection

Figure 4.11 is a 2D histogram showing the energy of an event with respect to its time  $t_c$  in 10 second cycles. From this histogram, we can make a selection of events according to their deposited energy inside TETRA. The impact of this selection is shown in Figure

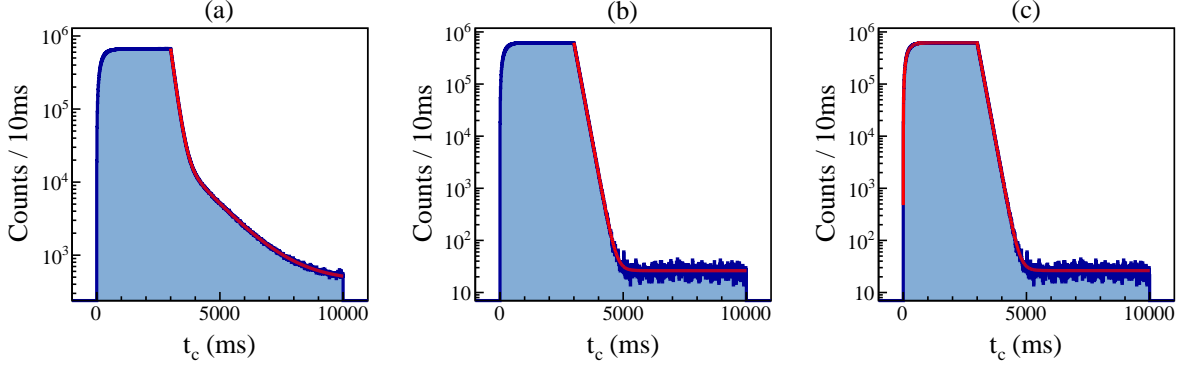


FIGURE 4.12 – Distribution of events with respect to their time  $t_c$  within an implantation cycle for 10 s cycles. (a) shows all events with  $0 \leq E_{dep} \leq 850$  keV while (b) and (c) show the events within  $150 \leq E_{dep} \leq 850$  keV. Each solid red lines correspond to a fit with a model defined in Section 4.4.1.

4.12, in which panel (a) shows all events recorded with TETRA, including bremsstrahlung, while panels (b) and (c) show events corresponding to neutron detection only. This simple selection almost entirely eliminates the contribution of bremsstrahlung events, resulting in a  $t_c$  distribution that largely follows the lifetime of  $^8\text{He}$  only. Moreover, this selection is large enough to ensure that all events corresponding to neutron detection are taken into account in the following analysis.

### Fit models

Each  $t_c$  distribution in Figure 4.12 can be fitted with a model to obtain half-life values. As with the plastic scintillator, the histogram that includes the bremsstrahlung events in Figure 4.12 (a) is fitted between  $t_c = t_{\text{ON}}$  and  $t_c = t_{\text{ON}} + t_{\text{OFF}}$  with the model described by Equation 4.3. For panel (b), the histogram is fitted within the same time range, and the model we used is a simple exponential decay model with a constant background parameter. Although event selection is the same between (b) and (c), the latter histogram is fitted with a model that covers the entire length of an implantation cycle. The equations that describe the full behavior are :

$$N_1(t_c) = \phi(1 - e^{-t_c/\tau}) + b, \quad (4.12)$$

$$N_2(t_c) = \phi(e^{t_{\text{ON}}/\tau} - 1)e^{-t_c/\tau} + b, \quad (4.13)$$

where  $N_1(t_c)$  and  $N_2(t_c)$  correspond to the fit before and after  $t_c = t_{\text{ON}}$  respectively. The derivation of these equations and the interpretation of the parameter  $\phi$  are given in the next chapter in Section 5.1.

All fits are performed with the log likelihood method provided by ROOT. The results of each fit performed for  $t_c \leq t_{\text{ON}}$  are summarized in Table 4.5. The uncertainties are statistical uncertainties only returned by each fit. The half-lives obtained for both  $A = 8$  isobars agree well with what can be found in the literature.

Implantation cycle	Event selection	$t_{1/2}(^8\text{He})$ (ms)	$t_{1/2}(^8\text{Li})$ (ms)
$t_{\text{ON}} = 0.3$ s and $t_{\text{OFF}} = 5$ s	$0 \leq E_{\text{dep}} \leq 850$ keV	$119.73 \pm 0.13$	$855.28 \pm 13.72$
	$150 \leq E_{\text{dep}} \leq 850$ keV	$119.49 \pm 0.06$	/
$t_{\text{ON}} = 3$ s and $t_{\text{OFF}} = 7$ s	$0 \leq E_{\text{dep}} \leq 850$ keV	$119.84 \pm 0.07$	$840.79 \pm 1.53$
	$150 \leq E_{\text{dep}} \leq 850$ keV	$119.61 \pm 0.04$	/

TABLE 4.5 –  $^8\text{He}$  and  $^8\text{Li}$  half-life values obtained from the fits with respect to the implantation cycle and the event selection.

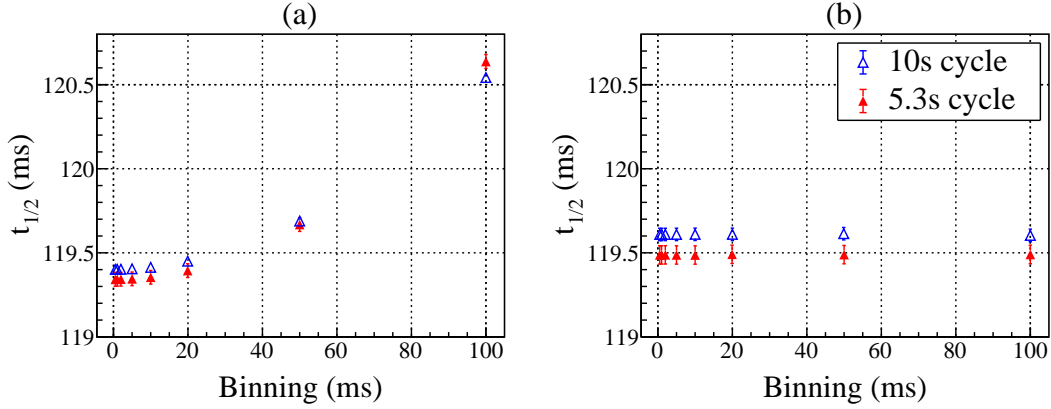


FIGURE 4.13 – Fit results with respect to the binning of the histogram. Panel (a) shows values obtained by fitting the whole cycle with Equations 4.12 and 4.13. Panel (b) shows values obtained by fitting the data for  $t_c \geq t_{\text{ON}}$  with an exponential decay model and a constant background parameter.

### Binning effect

Using events within  $150 \leq E_{\text{dep}} \leq 850$  keV, we can compare the  $^8\text{He}$  half-life values obtained by fitting the whole cycle or only the decaying part with respect to the bin width of the histogram. The results of each fit for widths between 0.5 and 100 ms are shown in Figure 4.13. If the results for fits on the data with  $t_c \geq t_{\text{ON}}$  are very stable with respect to the binning, the same cannot be said for fits on the whole cycle, as strong variations on the returned values  $t_{1/2}$  can be observed in Figure 4.13 (a), as well as a strong disagreement with the values obtained in Figure 4.13 (b). This binning effect can be explained by local instabilities in the radioactive beam intensity (and, therefore, the detection rate) that are not taken into account by the model. Indeed, such non-statistical fluctuations can affect the determination of  $t_{1/2}$ . Furthermore, since  $t_{1/2}(^8\text{He}) \approx 120$  ms, it takes  $\lesssim 1$  s to reach the detection rate at equilibrium. A sufficiently large bin width coupled with these local beam instabilities can lead to the observed binning dependence. Finally, these beam fluctuations do not matter in the region  $t_c \geq t_{\text{ON}}$  as only the implanted population at  $t_c = t_{\text{ON}}$  will contribute to the detection rate. Therefore, only the data with  $t_c \geq t_{\text{ON}}$  will be used in the following work.

### 4.4.2 Deadtime corrections

It takes  $20\mu\text{s}$  of non-paralyzable dead time for the DAQ system to process and record a signal from one  $^3\text{He}$  counter. Although the instantaneous rate per counter was not very high even for counters located in the first layer of TETRA, this deadtime can play a role in the observed  $\approx 1/1000$  discrepancy shown in Figure 4.13 (b). In the following, the impact of this dead time on the returned  $^8\text{He}$  values is investigated.

#### Evaluation of the real detection rate

To study these effects, we first need to evaluate the instantaneous detection rate for each counter at all times  $t_c \geq t_{\text{ON}}$ . Cycles without enough statistics (owing to a drop in beam intensity) were discarded in the following analysis. Without any deadtime, the detection rate in the decay part of each counter can be written as :

$$R_{i,j}(t_c) = R_{i,j}^{(1)} e^{-(t_c - t_{\text{ON}})/\tau_{\text{He}}} + R_{i,j}^{(2)} e^{-(t_c - t_{\text{ON}})/\tau_{\text{Li}}} + B_{i,j}, \quad (4.14)$$

where  $R_{i,j}^{(1)}$  and  $R_{i,j}^{(2)}$  are the initial rates at  $t_c = t_{\text{ON}}$  for each nuclei with subscripts  $i$  and  $j$  referring to the counter and the cycle respectively. The parameter  $B_{i,j}$  is a constant that describes the background detection rate. The model representing the observed detection rate  $r_{i,j}(t_c)$  for each individual counter  $i$  and cycle  $j$  taking into account the deadtime is :

$$r_{i,j}(t_c) = \frac{R_{i,j}(t_c)}{1 + \Delta R_{i,j}(t_c)}, \quad (4.15)$$

where  $\Delta$  is the deadtime.

The statistics per counter and per cycle were not high enough to properly fit the data directly with the latter model. To overcome this, we approximated TETRA as one detector with a single event line and a nonparalyzable deadtime of  $21\mu\text{s}$  imposed offline, as shown in Figure 4.14. The data is then stacked in one histogram for each cycle and fitted using Equation 4.15. Half-lives of 119.1 ms and 839.9 ms were used as nominal values for  $^8\text{He}$  and  $^8\text{Li}$  respectively. This allowed us to estimate the real detection rate  $R_j(t_c)$  of TETRA approximated to a single detector for each cycle  $j$  and for each component  $R_j^{(k)}$  ( $k = 1, 2$ ) and  $B_j$  in the model. The evaluation of the individual contribution of each counter to the global detection rate  $R_j(t_c)$  is the only step left to determine each  $R_{i,j}(t_c)$  value.

#### Individual counter contribution and correction

To obtain the contribution of each counter to the total detection rate per cycle  $R_j(t_c)$ , we first produce a  $t_c$  histogram containing the data of all selected cycles within a run for all individual counters. Then, all these histograms are summed to produce a single  $t_c$  distribution for TETRA. No additional deadtime is imposed offline here. Finally, the data on each individual counter histogram is fitted with the following model :

$$N_i(t_c) = N_i^{(1)} e^{-(t_c - t_{\text{ON}})/\tau_{\text{He}}} + N_i^{(2)} e^{-(t_c - t_{\text{ON}})/\tau_{\text{Li}}} + B_i, \quad (4.16)$$

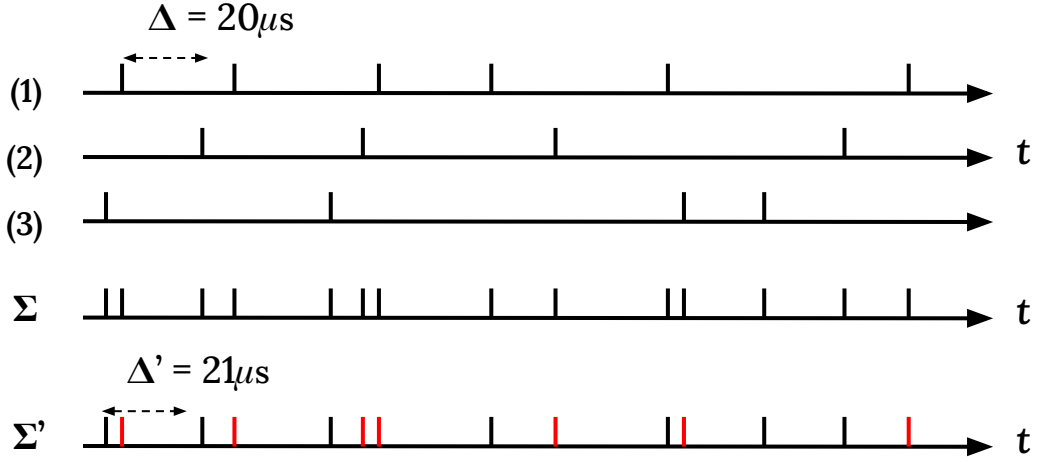


FIGURE 4.14 – Example showing the event line of three different counters from TETRA and their sum  $\Sigma$ . Events discarded by imposing an offline deadtime (here labeled  $\Delta'$ ) are shown in red on the  $\Sigma'$  line. This is used in the determination of  $R_j(t_c)$  only.

where  $N_i(t_c)$  is similar to  $R_{i,j}(t_c)$  in Equation 4.14 except that all cycles within a run are aggregated into one histogram, therefore giving the total recorded dose by a single counter instead of the instantaneous detection rate. The same model is used on each combined  $t_c$  distribution for TETRA giving access to  $N(t_c)$ . Finally, the relative efficiency (individual contribution) for each component in the model, for each counter and for each run is computed as :

$$\alpha_{N^{(k)},i} = \frac{N_i^{(k)}}{N^{(k)}} \quad \text{and} \quad \alpha_{B,i} = \frac{B_i}{B}, \quad (4.17)$$

for both radioactive component (superscript  $(k)$ ) and the background component respectively. Such relative efficiency coefficients with respect to the counter index obtained for one run are shown in Figure 4.15.

To finally achieve an evaluation of the real detection rate  $R_{i,j}(t_c)$  for each counter  $i$  at the time  $t_c$  in the cycle  $j$ , we simply have to compute :

$$R_{i,j}(t_c) = \alpha_{N^{(1)},i} R_j^{(1)}(t_c) + \alpha_{N^{(2)},i} R_j^{(2)}(t_c) + \alpha_{B,i} B_j. \quad (4.18)$$

Finally, we can produce corrected  $t_c$  histograms for each run by applying a weight  $w_{i,j}(t_c)$  to each event in the  $150 \leq E_{dep} \leq 850$  keV range like :

$$w_{i,j}(t_c) = 1 + \Delta R_{i,j}(t_c), \quad (4.19)$$

where  $\Delta$  is a deadtime imposed offline to each individual counter. This procedure has been applied for several values of  $\Delta$  that range from  $42 \mu\text{s}$  to 10 ms. An example with  $\Delta = 1$  ms is shown in Figure 4.16.

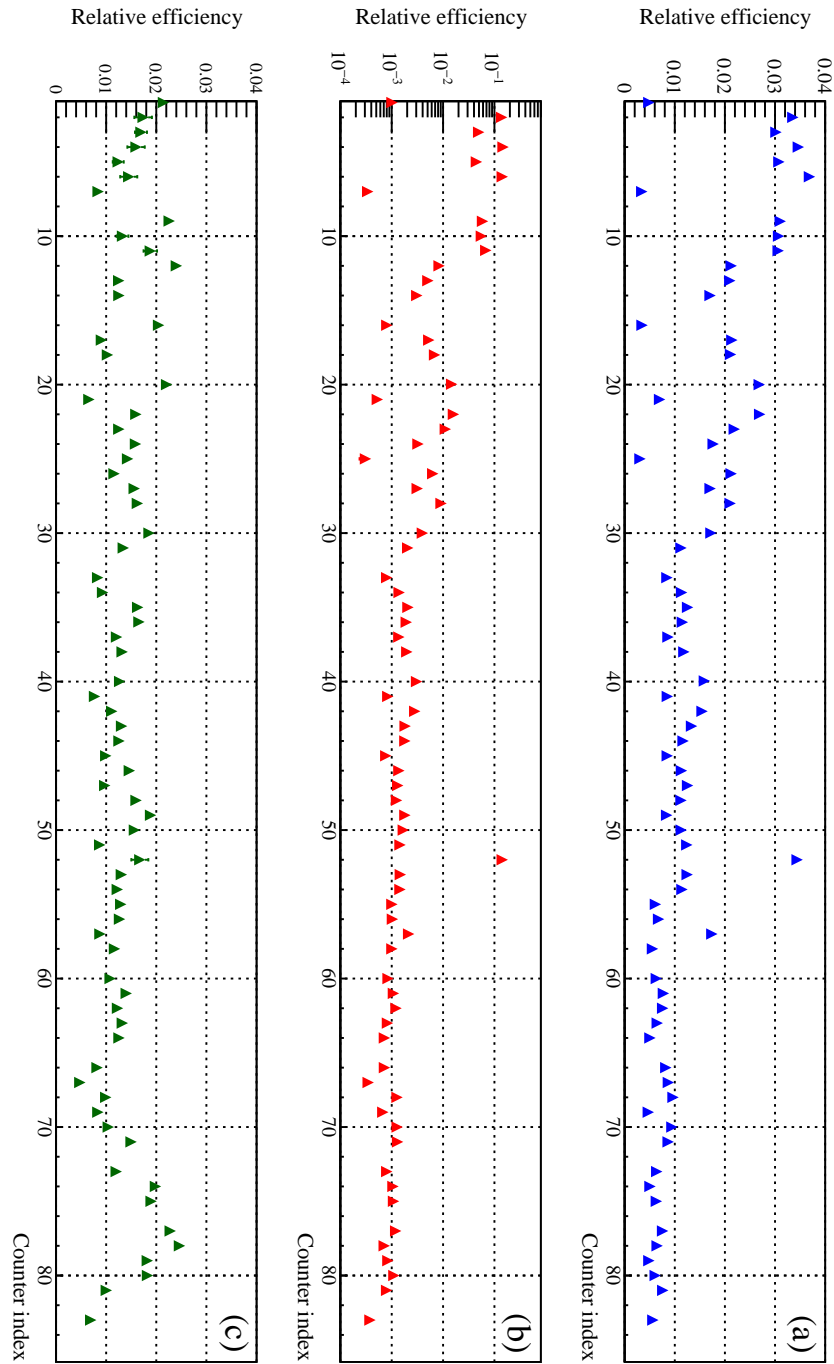


FIGURE 4.15 – Relative efficiency for each component in Equation 4.14 per counter for one run. Panels (a) and (b) give the relative efficiency of each individual counter with respect to the contributions following the  $^8\text{He}$  and  $^8\text{Li}$  lifetimes, respectively. Panel (c) gives the relative contribution of each individual counter for the constant background parameter.

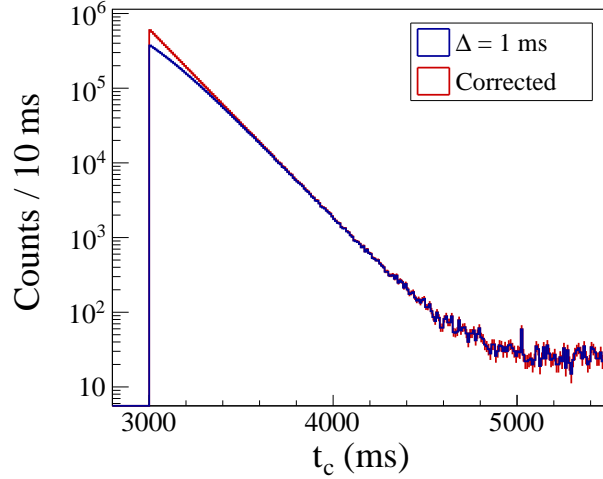


FIGURE 4.16 – Distribution of events with respect to their time  $t_c$  for all 4 runs with implantation cycles of 10 s. The blue histogram shows all recorded events that pass through a deadtime of  $\Delta = 1$  ms applied to each individual counter offline. A weight  $w_{i,j}$  defined in Equation 4.19 is then applied to all of these events resulting in the red histogram. Finally, the data in the second histogram are fitted to extract a half-life value.

### Fit results

The final corrected histograms are fitted for  $t_c \geq t_{\text{ON}}$  with a simple exponential decay model on top of a constant background in which the half-life  $t_{1/2} = \ln 2/\lambda$  is now a free parameter. Each fit is performed using the weighted log likelihood method in ROOT on corrected histograms with a bin width of 10 ms for all values of  $\Delta$ . The results of each fit with respect to the imposed deadtime and for both durations of the implantation cycles are shown in Figure 4.17. The results in this figure are obtained with fits performed on events between  $t_{\text{ON}} \leq t_c \leq t_{\text{ON}} + 2.2$  s. Not taking the remaining time where background detection dominates had no influence on the returned  $t_{1/2}$  values but considerably improved the goodness-of-fit indicators.

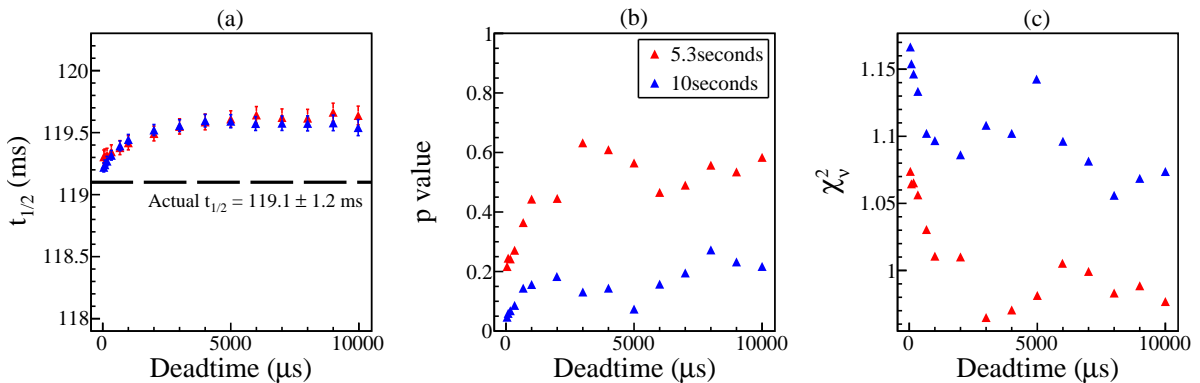


FIGURE 4.17 – Result of the fits with respect to the deadtime imposed offline and the duration of the implantation cycle. Panel (a) shows the half-life values returned by each fit. Panels (b) and (c) show the  $p$  values and  $\chi^2_\nu$  (reduced chi-square) which serve as goodness-of-fit indicators.

For corrections with deadtime  $\Delta \leq 1$  ms it can be seen that the returned half-lives have substantially dropped compared to the initial values. For 10 s cycles, the value went from 119.61 to 119.21 ms. For 5.3 s cycles, the value went from 119.49 to 119.30 ms. The half-lives then converge around  $t_{1/2} \approx 119.55$  ms as the deadtime increases. This points to a potential overcorrection of the data for small deadtimes that could increase the slope of the exponential curve too much and therefore lead to a smaller half-life. This could be due to the nominal value of 119.1 ms used to evaluate the real detection rate. Indeed, for small deadtimes, few events are actually discarded, and the correction weight applied to all remaining events could be too strong. Unfortunately, we did not have enough time to further investigate this problem.

Apart from this effect, the deadtime correction completely reconciles the half-lives obtained between the two implantation cycles while converging to values consistent with those obtained at the beginning of the analysis before the deadtime corrections. Furthermore, the  $p$  values and the  $\chi^2_\nu$  values are on average better for deadtimes  $\Delta > 1$  ms, indicating a better statistical agreement between the data and the model in that region.

#### 4.4.3 Summary and best $^8\text{He}$ half-life estimate

The very large number of neutron events recorded with TETRA during the few  $^8\text{He}$  runs in which the beam was implanted periodically coupled to a low background environment has shown to be a great opportunity to improve the value of  $t_{1/2}(^8\text{He})$ . Selecting the events with respect to their deposited energy within TETRA allowed us to obtain  $t_c$  distributions that only follow the  $^8\text{He}$  lifetime. Data were grouped into two sets according to the duration of the implantation cycle and then fitted to a simple exponential decay model on top of a constant background. This simple procedure returned  $t_{1/2}$  values that, although relatively close, were in medium disagreement considering the statistical uncertainties as shown in Figure 4.13 (b).

This discrepancy was investigated by studying how the DAQ deadtime of 20  $\mu\text{s}$  impacted our measurement. To do so, we used the method described in [112] adapted to the multidetector TETRA to evaluate the real detection rate at all times  $t_c \geq t_{\text{ON}}$  in each  $^3\text{He}$  counter and for each implantation cycle. Various deadtimes were then applied offline on each individual counters. Each event that passed through the offline deadtime was assigned a correction weight given in Equation 4.19. Although this procedure reconciled the two data groups, the returned  $t_{1/2}$  values show a small divergent behavior for small deadtime corrections.

Even though we were unable to fully conclude this work, we can still give our best estimate of the  $t_{1/2}(^8\text{He})$  value at this point of the study. To do so, the  $t_c$  histograms for both implantation cycles are summed together for each deadtime correction in histograms with a 10 ms bin width ranging from  $t_{\text{ON}} = 0$  to 5 seconds. The final data are fitted with the same model as before. As the background level is higher, we now fit the data between  $t_{\text{ON}} \leq t_c \leq 3$  s. The results are shown in Figure 4.18. To obtain an estimate of the  $^8\text{He}$  half-life, we used fit results with  $\Delta \geq 1$  ms only, where the  $p$  values are all greater than 0.25. Finally, the average half-life in this range is  $t_{1/2}(^8\text{He}) = 119.553 \pm 0.039$  ms, where the uncertainty is also an average of uncertainties from selected results.

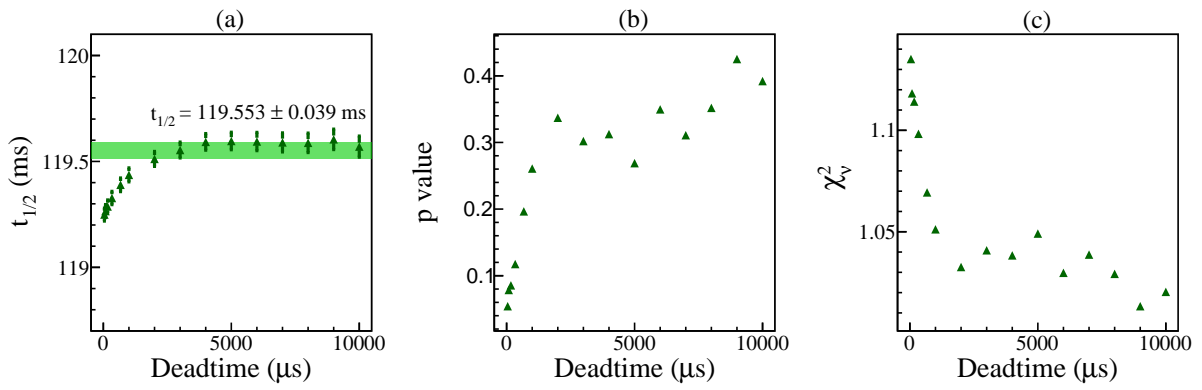


FIGURE 4.18 – Results of the final fits with respect to the deadtime imposed offline. Panel (a) shows the result of each fit and a band that corresponds to our best estimate. Panels (b) and (c) show the values of  $p$  and the reduced chi squares.

# Chapter 5

## ${}^6\text{He}$ analysis

In this chapter, we cover the different steps made to evaluate a stringent upper limit for the existence of a dark decay in  ${}^6\text{He}$ . In the following, we discuss the calculation of the average  ${}^6\text{He}$  beam intensity with the plastic scintillator and how we used the events recorded with the neutron detector TETRA.

### Contents

---

<b>5.1 Overview of the model</b> . . . . .	<b>76</b>
<b>5.2 <math>{}^6\text{He}</math> beam monitoring</b> . . . . .	<b>77</b>
5.2.1 $\gamma$ rays and bremsstrahlung detection with the HPGe . . . . .	77
5.2.2 Evaluation of $r_0$ from the plastic scintillator . . . . .	78
<b>5.3 TETRA analysis</b> . . . . .	<b>79</b>
5.3.1 Bremsstrahlung detection . . . . .	80
5.3.2 Anomalous counters with spurious events . . . . .	82
5.3.3 Searching for events above the background level . . . . .	84
<b>5.4 Evaluation of <math>\text{Br}_\chi</math></b> . . . . .	<b>88</b>
5.4.1 Fit procedure . . . . .	88
5.4.2 Results . . . . .	88
5.4.3 Stringent upper limit . . . . .	90

---

## 5.1 Overview of the model

The possibility of a neutron dark decay in  ${}^6\text{He}$  has been investigated using the neutron detector TETRA to detect the emission of a free neutron. Assuming that the neutron dark decay exists in  ${}^6\text{He}$ , free neutrons emitted at a rate proportional to the implanted and surviving  ${}^6\text{He}$  population in the catcher should be detected. During the experiment, the radioactive  ${}^6\text{He}$  beam was implanted inside the aluminum catcher for a duration of  $t_{\text{ON}} = 3$  s followed by 7 s without the beam to monitor the decay products. The change in the  ${}^6\text{He}$  population over time  $t_c$  within each cycle can be easily modeled by two parameters  $P_1(t_c)$  and  $P_2(t_c)$ . Here,  $P_1(t_c)$  and  $P_2(t_c)$  describe the number of  ${}^6\text{He}$  nuclei inside the catcher during the implantation time  $0 \leq t_c \leq t_{\text{ON}}$  and during the observation time  $t_{\text{ON}} \leq t_c \leq 10$  s, respectively. First, the expression of  $P_1(t_c)$  can be obtained from the following differential equation :

$$dP_1 = -\lambda P_1 dt + r_0 dt, \quad (5.1)$$

where  $\lambda = 1/\tau$  is the  ${}^6\text{He}$  decay rate and  $r_0$  is the beam implantation rate inside the catcher. We assume that the beam intensity is constant during the 3 seconds of implantation. Solving Eq. (5.1) gives :

$$P_1(t_c) = \frac{r_0}{\lambda}(1 - e^{-t_c/\tau}). \quad (5.2)$$

For  $t_c \geq t_{\text{ON}}$ , the expression of  $P_2(t_c)$  is directly given by the exponential decay law :

$$P_2(t_c) = P_2^{\text{on}} e^{-(t_c - t_{\text{ON}})/\tau}, \quad (5.3)$$

where  $P_2^{\text{on}}$  is the population in the catcher at  $t_c = t_{\text{ON}}$  and is given by  $P_1(t_{\text{ON}})$ . Therefore, we can write :

$$P_2(t_c) = \frac{r_0}{\lambda}(e^{t_{\text{ON}}/\tau} - 1)e^{-t_c/\tau}. \quad (5.4)$$

Subsequently, the equations representing the activity within the catcher  $A(t) = \lambda P(t)$  are readily derived :

$$A_1(t_c) = r_0(1 - e^{-t_c/\tau}), \quad (5.5)$$

$$A_2(t_c) = r_0(e^{t_{\text{ON}}/\tau} - 1)e^{-t_c/\tau}. \quad (5.6)$$

Thus, the instantaneous detection rates  $N_1(t_c)$  and  $N_2(t_c)$  in a detector with detection efficiency  $\varepsilon$  for decay products emitted from a specific decay channel  $i$  with a branching ratio  $\text{Br}_i$  are :

$$N_1(t_c) = \phi(1 - e^{-t_c/\tau}) + b, \quad (5.7)$$

$$N_2(t_c) = \phi(e^{t_{\text{ON}}/\tau} - 1)e^{-t_c/\tau} + b, \quad (5.8)$$

where  $b$  is an additional parameter representing a constant background and  $\phi = \varepsilon r_0 \text{Br}_i$ . Constraining the existence of a dark decay in  ${}^6\text{He}$  thereby corresponds to putting a stringent upper limit on its branching ratio  $\text{Br}_\chi$ . This requires knowledge of only three different parameters : the average  ${}^6\text{He}$  beam intensity inside the catcher ( $r_0$ ), the neutron detection efficiency of TETRA ( $\varepsilon_n$ ) and the neutron detection rate correlated to the  ${}^6\text{He}$  decay and measured with TETRA ( $\phi$ ). In the following work, the  ${}^6\text{He}$  lifetime has been fixed at

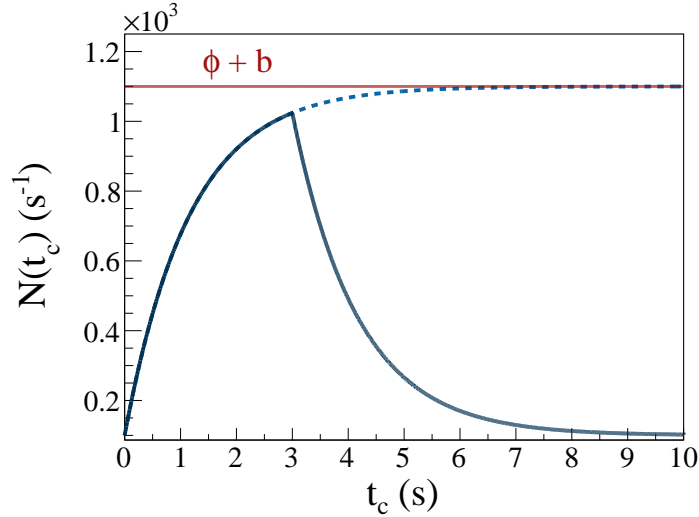


FIGURE 5.1 – Representation of the detection rate  $N(t_c)$  with respect to the time  $t_c$  within an implantation cycle. The parameters used in this figure are  $\phi = 1000 \text{ s}^{-1}$ ,  $b = 100 \text{ s}^{-1}$  and  $\tau = 1.164 \text{ s}$ . The solid blue line shows the expected behavior with 3 s of implantation and 7 s of observation. The dashed blue line represents the progression of  $N(t_c)$  if the beam is not stopped at  $t_{\text{ON}}$ . The solid red line indicates the maximum detection rate achieved for  $t_c \gtrsim 5\tau$ .

$\tau = 1.164 \text{ s}$  [112]. An example of an implantation cycle with  $\phi = 1000 \text{ s}^{-1}$  and  $b = 100 \text{ s}^{-1}$  is shown in Figure 5.1.

## 5.2 ${}^6\text{He}$ beam monitoring

The HPGe and plastic scintillator roles were to look for potential radioactive contaminants that could be brought into the catcher along with the  ${}^6\text{He}$  nuclei. Furthermore, the plastic scintillator was used to determine the average beam intensity parameter called  $r_0$ .

### 5.2.1 $\gamma$ rays and bremsstrahlung detection with the HPGe

The HPGe was used during the  ${}^6\text{He}$  runs mainly to look for possible unwanted radioactive nuclei that could be transported along with the  ${}^6\text{He}^+$  ions into the catcher. The energy spectra at both HPGe positions are shown in Figure 5.2. The overwhelming majority of events registered with the HPGe are not classical gamma from nuclear deexcitation, but rather bremsstrahlung photons correlated with the emission of  $\beta$  particles from the  ${}^6\text{He}$  decay and subsequently interacting with the surrounding matter. Only three different lines were observed standing out of the bremsstrahlung bulk at both HPGe positions : the 511 keV  $e^+e^-$  annihilation line, a 661.6 keV line emitted from a  ${}^{137}\text{Cs}$  control beacon, and a 1460.7 keV line emitted from  ${}^{214}\text{Bi}$  present in the concrete inside the room.

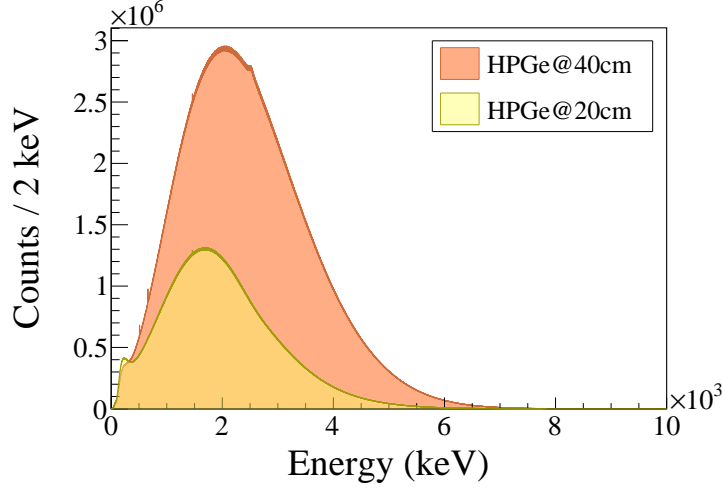


FIGURE 5.2 – Energy spectrum recorded with the HPGe at both positions. The vast majority of events are from bremsstrahlung radiation.

### 5.2.2 Evaluation of $r_0$ from the plastic scintillator

The average beam intensity parameter  $r_0$  required to assess an upper limit on  $\text{Br}_\chi$  can be evaluated thanks to the small solid angle plastic scintillator placed on top of the HPGe. The HPGe and plastic scintillator were positioned differently to cope with the  ${}^6\text{He}$  beam intensity estimated online by the silicon detector along the LIRAT line. A total of 37374 cycles are used in the following analysis. The first 19612 cycles were performed with the plastic scintillator at the closest position from the catcher ( $\approx 20\text{cm}$ ) with  $\varepsilon_{\beta,C} = (8.67 \pm 0.44) \times 10^{-4}$ . The remaining 17762 cycles were performed at the second and farthest position ( $\approx 40\text{cm}$ ) with  $\varepsilon_{\beta,F} = (1.57 \pm 0.09) \times 10^{-4}$ .

#### Average beam intensity at each position

All recorded events within the 37374 implantation cycles with the plastic scintillator are shown in Figure 5.3. Figure 5.3 (a) shows the energy spectra registered at both positions. Figure 5.3 (b) shows their associated time distributions within an implantation cycle with a binning of 10 ms. The two histograms in the latter figure are fitted using Equations 5.7 and 5.8. Although these histograms represent the total dose recorded at  $t_c$ , their corresponding instantaneous detection rates during a typical cycle can be assessed simply by dividing the content of a bin by the number of cycles and the width of the bin. It is necessary to consider these factors to properly evaluate  $\phi$  and calculate the associated mean beam intensity  $r_0$ .

Fitting the data in both histograms shown in Figure 5.3 (b) returned two different values that we call  $\tilde{\phi}_i$  which are connected to the desired  $\phi_i$  as follows :

$$\phi_i = \frac{c \tilde{\phi}_i}{b C_i}, \quad (5.9)$$

where  $c = 1000$  is the ( $\text{ms}^{-1} \rightarrow \text{s}^{-1}$ ) conversion factor,  $b = 10 \text{ ms}$  is the bin width used on both histograms and  $C_i$  is the number of cycles at the  $i = C, F$  plastic scintillator position.

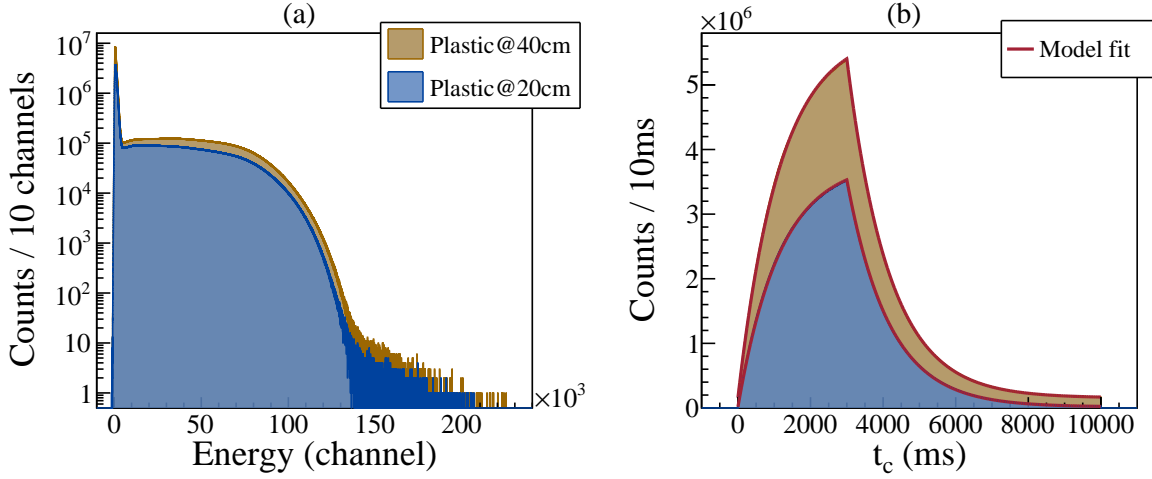


FIGURE 5.3 – (a) Plastic scintillator uncalibrated energy spectra. The blue (orange) histogram corresponds to the data recorded during the first 19612 (last 17762) cycles where the plastic was at  $\approx 20\text{cm}$  ( $\approx 40\text{cm}$ ) from the aluminum catcher. (b) Their corresponding histograms as a function of the time in the cycle  $t_c$ . Both data sets were fitted using the model described by Equations 5.7 and 5.8.

The values produced by the fit are  $\tilde{\phi}_C = 3.81 \times 10^6$  and  $\tilde{\phi}_F = 5.68 \times 10^6$ . The relative statistical uncertainties for both values are approximately  $10^{-4}$ . Using  $\text{Br}_\beta = 1$  and the appropriate detection efficiency  $\varepsilon_{\beta,i}$  we find the two following average  ${}^6\text{He}$  beam intensities  $r_{0,C} = (2.25 \pm 0.12) \times 10^7 \text{ s}^{-1}$  and  $r_{0,F} = (2.03 \pm 0.11) \times 10^8 \text{ s}^{-1}$  where the uncertainties contain both the statistical uncertainty returned by the fit and the uncertainty on the associated  $\varepsilon_{\beta,i}$  value.

### Average $r_0$ value during the experiment

To obtain an average beam intensity value on all cycles that we can use in the following TETRA analysis, we first evaluate  $H_i$ , the total number of implanted  ${}^6\text{He}$  at the  $i = C, F$  position using :

$$H_i = r_{0,i} C_i t_{\text{ON}}. \quad (5.10)$$

From this we obtain  $H_C = (1.32 \pm 0.07) \times 10^{12}$  and  $H_F = (1.08 \pm 0.06) \times 10^{13}$ . Therefore, the total number of implanted  ${}^6\text{He}$  in the aluminum catcher during the experiment is  $H_{\text{tot}} = (1.21 \pm 0.07) \times 10^{13}$ . Finally, using Equation 5.10, we determine the average beam intensity over the 37374 cycles, resulting in  $r_0 = (1.08 \pm 0.06) \times 10^8 \text{ s}^{-1}$ . All numbers discussed in this section are compiled in Table 5.1. Along with the evaluation of  $r_0$ , and as can be seen in Figure 5.3 (b), the plastic scintillator analysis has revealed no  $\beta$  emitters other than  ${}^6\text{He}$ .

## 5.3 TETRA analysis

As mentioned above, the recording of events using TETRA mainly originates from three distinct sources. The first corresponds to the detection of background events and arises at

$i$	$\varepsilon_{\beta,i} \times 10^4$	$C_i$	$\tilde{\phi}_i \times 10^{-6}$	$r_{0,i} (\text{s}^{-1})$	$H_i$
$C$	$8.67 \pm 0.44$	19612	3.81	$(2.25 \pm 0.12) \times 10^7$	$(1.32 \pm 0.07) \times 10^{12}$
$F$	$1.57 \pm 0.09$	17762	5.68	$(2.03 \pm 0.11) \times 10^8$	$(1.08 \pm 0.06) \times 10^{13}$
Total		37374		$(1.08 \pm 0.06) \times 10^8$	$(1.21 \pm 0.07) \times 10^{13}$

TABLE 5.1 – Summary of all numbers involved in the plastic scintillator analysis.

a constant rate. The second comes from the detection of bremsstrahlung photons related to  ${}^6\text{He}$   $\beta$  decays. Finally, the third corresponds to the detection of neutron events, which, in the case of a dark decay, should follow the  ${}^6\text{He}$  lifetime. Therefore, the purpose of the data analysis with TETRA is to recover a reliable  $\phi$  value as defined in Equations 5.7 and 5.8 that can be used to properly constrain  $\text{Br}_\chi$ . To do so, we must ensure that any deviation from a uniform background detection rate distribution in the final  $t_c$  histogram is not caused by any systematic effects. Identifying and removing these effects is the primary concern discussed in the following work. All events registered with TETRA with respect to their deposited energy inside the counters are shown in Figure 5.4.

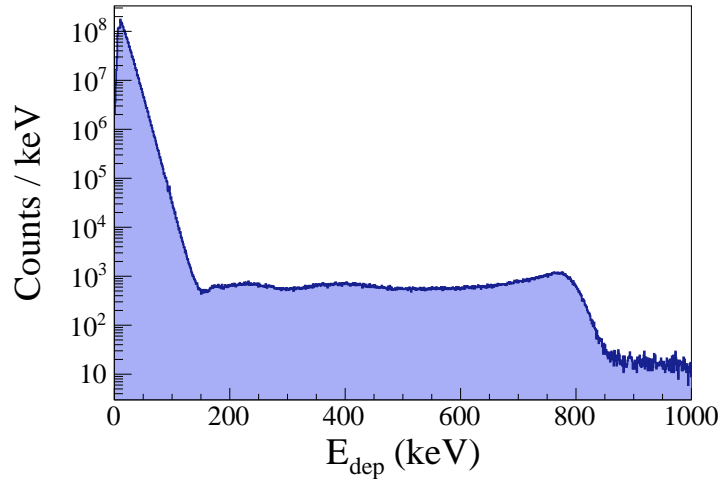


FIGURE 5.4 – Energy spectrum of TETRA with all events recorded throughout the 37374 implantation cycles.

### 5.3.1 Bremsstrahlung detection

#### Observation with TETRA

As with the HPGe, the bremsstrahlung associated with the  $\beta$  decay of  ${}^6\text{He}$  was also observed with TETRA. These photons were able to ionize the gas inside the counters with a deposited energy usually lower than  $\approx 150$  keV. Similarly to the HPGe, the vast majority of events observed with TETRA are bremsstrahlung photons. Figure 5.5 (a) shows these events in the energy spectrum of TETRA and Figure 5.5 (b) shows how they are distributed with respect to  $t_c$ . This bremsstrahlung detection is one of the main

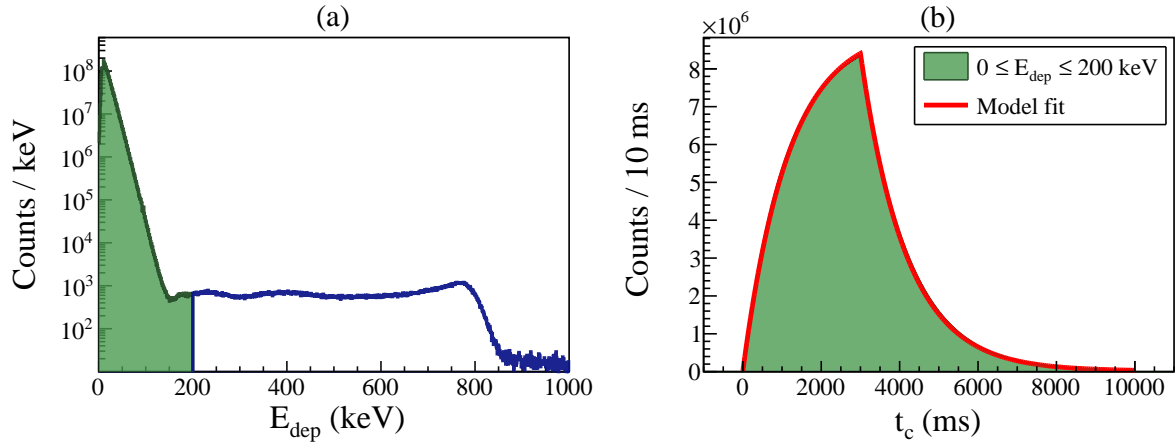


FIGURE 5.5 – (a) Energy spectrum of TETRA with a selection window in green for events in the  $0 \leq E_{dep} \leq 200$  keV range. (b) The associated histogram with respect to  $t_c$ . The data in the latter histogram is fitted using Equations 5.7 and 5.8 with a fixed  ${}^6\text{He}$  lifetime.

Lower limit (keV)	150	200	250	300	400	500	600	700
$\varepsilon_n$ (%)	46.89	45.15	42.07	39.11	32.88	26.08	20.08	13.18
$\Delta\varepsilon_n$ (%)	5.08	4.89	4.56	4.24	3.56	2.83	2.18	1.43

TABLE 5.2 – All lower limits used to select events within the neutron detection range in TETRA and their associated detection efficiency written in the form  $\varepsilon_n \pm \Delta\varepsilon_n$  (%).

problems we have encountered during the analysis. As can be seen in Figure 5.5 (b), it follows the  ${}^6\text{He}$  lifetime and can extend into the deposited energy range corresponding to neutron detection. Therefore, the bremsstrahlung detection mimics the dark decay we are trying to observe.

### Handling the bremsstrahlung

In order to deal with this contamination, we have simply made various cuts in the events that are within the range of neutron detection. Similarly to what is shown in Figure 5.5, events were selected with respect to various lower limits ranging from  $E_{dep} = 150$  keV to 700 keV and a common upper limit placed at 820 keV. These different selection windows were used to produce their corresponding  $t_c$  histograms in which the data was fitted using Equations 5.7 and 5.8. Note that these different data sets are not statistically independent as they all share the same upper limit at 820 keV. The detection efficiencies with respect to each lower limit are computed as described in Section 3.2.3. All lower limits starting at  $E_{dep} = 150$  keV and their corresponding detection efficiency are listed in Table 5.2.

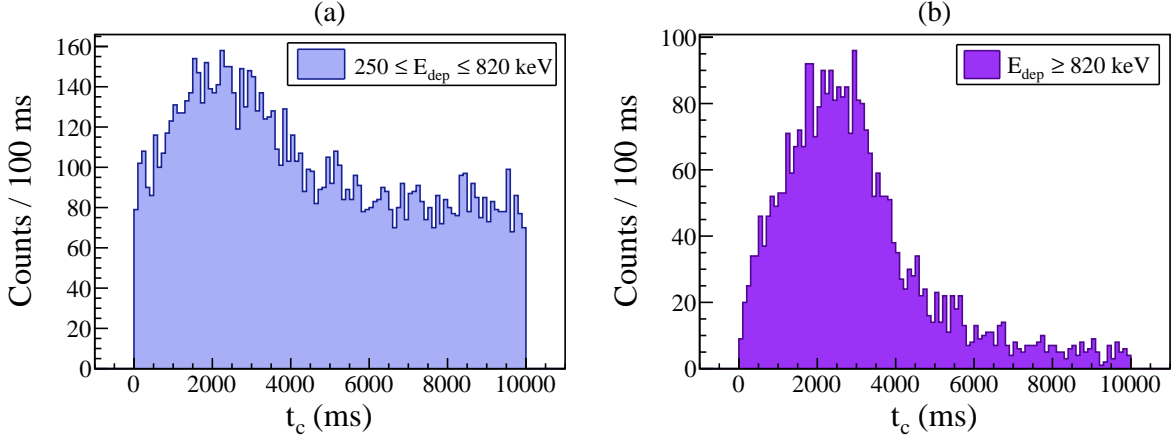


FIGURE 5.6 – (a) Distribution of events in the  $250 \leq E_{dep} \leq 820$  keV range with respect to  $t_c$ . (b) Distribution of events with  $E_{dep} \geq 820$  keV with respect to  $t_c$ . Both of these figures show the recorded events from counter number 82 only which is the most affected by these spurious events.

### 5.3.2 Anomalous counters with spurious events

#### Events following the beam implantation cycle

The first step in cleaning the data is to remove the counters that exhibited an anomalous response. Dead counters and counters with an inappropriate deposited energy spectrum were already excluded. Events recorded with TETRA during our experiment can be differentiated according to their deposited energy inside the counter. As discussed above, events with  $0 \leq E_{dep} \leq 200$  keV usually correspond to bremsstrahlung detection, while events with  $150 \leq E_{dep} \leq 820$  keV are mainly attributed to neutron detection. However, events with higher deposited energy up to the saturation level of the DAQ close to  $E_{dep} \approx 1$  MeV were also recorded. The origin of such events was already discussed in Section 3.2.2.

In addition, few counters have registered events showing a strong correlation with the beam implantation cycle in both the neutron detection range and above. Such events for the counter labeled with the number 82 are shown in Figure 5.6 in the  $250 \leq E_{dep} \leq 820$  keV and  $E_{dep} \geq 820$  keV ranges. The lower limit at 250 keV is chosen to minimize bremsstrahlung contamination. Fitting the data with Equations 5.7 and 5.8 without fixing any parameters returned lifetime values compatible with the  ${}^6\text{He}$  lifetime and, therefore, also simulate the dark decay. The reason why some counters were more affected than others, as discussed below, remains unclear.

#### Identification of the affected counters

Assuming a pure background detection only, histograms showing the distribution of events within an implantation cycle between 0 and 10 seconds, as in Figure 5.6, should have a mean value of  $\bar{t}_c = 5$  s. In such histograms with uniformly distributed background events, statistical fluctuations should be the only reason for possible mean values below and above 5 s. For each counter in TETRA, the following values  $(5 - \bar{t}_n)$  and  $(5 - \bar{t}_s)$  were calculated where  $\bar{t}_n$  and  $\bar{t}_s$  are the mean values of  $t_c$  in the  $250 \leq E_{dep} \leq 820$  keV and in the  $E_{dep} \geq 820$

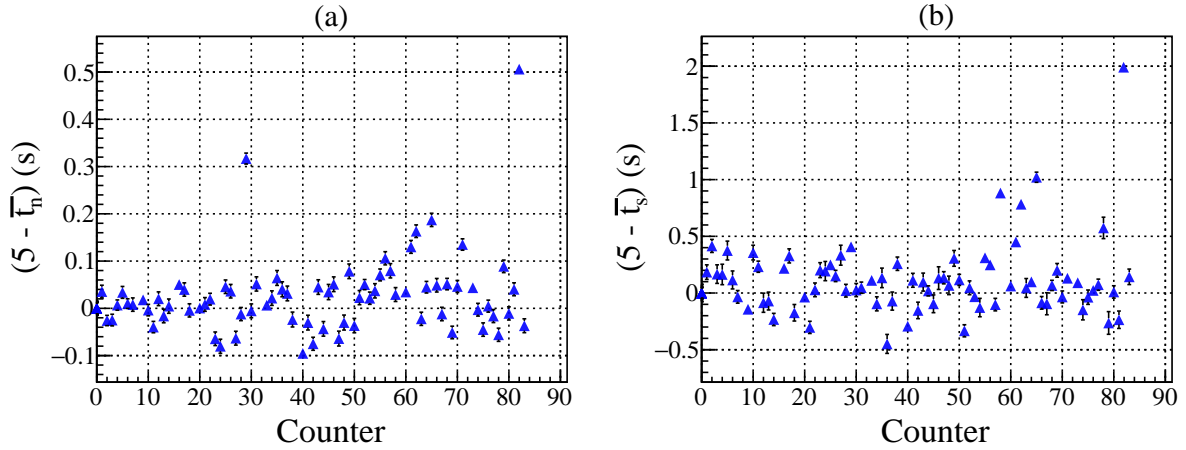


FIGURE 5.7 –  $(5 - \bar{t}_n)$  (a) and  $(5 - \bar{t}_s)$  (b) distributions with respect to the label of each counter from TETRA.

keV ranges, respectively. Each mean value is expressed in seconds. These values with respect to the number given as a label for each counter are shown in Figure 5.7. These two figures already show a few counters that display a behavior strongly correlated with the implantation cycle. However, they do not provide sufficient information separately to draw any conclusions. In fact, highlighting problematic counters with spurious events in both energy ranges requires building the  $(5 - \bar{t}_s)$  vs  $(5 - \bar{t}_n)$  distribution as shown in Figure 5.8.

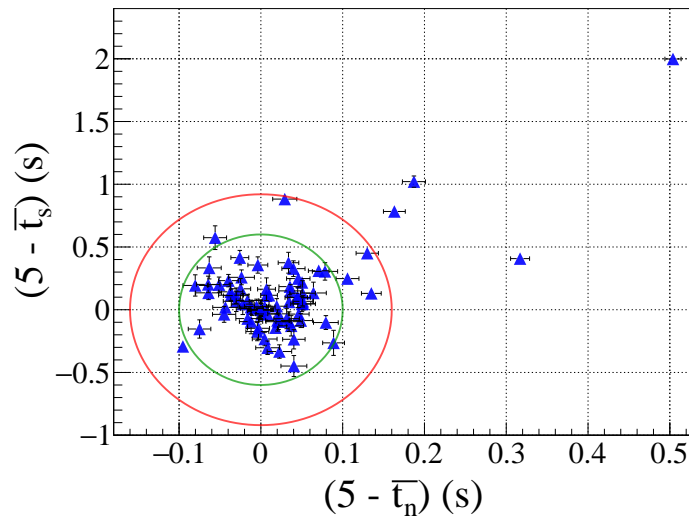


FIGURE 5.8 –  $(5 - \bar{t}_s)$  vs  $(5 - \bar{t}_n)$  distribution for all TETRA counters.

In this figure, the counters are distributed around the  $(0,0)$  point. This figure can be divided into 4 parts : one positively correlated with coordinates  $(\geq 0, \geq 0)$  and three anticorrelated with coordinates  $(\leq 0, \leq 0)$ ,  $(\leq 0, \geq 0)$  and  $(\geq 0, \leq 0)$ . If a counter is located in the correlated region, this means that events in its associated  $t_c$  histogram are usually placed with  $t_c \leq 5$  s in both energy ranges, as in Figures 5.6 (a) and (b). Obviously and as stated before, a counter could be located in this part only because of

statistical fluctuations. Therefore, a counter is deemed problematic if it is located in the correlated region with sufficiently large deviations in both directions compared to the rest of the counters. The green ellipse in Figure 5.8 contains all the counters with deviations that can be attributed to statistical fluctuations, since we can find counters in all four parts almost equally. The red ellipse contains counters with larger deviations which can be found either in one anticorrelated part or in the correlated region but with a deviation mainly along one axis. The four counters outside the red ellipse (such as the counter numbered 82 in Figure 5.6) are marked as problematic and were removed from the final analysis. In the end, 72 counters are used in the following work.

### 5.3.3 Searching for events above the background level

#### Time interval between events

An interesting feature in experimental physics is the description of time intervals between successive events recorded by a detector. Assuming a constant detection rate  $r$ , it can be shown that the time interval  $\Delta t$  between each event will be distributed as :

$$P(\Delta t) \sim e^{-r\Delta t}, \quad (5.11)$$

where  $P(\Delta t)$  is the probability to have a time interval of  $\Delta t$  between two adjacent events [100]. Figure 5.9 shows the  $t_c$  histogram of events recorded in the  $150 \leq E_{dep} \leq 820$  keV range. Comparing this  $t_c$  histogram with other  $t_c$  histograms shown above, as in Figure 5.3 (b), it is clear that the events registered with TETRA in this particular range are mainly due to background neutron detection. Therefore, we can build the  $P(\Delta t)$  distribution in the neutron detection range with TETRA to search for potential additional event sources.

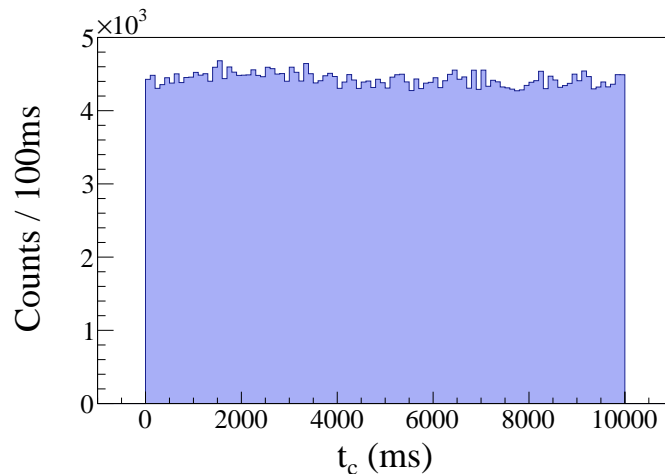


FIGURE 5.9 – Distribution of all events recorded with the 72 selected counters from TETRA in the  $150 \leq E_{dep} \leq 820$  keV range with respect to their time of arrival  $t_c$  in an implantation cycle.

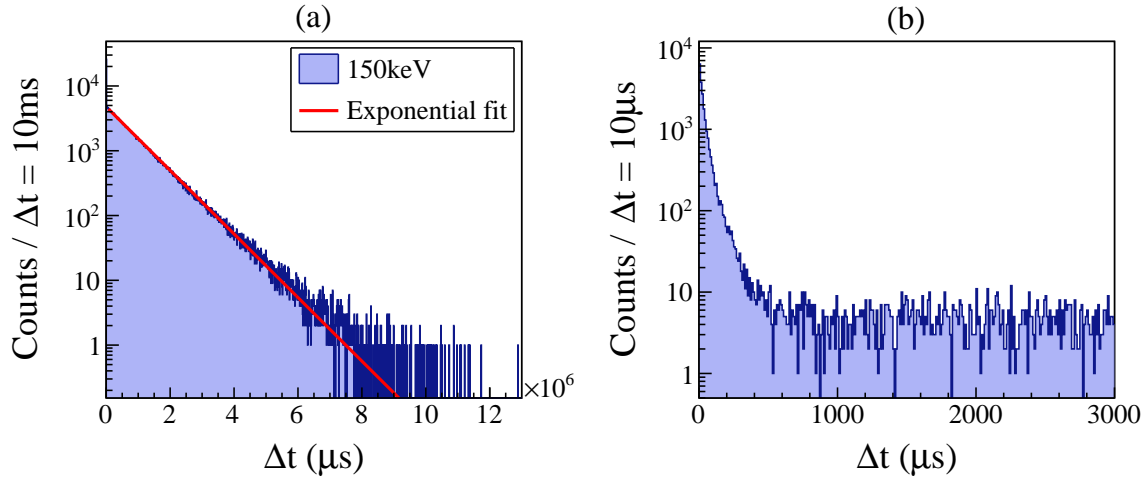


FIGURE 5.10 – Time interval between consecutive events for  $0 \leq \Delta t \leq 12$  seconds (a) and for  $0 \leq \Delta t \leq 3$  ms (b). The fit in (a) is made according to the model in Equation 5.11.

### Additional sources of events

In the following, we consider TETRA as a unique detector with a single event timeline, built by aggregating together all timelines from each selected counter. The  $P(\Delta t)$  histogram is then built by comparing the timestamp difference between each consecutive event. This histogram for events in the  $150 \leq E_{dep} \leq 820$  keV range is shown in Figure 5.10 (a) for  $\Delta t$  values between 0 and 12 seconds. The data in this histogram are fitted with an exponential model as described in Equation 5.11 and returned a detection rate around 1.14 Hz, which is compatible with the rate assessed in background runs. An additional distribution can also be observed for  $\Delta t$  values between 0 and 3 ms, as shown in Figure 5.10 (b). In this figure, the distribution for time intervals between 1 and 3 ms is mainly the continuity of the distribution shown in Figure 5.10 (a). However, another distribution clearly stands out for time intervals between 0 and 1 ms.

This additional distribution can also be observed when using different lower thresholds listed in Table 5.2. The  $t_c$  histograms for the lower limits placed at 400 and 700 keV are shown in Figure 5.11 (a) and their corresponding time interval distributions are shown in Figure 5.11 (b). In both figures, the histograms with the lower  $E_{dep}$  limit at 150 keV already discussed above are also shown as a point of comparison. Different reasons can explain the origin of the second distribution : (i) Artifact time intervals as a consequence of regrouping all selected counters within a single timeline. (ii) Background events of a different origin than ambient neutron detection, highly increasing the detection rate in short time windows. (iii) Events correlated with  ${}^6\text{He}$  decays, such as bremsstrahlungs or potential dark decays.

### Event flagging

The way in which these events can affect our final result by altering the  $t_c$  histograms can be investigated by flagging them. If an event with index  $j + 1$  is closer than a predefined

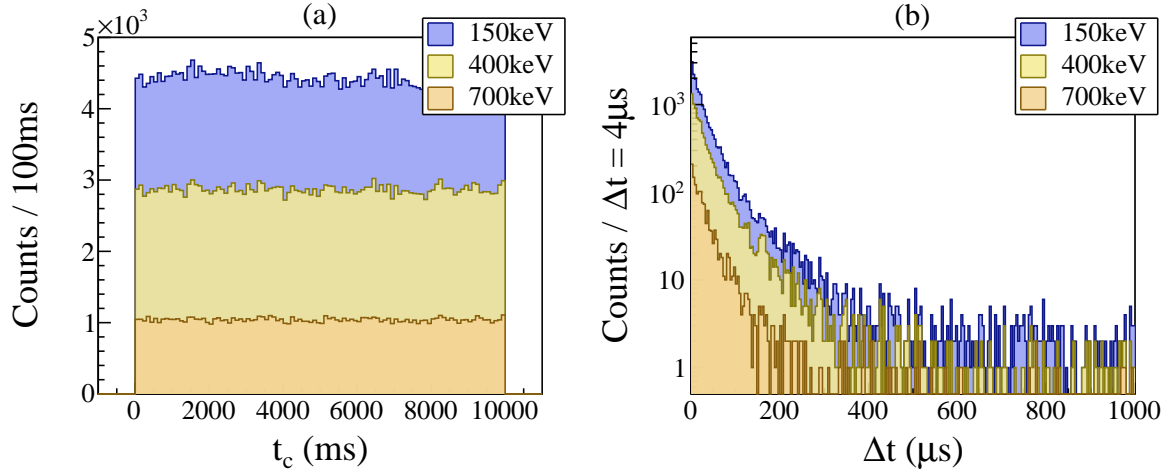


FIGURE 5.11 – (a)  $t_c$  histograms for three different  $E_{dep}$  lower limits. (b) Their associated  $\Delta t$  distribution in the  $0 \leq \Delta t \leq 1$  ms range.

time interval  $\Delta t$  to the event with index  $j$  in a specific  $E_{dep}$  range, then both events are flagged. Following this, if the  $j + 2$  event is also closer than  $\Delta t$  to the  $j + 1$  event, then the three events  $j, j + 1$  and  $j + 2$  are flagged. This continues until one event  $i$  is at a distance greater than  $\Delta t$  from the previous event  $i - 1$ . Finally, if an event  $k$  is separated by at least  $\Delta t$  from the  $k - 1$  and  $k + 1$  events, then  $k$  is not flagged. This procedure is summarized in Figure 5.12. In the following analysis, we will use two different  $\Delta t$  values to flag the events in all ranges of  $E_{dep}$  listed in Table 5.2 :  $\Delta t_1 = 300\mu\text{s}$  and  $\Delta t_2 = 1\text{ms}$ . These time intervals are defined this way, because both values largely cover the additional event source shown in Figure 5.11 (b). Once the events in question are flagged, they can be removed from the original data sets, as shown in Figure 5.13.

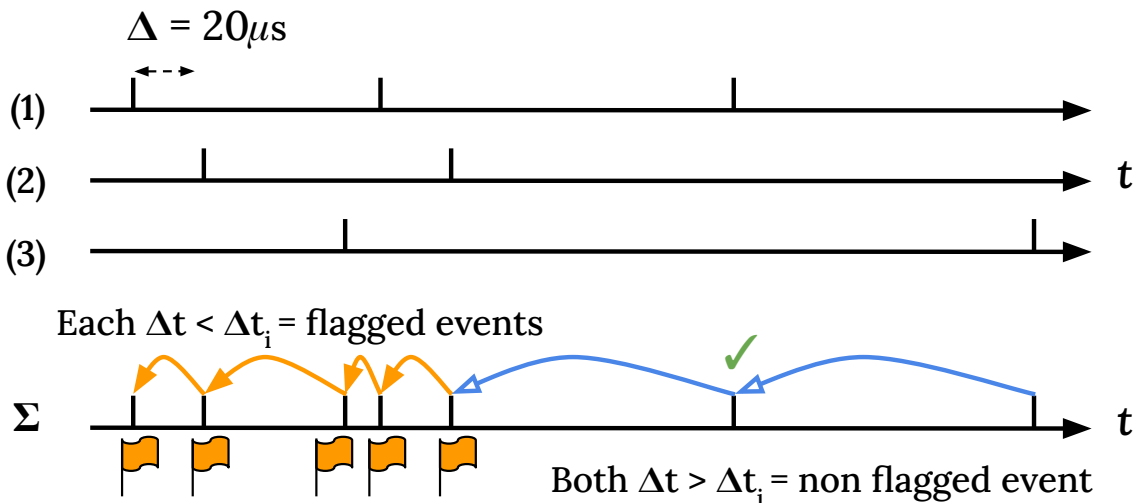


FIGURE 5.12 – Example showing the event line of three different counters from TETRA with their deadtime  $\Delta = 20\mu\text{s}$  and their sum  $\Sigma$ . The events that are closer than  $\Delta t_i = 0.3$  or  $1$  ms from each other are marked with a flag.

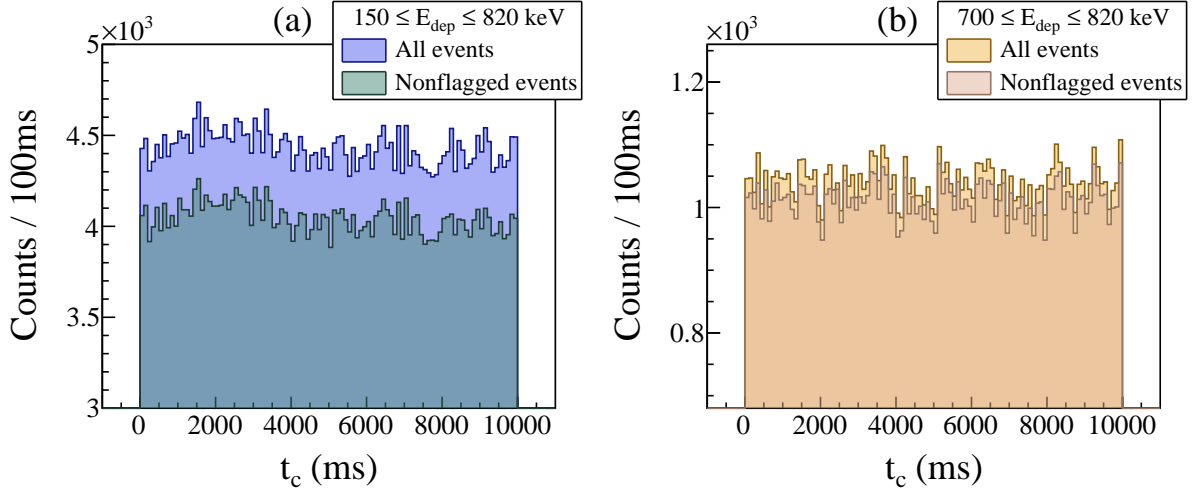


FIGURE 5.13 –  $t_c$  histograms with all events and with the flagged events removed. (a) shows the distributions for events with  $E_{dep} \geq 150$  keV and (b) for events with  $E_{dep} \geq 700$  keV. In both figures, the time interval used to flag the events is  $\Delta t_1 = 300\mu\text{s}$ .

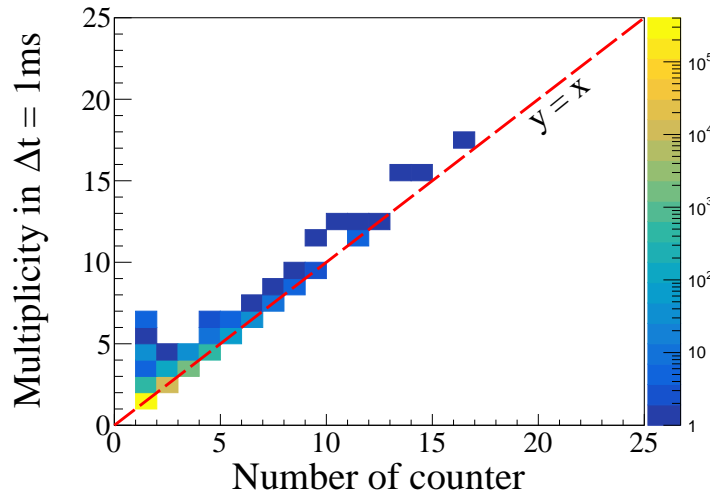


FIGURE 5.14 – Multiplicity of events within  $\Delta t_2 = 1$  ms with respect to the number of hit counters. The data shown here are for events with  $150 \leq E_{dep} \leq 820$  keV.

In addition, it is also possible to determine how many counters have been activated by these events, as shown in Figure 5.14. This figure shows the number of events with  $150 \leq E_{dep} \leq 820$  keV and  $\Delta t_2 = 1$  ms with respect to the number of counters they fired. Most flagged events are located along the  $y = x$  line in the figure, which means that each flagged event fired a different counter. If the multiplicity is strictly superior to the number of counters, it means that at least one counter was fired twice or more in the total time window in which the events were flagged. Groups with high multiplicity can be linked to spallation reaction from cosmic origins hitting multiple counters at the same time. The flagged events usually represent less than 10% of the total statistics. There are little to no differences between the numbers of events flagged with  $\Delta t_1 = 300\mu\text{s}$  and  $\Delta t_2 = 1$  ms.

## 5.4 Evaluation of $\text{Br}_\chi$

### 5.4.1 Fit procedure

All of the above discussions have highlighted two main sources of events that can alter our measurement of  $\text{Br}_\chi$  for the  ${}^6\text{He}$  dark decay : (i) the bremsstrahlung contamination and (ii) additional events sources that are difficult to clearly identify (cosmic spallation, radioactivity from material composing the counters, etc.). Indeed, (i) and (ii) can both potentially mimic the dark decay and their influence on our data must be thoroughly evaluated. In order to achieve a reliable branching ratio upper limit for the proposed  ${}^6\text{He}$  dark decay, multiple sets of data were produced. Initially, eight sets with different lower thresholds  $E_{dep}$  were made as listed in Table 5.2. We remind the reader that these groups of data are not statistically independent as they all share a common upper limit at  $E_{dep} = 820$  keV. For each of these sets, two additional subsets were generated in which all TETRA triggers within  $\Delta t_1 = 300\mu\text{s}$  or  $\Delta t_2 = 1\text{ms}$  were removed. Therefore, a total of 24 datasets were produced.

All of these different data sets were used to produce their corresponding  $t_c$  histograms. Then, all of these histograms were fitted with the model described by Equations 5.7 and 5.8. Moreover, to check any potential binning dependence on the final result, fits were performed on each group with bin widths ranging from 0.5 to 500 ms. All fits were performed using the log likelihood method provided by ROOT. As discussed in Section 5.2.2, fitting the data first returns the parameter  $\tilde{\phi}$ . The final variable  $\phi$  is achieved through Equation 5.9 using  $c = 1000$  which is the ( $\text{ms}^{-1} \rightarrow \text{s}^{-1}$ ) conversion factor,  $b$  is the bin width and  $C_{tot} = 37374$  is the total number of implantation cycles. Contrary to the  ${}^6\text{He}$  lifetime that is fixed, the remaining  $\phi$  and  $b$  parameters from Equations 5.7 and 5.8 are left completely free and no limits were placed on them to restrict the fitting procedure.

### 5.4.2 Results

All the  $\phi$  values obtained from the multiple fits are compiled in Figure 5.15. This figure is divided into three panels labeled (a), (b) and (c). First, the values of  $\phi$  in units of ( $\text{s}^{-1}$ ) with respect to the bin width in (ms) units are shown in each panel. Secondly, all data groups with respect to the lower threshold in deposited energy can be found in each panel. An additional group with a lower limit of  $E_{dep} = 100$  keV is also shown in each panel to highlight the effect of bremsstrahlung detection on the  $\phi$  values, but will not be used in the remaining work. Finally, panel (a) shows the results for fits performed on all events, while panels (b) and (c) show the results for fits performed on data groups where TETRA triggers within  $\Delta t_1 = 300\mu\text{s}$  and  $\Delta t_2 = 1\text{ms}$ , respectively, were rejected in each  $E_{dep}$  range.

The uncertainties shown in Figure 5.15 are only statistical and are returned by the fit. Relatively speaking and for data groups with lower limits higher than 200 keV, these statistical uncertainties are all at the 100% level or higher. There is no noticeable binning effect on the computed values of  $\phi$  in the vast majority of data groups. Some effects can be

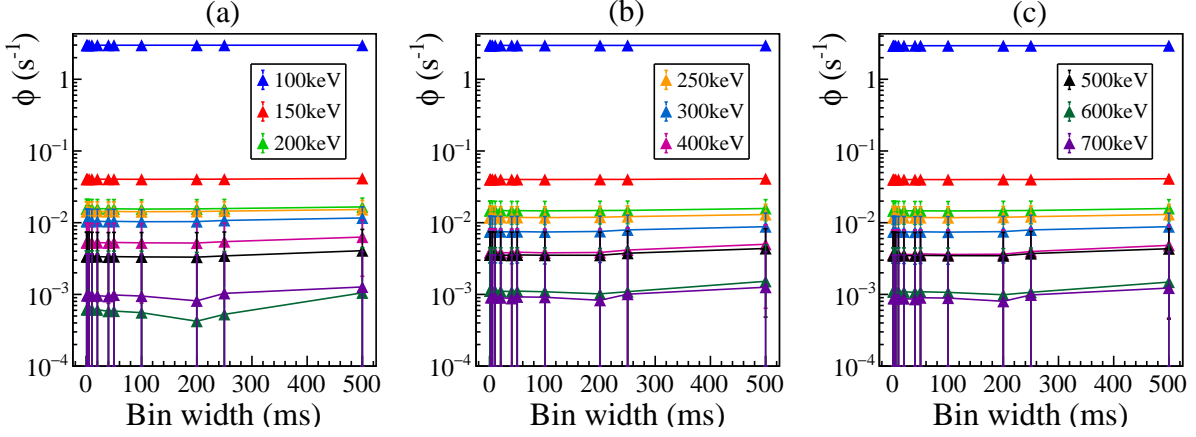


FIGURE 5.15 – All  $\phi$  values achieved from the multiple fits with respect to the binning of the concerned  $t_c$  histogram and the lower limit in  $E_{dep}$ . Fits performed using all TETRA events are shown in (a). Fits performed on data groups where events recorded within  $\Delta t_1 = 300\mu\text{s}$  and  $\Delta t_2 = 1\text{ms}$  were removed are shown in (b) and (c) respectively.

observed for groups with lower limits at 600 and 700 keV in panel (a), but the variations are well within error bars. The removal of TETRA triggers within  $\Delta t_{1,2}$  had little to no effect on the  $\phi$  values for groups with  $E_{dep} \leq 200$  keV. Some variations within the error bars can be seen for the  $\phi$  values of the data groups with  $E_{dep} \geq 250$  keV. This comes along with an overall great improvement in the  $p$ -values returned for each fit, indicating that removing the additional event source resulted in a better statistical agreement between the data and the model. For that reason, the next discussions will be based on  $\phi$  values returned for data groups where all TETRA triggers within  $\Delta t_1$  were rejected and for bin widths of 100 ms. Such  $\phi$  values are shown in Figure 5.16 (a) and the  $p$  values of each fit, all well above 0.05, are shown in Figure 5.16 (c).

The different  $\phi$  values shown in Figure 5.16 (a) cannot be directly compared together as their determination depends on the size of each data group. To solve this, we need

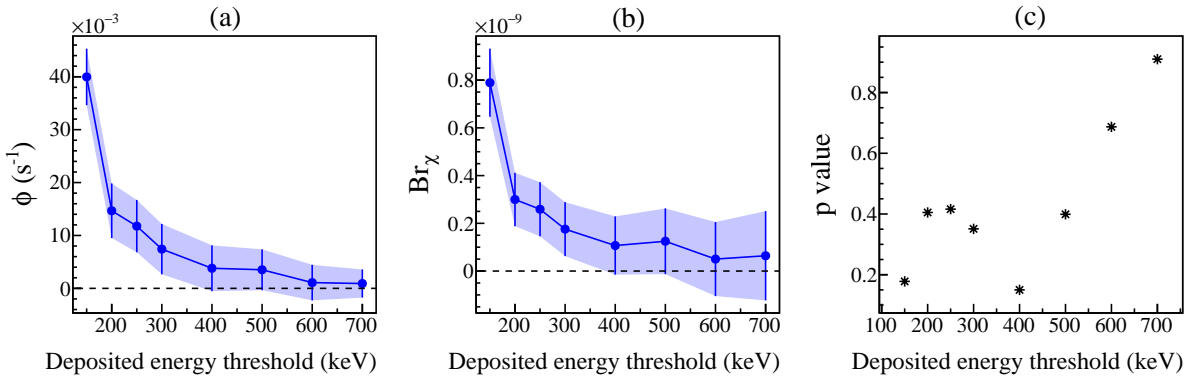


FIGURE 5.16 – (a)  $\phi$  values with respect to the lower  $E_{dep}$  threshold for fits performed with Equations 5.7 and 5.8 on data groups where events within  $\Delta t_1 = 300\mu\text{s}$  were removed. (b) Resulting branching ratio after scaling by the detection efficiency and the  ${}^6\text{He}$  beam intensity. (c) Corresponding  $p$  values for each fit. The dashed line in (a) and (b) is set at zero.

to calculate their corresponding dark branching ratios using  $\phi = \varepsilon_n r_0 \text{Br}_\chi$ . These  $\text{Br}_\chi$  values are shown in Figure 5.16 (b). The error bars shown in this figure correspond to the statistical uncertainties on each value of  $\phi$  returned by the fit and propagated along with the uncertainties on their associated  $\varepsilon_n$  and on  $r_0$ . The data group with the most statistics (lower threshold at  $E_{dep} = 150$  keV) clearly exhibits signs of bremsstrahlung contamination that slowly vanishes as the threshold increases. All the branching ratio values for  $E_{dep} \geq 200$  keV are generally in good agreement with each other with respect to their uncertainty.

### 5.4.3 Stringent upper limit

To place a strict upper limit on the branching ratio for the dark decay in  ${}^6\text{He}$ , each value shown in Figure 5.16 (b) is associated with a normal distribution with the following parameters :

$$(\mu, \sigma) = (\text{Br}_{\chi,i}, u(\text{Br}_{\chi,i})), \quad (5.12)$$

where  $\text{Br}_{\chi,i}$  is the branching ratio value for the  $i$ -th threshold associated with the uncertainty  $u(\text{Br}_{\chi,i})$ . Apart from the value at  $E_{dep} = 150$  keV, all the values in Figure 5.16 (b) are compatible with zero, with a tension lower than  $3\sigma$ . In the following, part of each distribution that goes to  $\text{Br}_\chi < 0$  is ignored in order to renormalize each surface with branching ratio values that are meaningful and physical. For each distribution, we compute the branching ratio value where 95% of the distribution surface is covered. This procedure for events with  $300 \leq E_{dep} \leq 820$  keV is shown in Figure 5.17.

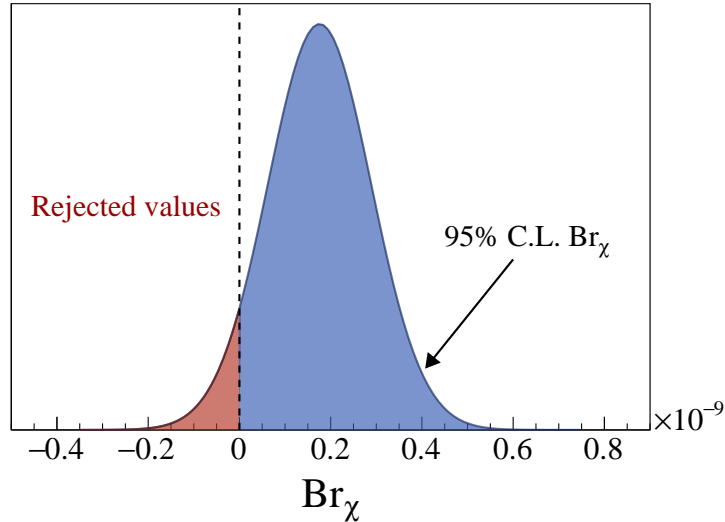


FIGURE 5.17 – Representation of the procedure followed to achieve the 95% C.L. dark branching ratio for the data group with  $E_{dep} \geq 300$  keV.

The result of this work is shown in Figure 5.18. As discussed above, the first point at  $E_{dep} = 150$  keV distinctly shows that the data group is tainted by bremsstrahlung events that replicate the dark decay. Finally, considering thresholds with  $E_{dep} \geq 300$  keV where the bremsstrahlung contamination seems to have little to no effects, we can place

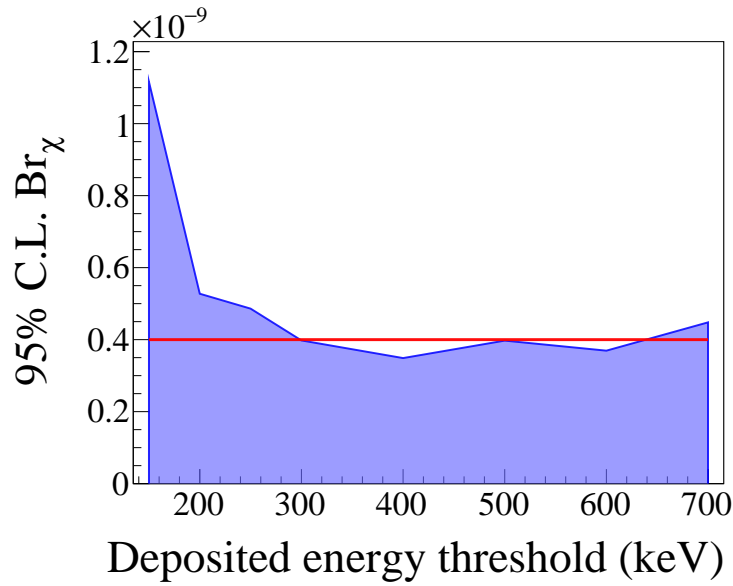


FIGURE 5.18 – Branching ratio values pushed at a 95% confidence level for each  $E_{dep}$  range. The red line indicates the conservative upper limit retained for the dark decay in  ${}^6\text{He}$  at  $4.0 \times 10^{-10}$ .

a conservative upper limit :

$$\text{Br}_\chi \leq 4.0 \times 10^{-10}, \quad (5.13)$$

for the  ${}^6\text{He}$  dark decay with a 95% confidence level. This limit is represented by the red line in Figure 5.18. Therefore, the maximum branching ratio we obtain is almost five orders of magnitude lower than the upper limit at  $1.2 \times 10^{-5}$  computed by Pfützner and Riisager in [79] to explain the neutron lifetime anomaly only through dark decays.

# Chapter 6

## Mass mixing constraint

The maximum branching ratio for the dark decay in  ${}^6\text{He}$  has been determined to be  $\text{Br}_\chi \leq 4.0 \times 10^{-10}$ , which serves to constrain the dark decay model. This chapter outlines the fundamentals of calculating any decay rate and how this can be used to explore and further constrain the parameter space for the neutron dark decay using our  ${}^6\text{He}$  result. Finally, this chapter ends with an explanation on how to probe the entire range of  $m_\chi$  using  ${}^{17}\text{C}$ . All expressions written in this chapter are in natural units, where  $[c] = [\hbar] = 1$ .

### Contents

---

<b>6.1 Overview</b>	<b>93</b>
<b>6.2 Decay rate calculations</b>	<b>93</b>
6.2.1 General formula	93
6.2.2 Decay amplitude in ${}^6\text{He}$	94
6.2.3 $\chi$ parameter space	95
6.2.4 $\phi$ parameter space	98
<b>6.3 Dark decay in <math>{}^{17}\text{C}</math></b>	<b>99</b>
6.3.1 Monte Carlo simulations of the ${}^{17}\text{C}$ decay	99
6.3.2 Result of the simulations	100
<b>6.4 Conclusion and perspective</b>	<b>102</b>

---

## 6.1 Overview

Two essential quantities in physics are the cross sections and the decay rates of any given process. These quantities can be measured experimentally and can also be calculated theoretically, providing a direct method of testing our understanding of nature. The main idea of this thesis work was to give an upper limit branching ratio for a neutron dark decay in  ${}^6\text{He}$ . A branching ratio is intrinsically related to the total decay rate  $\Gamma_{\text{tot}}$  of any unstable particle that appears in the well-known radioactive law written as :

$$N(t) = N_0 e^{-\Gamma t} = N_0 e^{-t/\tau}. \quad (6.1)$$

In this last equation,  $N_0$  is the initial number of particles at  $t = 0$  and  $\tau = 1/\Gamma_{\text{tot}}$  is known as the lifetime of the unstable particle. The total decay rate of this particle can be expressed as the aggregate of all partial decay rates  $\Gamma_i$  related to each individual decay process  $i$  like :

$$\Gamma_{\text{tot}} = \sum_i \Gamma_i. \quad (6.2)$$

Now, a partial decay rate can simply be written as :

$$\Gamma_i = \text{Br}_i \Gamma_{\text{tot}}, \quad (6.3)$$

where  $\text{Br}_i$  is the branching ratio of the  $i$ -th decay process. Therefore, we can write Equation 6.2 like :

$$\Gamma_{\text{tot}} = \sum_i \text{Br}_i \Gamma_{\text{tot}}. \quad (6.4)$$

In the case of  ${}^6\text{He}$ , its half-life has recently been accurately measured with  $t_{1/2} = \ln 2/\Gamma_{\text{tot}} = 807.25 \pm 0.16 \pm 0.11$  ms [112]. For the alleged dark decay in  ${}^6\text{He}$ , we have measured a branching ratio upper limit at  $\text{Br}_\chi \leq 4.0 \times 10^{-10}$  with a 95% confidence level. The theoretical expression for  $\Gamma_\chi$ , the partial decay rate for the dark decay in  ${}^6\text{He}$ , is the missing link needed to set further constraints on the model. Once an appropriate formulation of  $\Gamma_\chi$  is established, the known values of  $t_{1/2}$  and  $\text{Br}_\chi$  can be used to explore the parameter space  $(m_\chi, \frac{\varepsilon}{m_n - m_\chi})$  associated with the dark decay model (see Section 2.2) through :

$$\Gamma_\chi \left( m_\chi, \frac{\varepsilon}{m_n - m_\chi} \right) = \frac{\ln 2}{t_{1/2}} \text{Br}_\chi. \quad (6.5)$$

## 6.2 Decay rate calculations

### 6.2.1 General formula

The following equations are written in the same form as presented by the PDG in the Kinematics section of their latest review [113]. The differential expression of the partial decay rate for a particle with mass  $M$  in its rest frame in the initial state, decaying into

$n$  particles in the final state can be written like :

$$d\Gamma = \frac{(2\pi)^4}{2M} |\mathcal{M}|^2 d\Phi_n, \quad (6.6)$$

where  $\mathcal{M}$  is known as the Lorentz-invariant matrix element or the decay amplitude and  $d\Phi_n$  corresponds to the  $n$ -body phase space element. As with the decay amplitude, the phase space factor is also taken in its Lorentz-invariant form, meaning that it is relativistically invariant under any change of reference frame. It is sometimes written as  $d\text{LIPS}$  which stands for Lorentz-invariant phase space. It can be expressed as :

$$d\Phi_n = \delta^4(P - \sum_{i=1}^n p_i) \prod_{i=1}^n \frac{d^3\vec{p}_i}{(2\pi)^3 2E_i}, \quad (6.7)$$

where  $p_i$  and  $E_i$  are the 4-momentum and the energy of the  $i$ -th particle in the final state and  $P$  is the 4-momentum of the decaying particle. The delta function  $\delta^4$  ensures that the total energy and momentum are conserved in the process. The "4" simply means that it acts on all four components of the total 4-vector ( $P - \sum_{i=1}^n p_i$ ).

The phase space element is concerned with the kinematics of the decay process. It describes how the available energy is shared between all particles in the final state. The decay amplitude, on the other hand, describes the physics behind the decay. It can be expressed in a simple but effective way, or it can be expressed in a harder manner by laying out the fundamental picture behind the process. Like  $\beta$  decay was first described as a contact interaction and later understood as the interaction of a quark current and a leptonic current through the mediation of a  $W$  boson.

For a 3-body decay, the differential decay rate after integration of  $d\Phi_3$  can be expressed as :

$$d\Gamma = \frac{1}{(2\pi)^5} \frac{1}{16M} |\mathcal{M}|^2 dE_1 dE_3 d\alpha d(\cos\beta) d\gamma, \quad (6.8)$$

where  $\alpha$ ,  $\beta$  and  $\gamma$  are three Euler angles giving the orientation of the emitted particles in the final state with respect to the decaying particle in the initial state. To perform the remaining integration and obtain a theoretical expression for the dark decay rate in  ${}^6\text{He}$ , it is necessary to evaluate the form of the matrix element  $\mathcal{M}$ .

### 6.2.2 Decay amplitude in ${}^6\text{He}$

The  ${}^6\text{He}$  nucleus is characterized as a Borromean nucleus, which means that all of its two-body subsystems are unbound. Many theoretical attempts have successfully described  ${}^6\text{He}$  as the following 3-body system  $\alpha + n + n$  with well-defined  $\alpha n$  and  $nn$  interactions [114]. The core is usually considered an inert  ${}^4\text{He}$  nucleus with significant  $S_{n,p}({}^4\text{He}) \approx 20$  MeV values. The two valence neutrons, on the other hand, are weakly bound to the  $\alpha$  core with  $S_{2n}({}^6\text{He}) = 0.975$  MeV and are known to exist in both dineutron and cigar-like configurations [115, 116]. For that reason, the dark decay in this nucleus can be largely considered to happen only in one of the halo neutrons, leaving the  $\alpha$  core and the other neutron as simple spectators.

In the simplest assumption, the interaction in  ${}^6\text{He}$  is due to the mass mixing of a halo neutron with a dark fermion  $\chi$ . The matrix element to the lowest order simply is :

$$\mathcal{M} = \frac{\varepsilon}{m_n - m_\chi} \langle {}^4\text{He}, 2n | {}^6\text{He} \rangle, \quad (6.9)$$

where  $\langle {}^4\text{He}, 2n | {}^6\text{He} \rangle$  corresponds to the overlap between initial and final state wave functions, probing the degree to which one of the halo neutrons can be considered free. We assume here that the emission angle and energy of the outgoing particles do not influence the expression of  $\mathcal{M}$ . Moreover, here  $\mathcal{M}$  is dimensionless, as expected for a 3-body decay.

The wave function overlap  $\langle {}^4\text{He}, 2n | {}^6\text{He} \rangle$ , also called the spectroscopic factor  $S$ , has never been evaluated for halo neutrons in the  ${}^6\text{He}$  nucleus. However, it has been experimentally measured in nuclei such as  ${}^{11}\text{Be}$  and  ${}^{15}\text{C}$ , both of which are nuclei with a single halo neutron. In [117], spectroscopic factors for  ${}^{15}\text{C}$  in both its ground state and some of its excited states were obtained by measuring the angular distribution of cross sections for the  ${}^{14}\text{C}(d, p) {}^{15}\text{C}$  reaction. A mean value of 0.75 was obtained. In [118], it was determined that the ground state of  ${}^{11}\text{Be}$  could be described by a  ${}^{10}\text{Be}$  core with a valence neutron exhibiting predominantly single-particle behavior with a spectroscopic factor of 0.85 for this particular component. These two factors were also used in [119], which investigated the possibility of neutron dark decay in these nuclei. Therefore, we will use two different values for the  ${}^6\text{He}$  case : (i)  $S = 1$ , which is the limit case where the halo neutron is completely free and (ii)  $S = 0.5$ , which serves as a more conservative estimate.

### 6.2.3 $\chi$ parameter space

#### Constraint from the ${}^6\text{He}$ result

Now that we have a formulation of  $\mathcal{M}$  for the dark decay in  ${}^6\text{He}$ , we can inject it into Equation 6.8 to achieve an expression of  $\Gamma_\chi$ . Performing the remaining integration on the various emission angles results in :

$$d\Gamma_\chi = \frac{1}{(2\pi)^3} \frac{1}{8M} |\overline{\mathcal{M}}|^2 dE_1 dE_3, \quad (6.10)$$

Using  $M = m_\alpha + 2m_n - S_{2n}$  as the  ${}^6\text{He}$  mass we can identify  $dE_{1,3}$  as the energy of any of the three outgoing particles, since all combinations will lead to the same result. Therefore, computing the final integration leads to :

$$\Gamma_\chi = \frac{1}{(2\pi)^3} \frac{S^2}{8(m_\alpha + 2m_n - S_{2n})} \left( \frac{\varepsilon}{m_n - m_\chi} \right)^2 (m_n - S_{2n} - m_\chi)^2, \quad (6.11)$$

where  $S = 0.5, 1$  is the spectroscopic factor discussed above. The decay rate shown here is expressed in MeV. In order to remain consistent in terms of unit, the value  ${}^6\text{He}$  dark decay rate used in the following work is :

$$\Gamma_\chi = \frac{4.0 \times 10^{-10}}{1.164} 6.582 \times 10^{-22}, \quad (6.12)$$

where  $6.582 \times 10^{-22}$  is the ( $s^{-1} \rightarrow \text{MeV}$ ) conversion factor,  $4.0 \times 10^{-10}$  is our measured upper limit of  $\text{Br}_\chi$  and 1.164 seconds is the  ${}^6\text{He}$  lifetime. Isolating the mass mixing term  $\varepsilon/(m_n - m_\chi)$ , we obtain the final equation allowing us to probe the parameter space :

$$\left(\frac{\varepsilon}{m_n - m_\chi}\right)^2 = \frac{(2\pi)^3}{S^2} \frac{16\Gamma_\chi}{(m_n - S_{2n} - m_\chi)^2} (m_\alpha + 2m_n - S_{2n}). \quad (6.13)$$

In addition to our experimental limit on  $\text{Br}_\chi$ , this equation allows us to exclude a region of the parameter space probed with  ${}^6\text{He}$  as shown in Figure 6.1. In this figure, the red and purple vertical bands correspond to the stability of  ${}^9\text{Be}$  and  $\chi$ , respectively, as discussed in Section 2.2. The vertical grey band that goes from  $m_n$  to  $m_n - S_{2n} = 938.59$  MeV is a part of the open mass region that we cannot probe with the  ${}^6\text{He}$  dark decay. Finally, the grey dotted lines shows the behavior of the  $\chi$  parameter space with respect to three different branching ratios for the free neutron dark decay. One is at the 1% level which is the actual beam-bottle discrepancy and the other two are at 0.01% and 0.001%. These three lines were derived using the expression of the  $n \rightarrow \chi\gamma$  decay rate given in Equation 2.15.

### Constraints from UCN $\tau$ and Borexino

The blue and orange shaded areas represent the exclusion zones obtained from the UCN $\tau$  and Borexino experiments, respectively. The UCN $\tau$  experiment has already been discussed in Section 2.2.3, but Borexino has not yet been introduced. It is an apparatus located deep underground at the Gran Sasso National Laboratory in Italy. It was first designed to study low-energy solar neutrinos using a radiopure liquid scintillator in an environment optimized to minimize background contamination as much as possible [121]. From January 2012 to May 2013, the Borexino apparatus was used to test the conservation of the electric charge by looking for the charge nonconserving electron decay into a neutrino and a monoenergetic 256 keV photon [122] :

$$e^- \rightarrow \nu_e \gamma. \quad (6.14)$$

The results of this experiment were used by the authors in [120] to investigate the stability of the hydrogen atom against the dark decay. In this framework, the hydrogen atom would first undergo an electronic capture reaction which gives a neutron and a neutrino, followed by the dark decay of this neutron into a dark fermion and a monochromatic photon :

$$\text{H} \rightarrow \nu_e \chi \gamma. \quad (6.15)$$

As argued in this last article, this exotic process can be investigated using the data recorded with Borexino in [122] since the apparatus contains a large amount of hydrogen atoms. The authors in [120] used the experimental results from both the Borexino and the UCN $\tau$  experiment to derive their associated constraint on the mass mixing parameter responsible for the dark decay with respect to the mass of the emitted dark fermion.

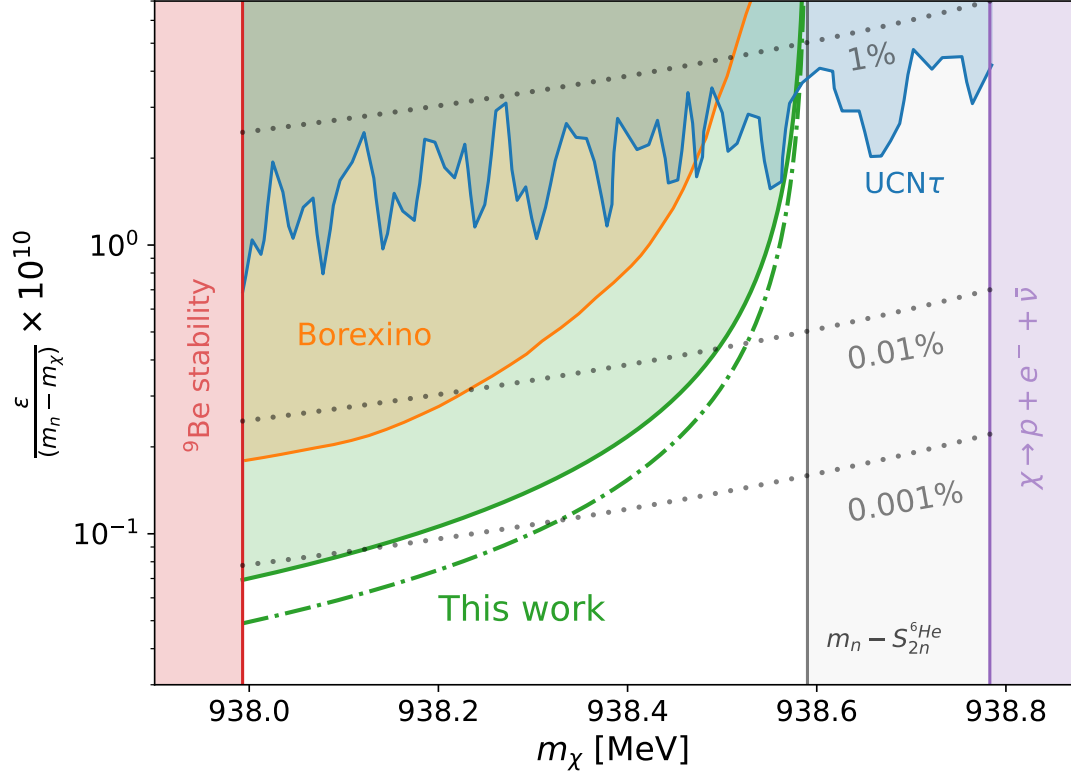


FIGURE 6.1 – Exclusion diagram of the parameter space for the dark fermion  $\chi$ . The red and purple vertical bands correspond to the  ${}^9\text{Be}$  and dark matter stability conditions. The grey vertical band corresponds to a part of the open mass range we are not sensitive to with  ${}^6\text{He}$ . The grey dotted lines correspond to three different neutron lifetime discrepancy scenario : the actual beam-bottle discrepancy at the 1% level and two additional cases at 0.01% and 0.001%. The blue and orange shaded region are results derived from the UCN $\tau$  and Borexino experiments respectively [120]. Finally, exclusion zones resulting from our experimental limit are shown in green.  $S=1$  is represented by the dash-dotted line and  $S=0.5$  with the solid line.

## Conclusion

The green shaded area in Figure 6.1 represents the exclusion zone obtained with Equation 6.13 using the conservative value of  $S=0.5$  for the wavefunction overlap. The dash-dotted green is obtained with the same calculation, but with  $S=1$ . The results show a clear improvement over the other two competitive constraints from Borexino and UCN $\tau$ . Our calculations reach branching ratios of  $\mathcal{O}(10^{-4} - 10^{-5})$  in order for the free neutron dark decay to be consistent with our data in more than half of the mass range probed by  ${}^6\text{He}$ . The last part remains largely under the actual beam-bottle discrepancy at  $\mathcal{O}(10^{-2})$ . Only a fraction goes beyond this level when  $m_\chi \rightarrow m_n - S_{2n}$  where Equation 6.13 diverges. In the end, if no other reason can suppress or even prevent the  ${}^6\text{He}$  dark decay, then this result completely excludes the dark decay as a solution to the neutron lifetime anomaly in the  $\approx 75\%$  of the mass range probed with  ${}^6\text{He}$ . The remaining  $\approx 25\%$  seems to be fully covered by the UCN $\tau$  but the reader should be reminded that this experiment (and the data from Borexino as well) only probes the decay  $n \rightarrow \chi\gamma$ .

### 6.2.4 $\phi$ parameter space

The constraint obtained for the parameter space of the dark fermion  $\chi$  can also be used to further limit the dark decay model. Although the scalar boson  $\phi$  that appears in the decay  $n \rightarrow \chi\phi$  is not involved in the final state of the investigated nuclear dark decay  ${}^6\text{He} \rightarrow {}^4\text{He} + n + \chi$ , its parameter space  $(m_\phi, |\lambda_\phi|)$  can still be probed with our result. As suggested in [78], the final state dark fermion  $\chi$  can also play the role of the intermediate dark fermion  $\tilde{\chi}$  that mixes with the neutron. In that specific scenario, the parameter space of each dark fermions is :

$$\left(m_\chi, \frac{\varepsilon}{m_n - m_\chi}\right) \equiv \left(m_{\tilde{\chi}}, \frac{\varepsilon}{m_n - m_{\tilde{\chi}}}\right), \quad (6.16)$$

and our result obtained with the  ${}^6\text{He}$  can be injected into the decay rate formula of the  $n \rightarrow \chi\phi$  in Equation 2.17.

In the following work, we first consider the actual beam-bottle discrepancy and a second neutron lifetime discrepancy at the 0.001% level. These discrepancies lead to decay rate values of  $\Gamma_\chi(1\%) = 8.02 \times 10^{-27}$  MeV and  $\Gamma_\chi(0.001\%) = 7.49 \times 10^{-30}$  MeV. Different values of  $m_\chi$  and  $\varepsilon/(m_n - m_\chi)$  consistent with their associated discrepancy can be evaluated in Figure 6.1 where the grey dotted lines cross with the green solid line. These values are listed in Table 6.1.

Discrepancy	$\Gamma_\chi$ (MeV)	$m_\chi$ (MeV)	$\varepsilon/(m_n - m_\chi)$	$m_\phi^{\max}$ (MeV)
1%	$8.02 \times 10^{-27}$	938.590	$5.0 \times 10^{-10}$	0.975
0.001%	$7.49 \times 10^{-30}$	938.100	$0.09 \times 10^{-10}$	1.465

TABLE 6.1 – Parameters used to compute exclusion areas in the parameter space of the dark scalar  $\phi$ .

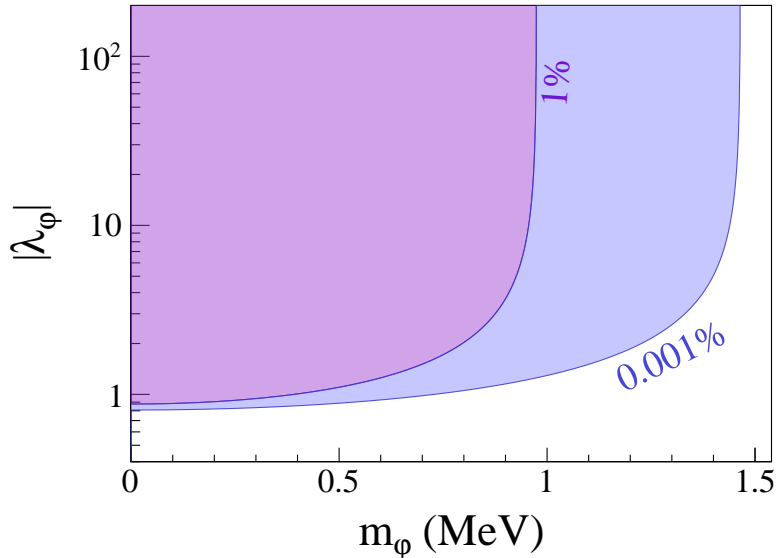


FIGURE 6.2 – Exclusion diagram of the parameter space for the dark scalar  $\phi$ . The shaded region in blue corresponds to a neutron lifetime discrepancy of 0.001%, whereas the purple shaded part is compatible with the actual beam-bottle discrepancy.

Subsequently, these values can be injected into the  $n \rightarrow \chi\phi$  decay rate in Equation 2.17 to probe the parameter space of the dark scalar  $\phi$  as shown in Figure 6.2. As already mentioned in Section 2.2.1, there is no specific mass hierarchy between  $\chi$  and  $\phi$  in the original  $n \rightarrow \chi\phi$  decay. Using our results from  ${}^6\text{He}$  obviously forces  $m_\phi \approx 1$  MeV, since we have  $937.993 \leq m_\chi \lesssim m_n - S_{2n}$  MeV. On the other hand, the maximum mass  $m_\phi^{\text{max}}$  for both discrepancies listed in Table 6.1 is still consistent with  $\phi$  being a dark matter candidate since we have  $m_\phi^{\text{max}} \ll m_p + m_e$ .

### 6.3 Dark decay in ${}^{17}\text{C}$

As discussed in Section 2.3.2, the  ${}^{17}\text{C}$  nucleus can still be used to look for dark decays through the channel  ${}^{17}\text{C} \rightarrow {}^{16}\text{C} + \chi$ . The presence of a dark decay in this nucleus can be probed thanks to the  $\beta n$  channel in the  ${}^{16}\text{C}$  disintegration. Here, we present simulations that reproduce the decay of  ${}^{17}\text{C}$  using Monte Carlo methods where a nonzero dark branching ratio is introduced to study the impact it would have with respect to neutron detection.

#### 6.3.1 Monte Carlo simulations of the ${}^{17}\text{C}$ decay

The simulations were performed using the random number generator class in ROOT called TRandom3. In this work, we assume an experiment designed in a way similar to the one presented in this manuscript with  ${}^6\text{He}$ . A pure  ${}^{17}\text{C}$  beam is implanted within a catcher where the nuclei are stopped and subsequently decay. An implantation cycle lasts 10 seconds, with  $t_{\text{ON}} = 1.2$  s used to implant the beam. The time in each cycle is discretized into several steps with a duration  $t_{\text{step}} = 1$  ms, allowing one to obtain a good enough

precision since the smallest half-life involved is  $t_{1/2}({}^{17}\text{C}) = 193$  ms. The other half-lives included in the simulation are  $t_{1/2}({}^{17}\text{N}) = 4171$  ms and  $t_{1/2}({}^{16}\text{C}) = 750$  ms. The intensity of the  ${}^{17}\text{C}$  beam is taken to be  $r_0 = 10^5$  s $^{-1}$ . Therefore, at each time step during the 1.2 s of implantation, 100  ${}^{17}\text{C}$  nuclei are implanted. At each time step, if the population  $N_i$  of a particular isotope  $i$  is greater than zero, then a random number  $0 \leq P_j \leq 1$  is generated for each nucleus  $j$  in  $N_i$ . Finally, the randomly generated number  $P_j$  for each nucleus in  $N_i$  is compared with the coupling of the decay rate of the  $i$ -th isotope and the width of the time step. If we have :

- $(P_j > \frac{\log 2}{t_{1/2}^{(i)}} t_{\text{step}})$ , then the  $j$ -th nucleus survives and goes on the next time step,
- $(P_j \leq \frac{\log 2}{t_{1/2}^{(i)}} t_{\text{step}})$ , then the  $j$ -th nucleus decays and is removed from the population.

For each nucleus  $k$  that decays within  $t_{\text{step}}$ , a second random number  $0 \leq B_k \leq 1$  is generated to decide which branch the nucleus will follow. For  ${}^{17}\text{C}$ , we implemented the  $\beta$  decay,  $\beta n$  decay and the dark decay. The values of the branching ratio used for this nucleus are  $\text{Br}_{\beta n} = 0.284$ ,  $\text{Br}_{\chi} = 10^{-2}$ ,  $10^{-3}$  or  $10^{-6}$ , and, to ensure unity, the remaining branching ratio is defined as  $\text{Br}_{\beta} = 1 - \text{Br}_{\beta n} - \text{Br}_{\chi}$ . The potential  $\beta 2n$  branch is not simulated, as it would produce  ${}^{15}\text{N}$ , which is stable. For  ${}^{17}\text{N}$  and  ${}^{16}\text{C}$ , branching ratios of 0.951 and 0.993 were used for the  $\beta n$  decays. All lifetime and branching ratio values listed here are from NuDat3. In the case of  ${}^{17}\text{C}$ , the randomly generated number is compared to the different branching ratios, so that if we have :

- $(B_k \leq \text{Br}_{\chi})$ , then the population of  ${}^{16}\text{C}$  is increased by one,
- $(\text{Br}_{\chi} < B_k \leq \text{Br}_{\chi} + \text{Br}_{\beta n})$ , then a neutron is emitted,
- $(\text{Br}_{\chi} + \text{Br}_{\beta n} < B_k \leq 1)$ , then the population of  ${}^{17}\text{N}$  is increased by one.

The same logic applies for the other two isotopes, where a neutron is emitted if we have  $B_k \leq \text{Br}_{\beta n}$  ( ${}^{16}\text{C}$ ;  ${}^{17}\text{N}$ ). For simplicity, we assume a neutron detector with unit detection efficiency in the simulation. Therefore, no additional test is performed to check if an emitted neutron is observed or not. If a neutron is emitted within a time step, then it is detected within the same time step. Once a cycle is over, another one in which all initial abundances of isotopes are reset to zero begins until the maximum number of cycles is reached.

### 6.3.2 Result of the simulations

As mentioned above, the simulations were performed with three different values for the dark decay branching ratio. The first is at  $10^{-2}$  and serves as a boundary scenario that emphasizes the effect of a dark decay in  ${}^{17}\text{C}$ . Another simulation was performed with a branching ratio of  $10^{-6}$ , better aligned with the upper limit estimated by Pfützner and Riisager in [79]. Finally, a simulation was also performed with an intermediate branching ratio of  $10^{-3}$ . The number of cycles is 2000 for the simulations with  $\text{Br}_{\chi} = 1\%$  or  $0.1\%$

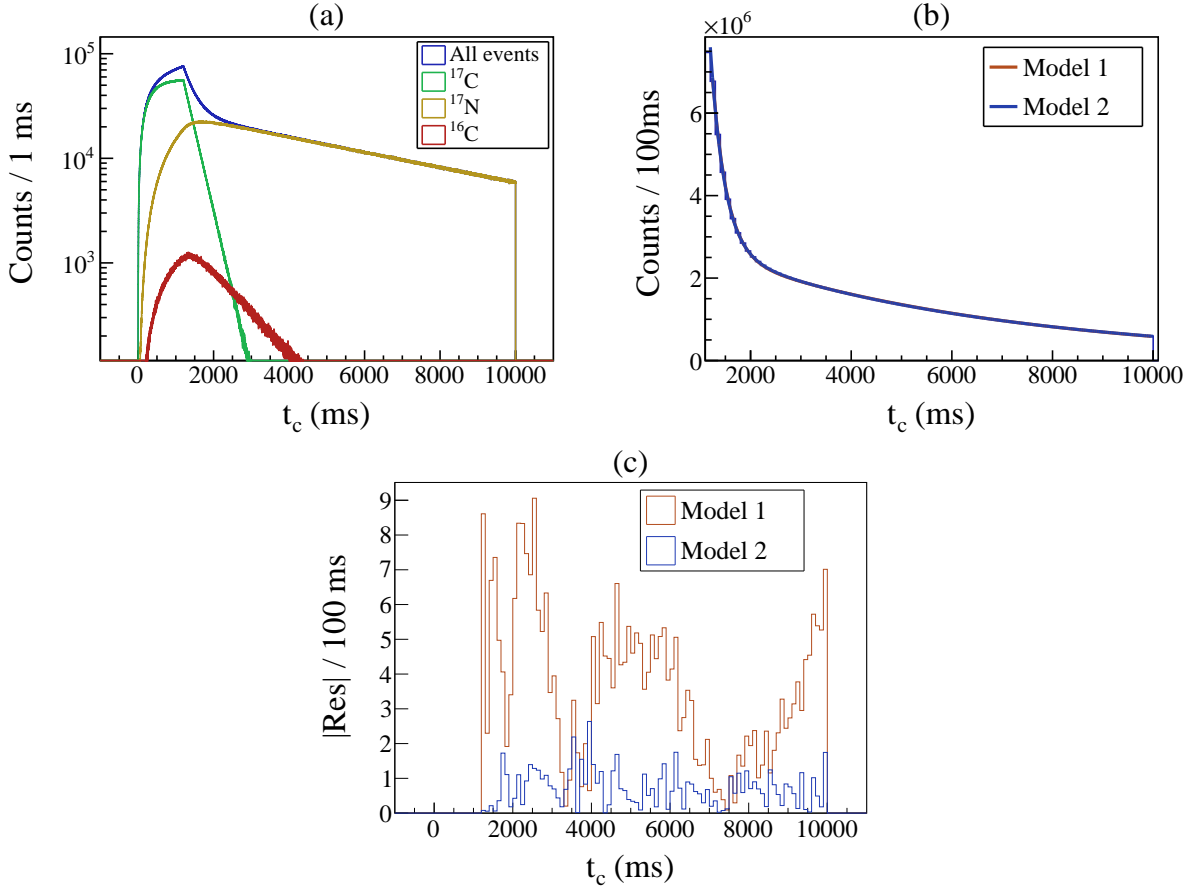


FIGURE 6.3 – (a) Result of the simulation with  $\text{Br}_\chi = 1\%$ . The events are distributed with respect to their time  $t_c$  within a cycle. The parent nuclei responsible for each event are listed in the legend. The parent nucleus revealing the dark decay is  $^{16}\text{C}$ . (b) Fit of the data starting at  $t_{\text{ON}}$ . Model 1 corresponds to Equation 6.18 and Model 2 to Equation 6.17. (c) Absolute value of the residuals with respect to each fit.

and 10000 with  $\text{Br}_\chi = 10^{-6}$ . This corresponds to  $\approx 5\text{h}30$  and  $\approx 27\text{h}45$  of beam time, respectively. The results with  $\text{Br}_\chi = 1\%$  are shown in Figure 6.3. Figure 6.3 (a) shows how neutron events are distributed with respect to their time  $t_c$  within an implantation cycle. The histogram also illustrates how the aggregated distribution (blue line) is partitioned relative to the parent nucleus. Figure 6.3 (b) shows a fit performed on the data between  $t_{\text{ON}} = 1.2$  and 10 s.

Since neutron detection in this part should follow the lifetime of all nuclei involved in neutron emission, in the case of a dark decay the equation should read :

$$N(t_c) = N_1 e^{-\lambda_1(t_c - t_{\text{ON}})} + N_2 e^{-\lambda_2(t_c - t_{\text{ON}})} + N_3 e^{-\lambda_3(t_c - t_{\text{ON}})}, \quad (6.17)$$

where  $\lambda_i = \log 2 / t_{1/2}^{(i)}$  is the radioactive constant of the  $i$ -th nucleus. If there is no  $^{17}\text{C}$  dark decay, then Equation 6.17 turns into :

$$N(t_c) = N_1 e^{-\lambda_1(t_c - t_{\text{ON}})} + N_2 e^{-\lambda_2(t_c - t_{\text{ON}})}, \quad (6.18)$$

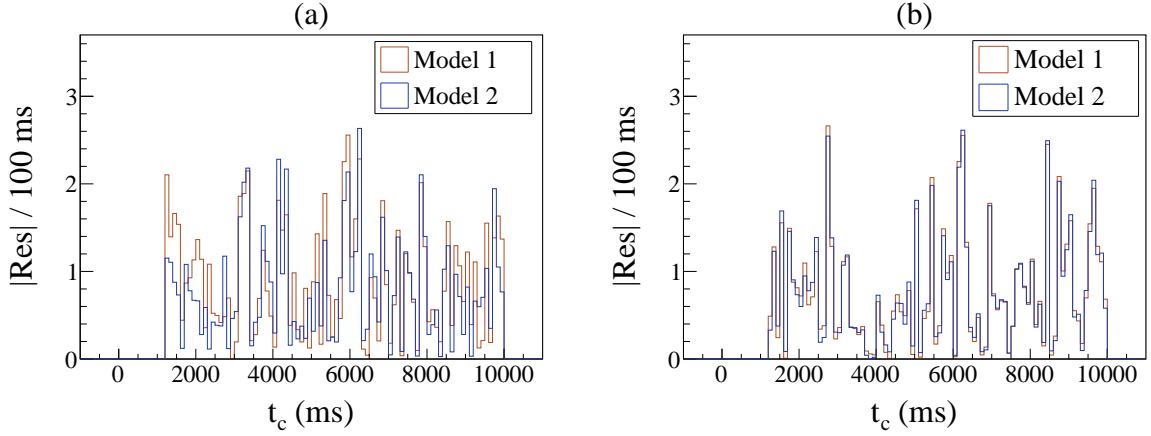


FIGURE 6.4 – Absolute value of the residuals for  $\text{Br}_\chi = 10^{-3}$  (a) and  $\text{Br}_\chi = 10^{-6}$  (b).

where the  $^{16}\text{C}$  component has simply been removed.

There is only a slight visual difference between the fits performed in Figure 6.3 (b) with the two different models. The deviation between between the data and the model can be highlighted by computing the residuals  $\text{Res}_i$  at each bin  $i$  like :

$$\text{Res}_i = \frac{N_{\text{meas},i} - N_{\text{model},i}}{\sqrt{N_{\text{meas},i}}}, \quad (6.19)$$

where  $N_{\text{meas},i}$  is the measured number of events in bin number  $i$  and  $N_{\text{model},i}$  the number of events expected by the fit model. This corresponds to the difference between the data and the model normalized by the statistical uncertainty of the bin. The absolute values for the residuals obtained with the two models are shown in Figure 6.3 (c). It can be seen that fitting the data without taking into account the simulated dark decay branch completely fails to reproduce the data with residuals that clearly exceed the usual  $3\sigma$  level.

The same procedure was applied for simulations with a dark decay probability of  $10^{-3}$  and  $10^{-6}$ . The residuals obtained for each branching ratio are shown in Figure 6.4. Although there is a notable difference between the residuals obtained in Figure 6.4 (a), it is not as large as in Figure 6.3 (c). In the case of a dark decay at the level of  $10^{-6}$ , the residuals shown in Figure 6.4 (b) are almost identical between the two models. Probing the  $^{17}\text{C}$  dark decay at a very low level would therefore require both more time and a higher beam intensity.

## 6.4 Conclusion and perspective

The experimental upper limit  $\text{Br}_\chi \leq 4.0 \times 10^{-10}$  obtained for the  $^6\text{He}$  dark decay was translated into a constraint on the model by achieving a theoretical calculation of the associated decay rate, including the 3-body phase space and the mass mixing term  $\varepsilon/(m_n - m_\chi)$ . The result shown in Figure 6.1 completely excludes dark decays as a solution to the neutron lifetime discrepancy in the mass range probed by  $^6\text{He}$ .

Although this result is in agreement with competitive constraints obtained by the

Borexino and UCN $\tau$  apparatus, it also provides a complementary point of view, since these experiments specifically looked for gamma emissions, leaving the  $n \rightarrow \chi\phi$  decay unprobed. Furthermore, even though our result reaches levels of  $\mathcal{O}(10^{-5})$  for the lifetime discrepancy, we only cover  $\approx 75\%$  of the open mass range for  $\chi$  to be a dark matter candidate.

In this chapter, we discussed the feasibility of investigating the whole open mass range using the proposed dark decay in  $^{17}\text{C}$ . An experiment could be performed at the Facility for Rare Isotope Beams (FRIB) at Michigan State University (MSU). Under optimal conditions, FRIB would be able to produce a stopped  $^{17}\text{C}$  beam with an intensity  $r_0 \approx 5.0 \times 10^5$  pps [123], comparable to the value used for the simulation. Using this beam in a setup similar to the one presented in Section 3.1 with a high-efficiency neutron counter ( $\varepsilon_n \approx 50\%$ ) could therefore be a solution to probe the entire mass range without looking for a specific gamma emission. In addition, if there are no unknown rules that could prevent dark decays in  $^{17}\text{C}$ , such an experiment could bring a final word on the neutron dark decay hypothesis.

# General conclusion

The neutron dark decay model has been proposed as a possible explanation to the neutron lifetime discrepancy between beam and bottle experiments. Shortly after the original 2018 publication, free neutron experiments investigating the two decay modes involving final-state SM particles published their results, all of which were incompatible with the actual beam-bottle discrepancy. The problem with such experiments is that they cannot probe the channel with dark particles only in the final state. A different method used to test the model was to look for the consequences of dark decays in neutron stars, particularly how they impact the stellar objects equation of state. These studies initially ruled out the dark decay model, as they could not reproduce neutron stars with masses of  $\approx 2M_{\odot}$ . Later, it was found that adding ingredients to the model such as repulsive dark matter interactions was enough to reconcile neutron stars with dark decays.

Dark decays have also been suggested to occur in a selection of radioactive nuclei that satisfy certain energy conditions. The difficulty of this approach is to find a good nucleus in which a dark decay would give a clear and unambiguous signature while covering a sufficiently large part of the open mass range for the dark fermion. The  ${}^6\text{He}$  proved to be a very good candidate for nuclear dark decay studies. Indeed, a dark decay in this nucleus would lead to the emission of a free neutron, a process otherwise forbidden in the standard  ${}^6\text{He}$  decay. Furthermore, this nucleus covers  $\approx 75\%$  of the open mass range for the fermion  $\chi$  to be a dark matter candidate. An experiment searching for a neutron dark decay in  ${}^6\text{He}$  was performed in June 2021 at GANIL. The data analysis resulted in a stringent upper limit of  $\text{Br}_{\chi} \leq 4.0 \times 10^{-10}$  with a 95% confidence level. This experimental result was then translated into a strong constraint on the mass mixing parameter responsible for the dark decay. Calculations including the three-body phase space resulted in limits well below the level of the actual beam-bottle discrepancy in the mass range probed with  ${}^6\text{He}$ .

This result provides a complementary picture to the various limits obtained in free neutron experiments or to the exclusion zone adapted from Borexino data. Indeed, nuclear dark decays directly probe the mass mixing mechanism, whereas the other experiments

relied on the detection of a specific  $\gamma$  ray or  $e^+e^-$  pair which may simply be unavailable channels. In the last chapter, we have discussed a possible way to probe this mechanism for the entire range of  $m_\chi$  using the  $^{17}\text{C}$  nucleus. A dark decay in this isotope could be evidenced thanks to the different lifetimes of all the  $\beta n$  channels. An experiment using a low energy  $^{17}\text{C}$  beam could be carried out at a facility such as FRIB. Using an experimental setup similar to the one presented in this thesis could further constrain the mass mixing parameter in the entire mass range.

Finally, the situation could also be clarified in the near future thanks to all the forthcoming experiments designed to measure the neutron lifetime with a better level of precision. The various methods discussed in this thesis should provide complementary results and possibly resolve the lifetime discrepancy. But, if the discrepancy remains, then this would strengthen the possibility that new neutron physics is indeed at work.

# Appendix A

## Compilation of $\lambda$ measurements

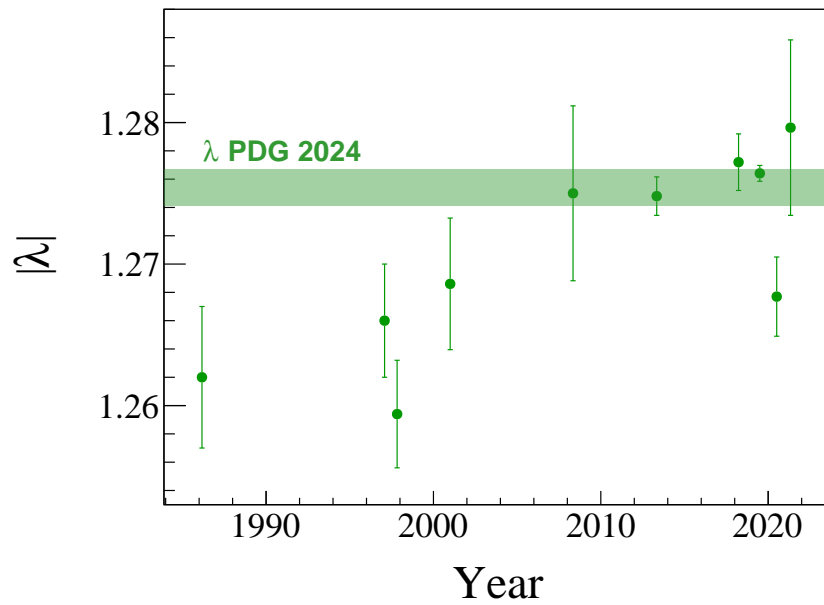


FIGURE A.1 – Values of  $|\lambda|$  used by the PDG to compute their weighted average.

# Appendix B

## Calculation of $\Gamma_{n \rightarrow \chi\phi}$

Achieving a decay rate equation alone can be very hard, especially for experimentalists. At least it was for me. Here, we provide a relatively detailed step-by-step description on how to compute the decay rate for the  $n \rightarrow \chi\phi$  decay, as given in [76, 78]. This demonstration requires knowledge of underlying concepts such as relativistic kinematics or how to use Feynman rules. These topics have been addressed in many particle physics textbooks such as Griffith's, Thomson's, Pal's, and others. Hence, all objects used will be briefly presented and the reader is advised to go through any of these books for more details.

### Useful expressions and identities

#### General decay rate formula

This equation was already discussed in the last chapter of this manuscript. It expresses the differential decay rate  $d\Gamma$  of any decay process like :

$$d\Gamma = \frac{(2\pi)^4}{2M} |\mathcal{M}|^2 d\Phi_n, \quad (\text{B.1})$$

where  $M$  is the mass of the decaying body,  $\mathcal{M}$  is the Lorentz-invariant matrix element and  $d\Phi_n$  is the  $n$ -body phase space factor. The matrix element, also called the decay amplitude, contains the fundamental description of the process. On the other hand, phase space is concerned with kinematics and its calculation depends on the number  $n$  of particles in the final state.

#### Integration over the 2-body phase space

The demonstration on how to integrate the phase space factor for any decay with 2 particles in the final state can be found in any of the books mentioned above. Using natural units  $\hbar = c = 1$ , the result is :

$$d\Gamma = \frac{p^*}{32\pi^2 M^2} |\mathcal{M}|^2 d\Omega, \quad (\text{B.2})$$

where  $p^*$  is the momentum in the center-of-mass frame of reference and  $\Omega$  is the solid angle of the emitted particles. The momentum  $p^* = |\mathbf{p}_1| = |\mathbf{p}_2|$  can be expressed as :

$$p^* = \frac{\sqrt{\lambda(M^2, m_1^2, m_2^2)}}{2M}, \quad (\text{B.3})$$

where  $\lambda(a, b, c) = a^2 + b^2 + c^2 - 2ab - 2ac - 2bc$  is known as the Källén function.

### Completeness identities for Dirac spinors

Dirac spinors are mathematical objects that are used in quantum field theory to describe fermions, such as electrons or quarks. A spinor is a  $4 \times 1$  matrix that incorporates both the particle and antiparticle spin states and complies with the Dirac equation. If we have a fermion with momentum  $\mathbf{p}$  and spin  $s$ , described by the spinor  $u(\mathbf{p}, s)$  or an antifermion described by the spinor  $v(\mathbf{p}, s)$ , then it can be shown that :

$$\sum_s u(\mathbf{p}, s) \bar{u}(\mathbf{p}, s) = \not{p} + m, \quad (\text{B.4})$$

$$\sum_s v(\mathbf{p}, s) \bar{v}(\mathbf{p}, s) = \not{p} - m, \quad (\text{B.5})$$

where  $\not{p} = \gamma^\mu p_\mu$  with  $p$  the 4-momentum,  $\gamma^\mu$  represents the gamma matrices with  $\mu = 0, 1, 2, 3$  and  $\bar{u} = u^\dagger \gamma^0$  is the adjoint Dirac spinor. Finally,  $m \equiv m \mathcal{I}_4$  is the mass of the particle and  $\mathcal{I}_4$  is the identity matrix. These relations are often referred to as completeness identities.

### Trace identities

Here are some identities that are useful in calculating  $\Gamma_{n \rightarrow \chi\phi}$  :

$$\text{Tr}(\gamma^{\mu_1} \gamma^{\mu_2} \dots \gamma^{\mu_{2n+1}}) = 0, \quad (\text{B.6})$$

$$\text{Tr}(\mathcal{I}_4) = 4, \quad (\text{B.7})$$

$$\text{Tr}(\not{a} \not{b}) = 4ab. \quad (\text{B.8})$$

The first identity means that the trace of any odd number of gamma matrices is equal to zero.

### Obtaining the expression for $\Gamma_{n \rightarrow \chi\phi}$

We are now ready to do the calculation. First, we recall the effective Lagrangian of the decay :

$$\mathcal{L} = \frac{\lambda_\phi \varepsilon}{m_n - m_{\tilde{\chi}}} \bar{\chi} n \phi^*, \quad (\text{B.9})$$

which is the classical form of a point-like interaction with three fields. Using the Feynman rules, we can obtain the expression of  $\mathcal{M}$  from this diagram :

$$\mathcal{M} = \frac{\lambda_\phi \varepsilon}{m_n - m_{\tilde{\chi}}} \bar{\chi}(\mathbf{p}_\chi, s_\chi) n(\mathbf{p}_n, s_n). \quad (\text{B.10})$$

Therefore we have :

$$|\mathcal{M}|^2 = |\lambda_\phi|^2 \left( \frac{\varepsilon}{m_n - m_\chi} \right)^2 [\bar{n}\chi][\bar{\chi}n]. \quad (\text{B.11})$$

We now need to compute the spin-averaged matrix element :

$$\overline{|\mathcal{M}|^2} = \frac{1}{2} \sum_{s_n} \sum_{s_\chi} |\mathcal{M}|^2. \quad (\text{B.12})$$

Using the completeness identities and Casimir's trick we obtain :

$$\overline{|\mathcal{M}|^2} = \frac{|\lambda_\phi|^2}{2} \left( \frac{\varepsilon}{m_n - m_{\tilde{\chi}}} \right)^2 \text{Tr}[(\not{p}_n + m_n)(\not{p}_\chi + m_\chi)], \quad (\text{B.13})$$

which in turn gives :

$$\overline{|\mathcal{M}|^2} = 2|\lambda_\phi|^2 \left( \frac{\varepsilon}{m_n - m_{\tilde{\chi}}} \right)^2 [p_n p_\chi + m_n m_\chi]. \quad (\text{B.14})$$

Defining the 4-vectors as  $p_n = (m_n, \mathbf{0})$  and  $p_\chi = (E_\chi, \mathbf{p}_\chi)$  we have :

$$[p_n p_\chi + m_n m_\chi] = m_n [E_\chi + m_\chi]. \quad (\text{B.15})$$

It can be shown for a 2-body decay in the form  $A \rightarrow B + C$ , that we can express  $E_B = (m_A^2 - m_C^2 + m_B^2)/2m_A$  in the center-of-mass frame. Therefore, we can write :

$$E_\chi = \frac{m_n^2 - m_\phi^2 + m_\chi^2}{2m_n}. \quad (\text{B.16})$$

Finally, the spin-averaged matrix element is :

$$\overline{|\mathcal{M}|^2} = |\lambda_\phi|^2 \left( \frac{\varepsilon}{m_n - m_{\tilde{\chi}}} \right)^2 [(1+x)^2 - y^2] m_n^2, \quad (\text{B.17})$$

where  $x = m_\chi/m_n$  and  $y = m_\phi/m_n$ . Now we can focus on the expression of the momentum  $p^*$ . Using the equation in the previous section, we can write :

$$p^* = \frac{\sqrt{[m_n^2 - (m_\chi + m_\phi)^2][m_n^2 - (m_\chi - m_\phi)^2]}}{2m_n}, \quad (\text{B.18})$$

where the numerator is a factorized form of the Källén function. Taking out all  $m_n$  outside of the square root and rearranging the different factors inside gives :

$$p^* = \frac{m_n}{2} \sqrt{[(1-x)^2 - y^2][(1+x)^2 - y^2]}. \quad (\text{B.19})$$

We now have all ingredients and we simply need to perform the remaining integration over  $d\Omega$ . Finally, the decay rate for the decay  $n \rightarrow \chi\phi$  is :

$$\Gamma_{n \rightarrow \chi\phi} = \frac{|\lambda_\phi|^2}{16\pi} \sqrt{[(1-x)^2 - y^2][(1+x)^2 - y^2]^3} \left( \frac{\varepsilon}{m_n - m_{\tilde{\chi}}} \right)^2 m_n. \quad (\text{B.20})$$

# Bibliography

- [1] Enrico Fermi. “Tentativo di una Teoria Dei Raggi  $\beta$ ”. In: *Il Nuovo Cimento* 11 (1934), pp. 1–19. DOI: <https://doi.org/10.1007/BF02959820>.
- [2] Steffen Turkat et al. “Systematics of  $\log ft$  values for  $\beta^-$ , and EC/ $\beta^+$  transitions”. In: *Atomic Data and Nuclear Data Tables* 152 (2023), p. 101584. ISSN: 0092-640X. DOI: <https://doi.org/10.1016/j.adt.2023.101584>. URL: <https://www.sciencedirect.com/science/article/pii/S0092640X23000128>.
- [3] J. C. Hardy and I. S. Towner. “Superaligned  $0^+ \rightarrow 0^+$  nuclear  $\beta$  decays: 2020 critical survey, with implications for  $V_{ud}$  and CKM unitarity”. In: *Phys. Rev. C* 102 (4 Oct. 2020), p. 045501. DOI: [10.1103/PhysRevC.102.045501](https://doi.org/10.1103/PhysRevC.102.045501). URL: <https://link.aps.org/doi/10.1103/PhysRevC.102.045501>.
- [4] Mikhail Gorchtein and Chien-Yeah Seng. “The Standard Model Theory of Neutron Beta Decay”. In: *Universe* 9.9 (2023). ISSN: 2218-1997. URL: <https://www.mdpi.com/2218-1997/9/9/422>.
- [5] D. M. Webber et al. “Measurement of the Positive Muon Lifetime and Determination of the Fermi Constant to Part-per-Million Precision”. In: *Phys. Rev. Lett.* 106 (4 Jan. 2011), p. 041803. DOI: [10.1103/PhysRevLett.106.041803](https://doi.org/10.1103/PhysRevLett.106.041803). URL: <https://link.aps.org/doi/10.1103/PhysRevLett.106.041803>.
- [6] V. Tishchenko et al. “Detailed report of the MuLan measurement of the positive muon lifetime and determination of the Fermi constant”. In: *Phys. Rev. D* 87 (5 Mar. 2013), p. 052003. DOI: [10.1103/PhysRevD.87.052003](https://doi.org/10.1103/PhysRevD.87.052003). URL: <https://link.aps.org/doi/10.1103/PhysRevD.87.052003>.
- [7] Makoto Kobayashi and Toshihide Maskawa. “CP-Violation in the Renormalizable Theory of Weak Interaction”. In: *Progress of Theoretical Physics* 49.2 (Feb. 1973), pp. 652–657. ISSN: 0033-068X. DOI: [10.1143/PTP.49.652](https://doi.org/10.1143/PTP.49.652). eprint: <https://academic.oup.com/ptp/article-pdf/49/2/652/5257692/49-2-652.pdf>. URL: <https://doi.org/10.1143/PTP.49.652>.
- [8] Dirk Dubbers and Michael G. Schmidt. “The neutron and its role in cosmology and particle physics”. In: *Rev. Mod. Phys.* 83 (4 Oct. 2011), pp. 1111–1171. DOI: [10.1103/RevModPhys.83.1111](https://doi.org/10.1103/RevModPhys.83.1111). URL: <https://link.aps.org/doi/10.1103/RevModPhys.83.1111>.

- [9] Andrzej Czarnecki, William J. Marciano, and Alberto Sirlin. “Radiative corrections to neutron and nuclear beta decays revisited”. In: *Phys. Rev. D* 100 (7 Oct. 2019), p. 073008. DOI: [10.1103/PhysRevD.100.073008](https://doi.org/10.1103/PhysRevD.100.073008). URL: <https://link.aps.org/doi/10.1103/PhysRevD.100.073008>.
- [10] R. L. Workman et al. “Review of Particle Physics”. In: *PTEP* 2022 (2022), p. 083C01. DOI: [10.1093/ptep/ptac097](https://doi.org/10.1093/ptep/ptac097).
- [11] Anonymous. “Minutes of the Meeting at Washington, April 29 to May 1, 1948”. In: *Phys. Rev.* 74 (9 Nov. 1948), pp. 1201–1253. DOI: [10.1103/PhysRev.74.1201](https://doi.org/10.1103/PhysRev.74.1201). URL: <https://link.aps.org/doi/10.1103/PhysRev.74.1201>.
- [12] J. M. Robson. “The Radioactive Decay of the Neutron”. In: *Phys. Rev.* 83 (2 July 1951), pp. 349–358. DOI: [10.1103/PhysRev.83.349](https://doi.org/10.1103/PhysRev.83.349). URL: <https://link.aps.org/doi/10.1103/PhysRev.83.349>.
- [13] F. M. Gonzalez et al. “Improved Neutron Lifetime Measurement with UCN $\tau$ ”. In: *Phys. Rev. Lett.* 127 (16 Oct. 2021), p. 162501. DOI: [10.1103/PhysRevLett.127.162501](https://doi.org/10.1103/PhysRevLett.127.162501). URL: <https://link.aps.org/doi/10.1103/PhysRevLett.127.162501>.
- [14] Fred E. Wietfeldt and Geoffrey L. Greene. “Colloquium: The neutron lifetime”. In: *Rev. Mod. Phys.* 83 (4 Nov. 2011), pp. 1173–1192. DOI: [10.1103/RevModPhys.83.1173](https://doi.org/10.1103/RevModPhys.83.1173). URL: <https://link.aps.org/doi/10.1103/RevModPhys.83.1173>.
- [15] J. S. Nico et al. “Measurement of the neutron lifetime by counting trapped protons in a cold neutron beam”. In: *Phys. Rev. C* 71 (5 May 2005), p. 055502. DOI: [10.1103/PhysRevC.71.055502](https://doi.org/10.1103/PhysRevC.71.055502). URL: <https://link.aps.org/doi/10.1103/PhysRevC.71.055502>.
- [16] James F. Ziegler. *SRIM - Stopping and Range of Ions in Matter*. URL: [srim.org](http://srim.org).
- [17] A. T. Yue et al. “Improved Determination of the Neutron Lifetime”. In: *Phys. Rev. Lett.* 111 (22 Nov. 2013), p. 222501. DOI: [10.1103/PhysRevLett.111.222501](https://doi.org/10.1103/PhysRevLett.111.222501). URL: <https://link.aps.org/doi/10.1103/PhysRevLett.111.222501>.
- [18] M.B. Chadwick et al. “ENDF/B-VII.0: Next Generation Evaluated Nuclear Data Library for Nuclear Science and Technology”. In: *Nuclear Data Sheets* 107.12 (2006). Evaluated Nuclear Data File ENDF/B-VII.0, pp. 2931–3060. ISSN: 0090-3752. DOI: <https://doi.org/10.1016/j.nds.2006.11.001>. URL: <https://www.sciencedirect.com/science/article/pii/S0090375206000871>.
- [19] A. P. Serebrov et al. “Search for explanation of the neutron lifetime anomaly”. In: *Phys. Rev. D* 103 (7 Apr. 2021), p. 074010. DOI: [10.1103/PhysRevD.103.074010](https://doi.org/10.1103/PhysRevD.103.074010). URL: <https://link.aps.org/doi/10.1103/PhysRevD.103.074010>.
- [20] F. E. Wietfeldt et al. “Comments on Systematic Effects in the NIST Beam Neutron Lifetime Experiment”. In: (2022). arXiv: [2209.15049](https://arxiv.org/abs/2209.15049).
- [21] W. Mampe et al. “Neutron lifetime measured with stored ultracold neutrons”. In: *Phys. Rev. Lett.* 63 (6 Aug. 1989), pp. 593–596. DOI: [10.1103/PhysRevLett.63.593](https://doi.org/10.1103/PhysRevLett.63.593). URL: <https://link.aps.org/doi/10.1103/PhysRevLett.63.593>.

- [22] A. P. Serebrov and A. K. Fomin. “Monte Carlo simulation of the experiment MAMBO I and possible correction of neutron lifetime result”. In: (2009). arXiv: [0808.3975](https://arxiv.org/abs/0808.3975) [nucl-ex].
- [23] A. Steyerl et al. “Quasielastic scattering in the interaction of ultracold neutrons with a liquid wall and application in a reanalysis of the Mambo I neutron-lifetime experiment”. In: *Phys. Rev. C* 85 (6 June 2012), p. 065503. DOI: [10.1103/PhysRevC.85.065503](https://doi.org/10.1103/PhysRevC.85.065503). URL: <https://link.aps.org/doi/10.1103/PhysRevC.85.065503>.
- [24] S. Arzumanov et al. “A measurement of the neutron lifetime using the method of storage of ultracold neutrons and detection of inelastically up-scattered neutrons”. In: *Phys. Lett. B* 745 (2015), pp. 79–89. DOI: [10.1016/j.physletb.2015.04.021](https://doi.org/10.1016/j.physletb.2015.04.021).
- [25] W. Mampe et al. “Measuring neutron lifetime by storing ultracold neutrons and detecting inelastically scattered neutrons”. In: *JETP Lett.* 57 (1993), pp. 82–87. URL: [http://jetpletters.ru/ps/1175/article\\_17737.shtml](http://jetpletters.ru/ps/1175/article_17737.shtml).
- [26] A. Serebrov et al. “Measurement of the neutron lifetime using a gravitational trap and a low-temperature Fomblin coating”. In: *Physics Letters B* 605.1 (2005), pp. 72–78. ISSN: 0370-2693. DOI: <https://doi.org/10.1016/j.physletb.2004.11.013>. URL: <https://www.sciencedirect.com/science/article/pii/S0370269304015552>.
- [27] A. P. Serebrov et al. “Neutron lifetime measurements with a large gravitational trap for ultracold neutrons”. In: *Phys. Rev. C* 97 (5 May 2018), p. 055503. DOI: [10.1103/PhysRevC.97.055503](https://doi.org/10.1103/PhysRevC.97.055503). URL: <https://link.aps.org/doi/10.1103/PhysRevC.97.055503>.
- [28] R. W. Pattie et al. “Measurement of the neutron lifetime using a magneto-gravitational trap and in situ detection”. In: *Science* 360.6389 (2018), pp. 627–632. DOI: [10.1126/science.aan8895](https://doi.org/10.1126/science.aan8895). eprint: <https://www.science.org/doi/pdf/10.1126/science.aan8895>. URL: <https://www.science.org/doi/abs/10.1126/science.aan8895>.
- [29] J. Byrne and P. G. Dawber. “A Revised Value for the Neutron Lifetime Measured Using a Penning Trap”. In: *EPL* 33 (1996), p. 187. DOI: [10.1209/ep1/i1996-00319-x](https://doi.org/10.1209/ep1/i1996-00319-x).
- [30] N. Sumi et al. “Precise Neutron Lifetime Measurement Using Pulsed Neutron Beams at J-PARC”. In: *Proceedings of the 3rd J-PARC Symposium (J-PARC2019)*. DOI: [10.7566/JPSCP.33.011056](https://doi.org/10.7566/JPSCP.33.011056). URL: <https://journals.jps.jp/doi/abs/10.7566/JPSCP.33.011056>.
- [31] J. Byrne et al. “Measurement of the neutron lifetime by counting trapped protons”. In: *Phys. Rev. Lett.* 65 (1990), pp. 289–292. DOI: [10.1103/PhysRevLett.65.289](https://doi.org/10.1103/PhysRevLett.65.289).
- [32] A. Pichlmaier et al. “Neutron lifetime measurement with the UCN trap-in-trap MAMBO II”. In: *Physics Letters B* 693.3 (2010), pp. 221–226. ISSN: 0370-2693. DOI: <https://doi.org/10.1016/j.physletb.2010.08.032>. URL: <https://www.sciencedirect.com/science/article/pii/S0370269310009792>.

- [33] V. F. Ezhov et al. “Measurement of the neutron lifetime with ultra-cold neutrons stored in a magneto-gravitational trap”. In: *JETP Lett.* 107.11 (2018), pp. 671–675. DOI: [10.1134/S0021364018110024](https://doi.org/10.1134/S0021364018110024). arXiv: [1412.7434](https://arxiv.org/abs/1412.7434) [nucl-ex].
- [34] P. Bopp et al. “The Beta Decay Asymmetry of the Neutron and  $g_A/g_V$ ”. In: *Phys. Rev. Lett.* 56 (1986). [Erratum: *Phys.Rev.Lett.* 57, 1192 (1986)], p. 919. DOI: [10.1103/PhysRevLett.56.919](https://doi.org/10.1103/PhysRevLett.56.919).
- [35] B. Erokolimsky et al. “Corrigendum: Corrected value of the beta-emission asymmetry in the decay of polarized neutrons measured in 1990”. In: (1997). [Erratum: *Phys.Lett.B* 412, 240–241 (1997)]. DOI: [10.1016/S0370-2693\(97\)01004-6](https://doi.org/10.1016/S0370-2693(97)01004-6).
- [36] P. Liaud et al. “The measurement of the beta asymmetry in the decay of polarized neutrons”. In: *Nucl. Phys. A* 612 (1997), pp. 53–81. DOI: [10.1016/S0375-9474\(96\)00325-9](https://doi.org/10.1016/S0375-9474(96)00325-9).
- [37] Yu. A. Mostovoi et al. “Experimental value of  $G(A)/G(V)$  from a measurement of both P-odd correlations in free-neutron decay”. In: *Phys. Atom. Nucl.* 64 (2001), pp. 1955–1960. DOI: [10.1134/1.1423745](https://doi.org/10.1134/1.1423745).
- [38] M. Beck et al. “Improved determination of the  $\beta$ - $\bar{\nu}_e$  angular correlation coefficient  $a$  in free neutron decay with the *aSPECT* spectrometer”. In: *Phys. Rev. C* 101.5 (2020), p. 055506. DOI: [10.1103/PhysRevC.101.055506](https://doi.org/10.1103/PhysRevC.101.055506). arXiv: [1908.04785](https://arxiv.org/abs/1908.04785) [nucl-ex].
- [39] M. Schumann et al. “Measurement of the Proton Asymmetry Parameter C in Neutron Beta Decay”. In: *Phys. Rev. Lett.* 100 (2008), p. 151801. DOI: [10.1103/PhysRevLett.100.151801](https://doi.org/10.1103/PhysRevLett.100.151801). arXiv: [0712.2442](https://arxiv.org/abs/0712.2442) [hep-ph].
- [40] D. Mund et al. “Determination of the Weak Axial Vector Coupling from a Measurement of the Beta-Asymmetry Parameter A in Neutron Beta Decay”. In: *Phys. Rev. Lett.* 110 (2013), p. 172502. DOI: [10.1103/PhysRevLett.110.172502](https://doi.org/10.1103/PhysRevLett.110.172502). arXiv: [1204.0013](https://arxiv.org/abs/1204.0013) [hep-ex].
- [41] M. A. -P. Brown et al. “New result for the neutron  $\beta$ -asymmetry parameter  $A_0$  from UCNA”. In: *Phys. Rev. C* 97.3 (2018), p. 035505. DOI: [10.1103/PhysRevC.97.035505](https://doi.org/10.1103/PhysRevC.97.035505). arXiv: [1712.00884](https://arxiv.org/abs/1712.00884) [nucl-ex].
- [42] B. Märkisch et al. “Measurement of the Weak Axial-Vector Coupling Constant in the Decay of Free Neutrons Using a Pulsed Cold Neutron Beam”. In: *Phys. Rev. Lett.* 122.24 (2019), p. 242501. DOI: [10.1103/PhysRevLett.122.242501](https://doi.org/10.1103/PhysRevLett.122.242501). arXiv: [1812.04666](https://arxiv.org/abs/1812.04666) [nucl-ex].
- [43] M. T. Hassan et al. “Measurement of the neutron decay electron-antineutrino angular correlation by the aCORN experiment”. In: *Phys. Rev. C* 103.4 (2021), p. 045502. DOI: [10.1103/PhysRevC.103.045502](https://doi.org/10.1103/PhysRevC.103.045502). arXiv: [2012.14379](https://arxiv.org/abs/2012.14379) [nucl-ex].
- [44] P. Plattner et al. “Nuclear Charge Radius of  $^{26m}\text{Al}$  and Its Implication for  $V_{ud}$  in the Quark Mixing Matrix”. In: *Phys. Rev. Lett.* 131 (22 Nov. 2023), p. 222502. DOI: [10.1103/PhysRevLett.131.222502](https://doi.org/10.1103/PhysRevLett.131.222502). URL: <https://link.aps.org/doi/10.1103/PhysRevLett.131.222502>.

- [45] D. Po čani ć et al. “Precise Measurement of the  $\pi^+ \rightarrow \pi^0 e^+ \nu$  Branching Ratio”. In: *Phys. Rev. Lett.* 93 (18 Oct. 2004), p. 181803. DOI: [10.1103/PhysRevLett.93.181803](https://doi.org/10.1103/PhysRevLett.93.181803). URL: <https://link.aps.org/doi/10.1103/PhysRevLett.93.181803>.
- [46] W.C. Feldman, G.F. Auchampaugh, and D.M. Drake. “A technique to measure the neutron lifetime from low-earth orbit”. In: *Nuclear Instruments and Methods in Physics Research Section A: Accelerators, Spectrometers, Detectors and Associated Equipment* 287.3 (1990), pp. 595–605. ISSN: 0168-9002. DOI: [https://doi.org/10.1016/0168-9002\(90\)91584-X](https://doi.org/10.1016/0168-9002(90)91584-X). URL: <https://www.sciencedirect.com/science/article/pii/016890029091584X>.
- [47] Jack T. Wilson et al. “Space-based measurement of the neutron lifetime using data from the neutron spectrometer on NASA’s MESSENGER mission”. In: *Phys. Rev. Res.* 2 (2 June 2020), p. 023316. DOI: [10.1103/PhysRevResearch.2.023316](https://doi.org/10.1103/PhysRevResearch.2.023316). URL: <https://link.aps.org/doi/10.1103/PhysRevResearch.2.023316>.
- [48] Jack T. Wilson et al. “Measurement of the free neutron lifetime using the neutron spectrometer on NASA’s Lunar Prospector mission”. In: *Phys. Rev. C* 104 (4 Oct. 2021), p. 045501. DOI: [10.1103/PhysRevC.104.045501](https://doi.org/10.1103/PhysRevC.104.045501). URL: <https://link.aps.org/doi/10.1103/PhysRevC.104.045501>.
- [49] David J. Lawrence, Jack T. Wilson, and Patrick N. Peplowski. “Space-based measurements of neutron lifetime: Approaches to resolving the neutron lifetime anomaly”. In: *Nuclear Instruments and Methods in Physics Research Section A: Accelerators, Spectrometers, Detectors and Associated Equipment* 988 (2021), p. 164919. ISSN: 0168-9002. DOI: <https://doi.org/10.1016/j.nima.2020.164919>. URL: <https://www.sciencedirect.com/science/article/pii/S0168900220313164>.
- [50] K. Mishima et al. “Performance of the Full-equipped Spin Flip Chopper For Neutron Lifetime Experiment at J-PARC”. In: (2023). arXiv: [2312.12959](https://arxiv.org/abs/2312.12959).
- [51] Fred Wietfeldt and BL3 Collaboration Team. “The BL3 Beam Neutron Lifetime Experiment”. In: *APS April Meeting Abstracts*. Vol. 2022. APS Meeting Abstracts. Apr. 2022, T12.004, T12.004. URL: <https://ui.adsabs.harvard.edu/abs/2022APS..APRT12004W>.
- [52] Nicholas Floyd et al. “Status of the UCNProBe experiment”. In: *APS Meeting Abstracts*. APS Meeting Abstracts. Jan. 2023, E14.008, E14.008. URL: <https://ui.adsabs.harvard.edu/abs/2023APS..HAW14008F>.
- [53] M. Krivoš et al. “YAP:Ce scintillator as an absolute ultracold neutron detector”. In: (2024). arXiv: [2405.02309](https://arxiv.org/abs/2405.02309).
- [54] J. Auler et al. “ $\tau$ SPECT: A spin-flip loaded magnetic ultracold neutron trap for a determination of the neutron lifetime”. In: (2023). arXiv: [2311.00712](https://arxiv.org/abs/2311.00712).
- [55] M. J. Bales et al. “Precision Measurement of the Radiative  $\beta$  Decay of the Free Neutron”. In: *Phys. Rev. Lett.* 116 (24 June 2016), p. 242501. DOI: [10.1103/PhysRevLett.116.242501](https://doi.org/10.1103/PhysRevLett.116.242501). URL: <https://link.aps.org/doi/10.1103/PhysRevLett.116.242501>.

- [56] Raymond Daudel, Maurice Jean, and Marcel Lecoïn. “Sur la possibilité d’existence d’un type particulier de radioactivité phénomène de création e<sup>-</sup>”. In: *Journal de Physique et le Radium* 8.8 (1947), pp. 238–243. DOI: [10.1051/jphysrad:0194700808023800](https://doi.org/10.1051/jphysrad:0194700808023800). URL: <https://hal.science/jpa-00234057>.
- [57] S. G. Cohen. “The Decay of Neutrons into Neutral Hydrogen Atoms”. In: *Phys. Rev.* 84 (3 Nov. 1951), pp. 591–591. DOI: [10.1103/PhysRev.84.591](https://doi.org/10.1103/PhysRev.84.591). URL: <https://link.aps.org/doi/10.1103/PhysRev.84.591>.
- [58] S. G. Cohen, D. E. Murnick, and R. S. Raghavan. “Bound-state beta-decay and kinematic search for neutrino mass”. In: *Hyperfine Interactions* 33.1 (Mar. 1987), pp. 1–8. ISSN: 1572-9540. DOI: [10.1007/BF02394096](https://doi.org/10.1007/BF02394096). URL: <https://doi.org/10.1007/BF02394096>.
- [59] M. Faber et al. “Continuum-state and bound-state  $\beta^-$ -decay rates of the neutron”. In: *Phys. Rev. C* 80 (3 Sept. 2009), p. 035503. DOI: [10.1103/PhysRevC.80.035503](https://doi.org/10.1103/PhysRevC.80.035503). URL: <https://link.aps.org/doi/10.1103/PhysRevC.80.035503>.
- [60] M. Jung et al. “First observation of bound-state  $\beta^-$  decay”. In: *Phys. Rev. Lett.* 69 (15 Oct. 1992), pp. 2164–2167. DOI: [10.1103/PhysRevLett.69.2164](https://doi.org/10.1103/PhysRevLett.69.2164). URL: <https://link.aps.org/doi/10.1103/PhysRevLett.69.2164>.
- [61] F. Bosch et al. “Observation of Bound-State  $\beta^-$  Decay of Fully Ionized  $^{187}\text{Re}$ :  $^{187}\text{Re}-^{187}\text{Os}$  Cosmochronometry”. In: *Phys. Rev. Lett.* 77 (26 Dec. 1996), pp. 5190–5193. DOI: [10.1103/PhysRevLett.77.5190](https://doi.org/10.1103/PhysRevLett.77.5190). URL: <https://link.aps.org/doi/10.1103/PhysRevLett.77.5190>.
- [62] Leckenby, Guy et al. “Analysis methods to determine the bound-state beta-decay half-life of Thallium-205”. In: *EPJ Web Conf.* 279 (2023), p. 06010. DOI: [10.1051/epjconf/202327906010](https://doi.org/10.1051/epjconf/202327906010). URL: <https://doi.org/10.1051/epjconf/202327906010>.
- [63] Eugene Oks. “New results on the two-body decay of neutrons shed new light on neutron stars”. In: *New Astronomy* 113 (2024), p. 102275. ISSN: 1384-1076. DOI: <https://doi.org/10.1016/j.newast.2024.102275>. URL: <https://www.sciencedirect.com/science/article/pii/S1384107624000897>.
- [64] W. Schott et al. “An experiment for the measurement of the bound- $\beta$ -decay of the free neutron”. In: *The European Physical Journal A - Hadrons and Nuclei* 30.3 (Dec. 2006), pp. 603–611. ISSN: 1434-601X. DOI: [10.1140/epja/i2006-10136-3](https://doi.org/10.1140/epja/i2006-10136-3). URL: <https://doi.org/10.1140/epja/i2006-10136-3>.
- [65] Schott, Wolfgang et al. “Towards a first measurement of the free neutron bound beta decay detecting hydrogen atoms at a throughgoing beamtube in a high flux reactor”. In: *EPJ Web Conf.* 219 (2019), p. 04006. DOI: [10.1051/epjconf/201921904006](https://doi.org/10.1051/epjconf/201921904006). URL: <https://doi.org/10.1051/epjconf/201921904006>.
- [66] Zhang Shuo et al. *Proposal for Measurement of the Two-body Neutron Decay using Microcalorimeter*. 2023. arXiv: [2210.02314](https://arxiv.org/abs/2210.02314) [hep-ex]. URL: <https://arxiv.org/abs/2210.02314>.

- [67] Zurab Berezhiani. “Mirror World and its Cosmological Consequences”. In: *International Journal of Modern Physics A* 19.23 (2004), pp. 3775–3806. DOI: [10.1142/S0217751X04020075](https://doi.org/10.1142/S0217751X04020075). eprint: <https://doi.org/10.1142/S0217751X04020075>. URL: <https://doi.org/10.1142/S0217751X04020075>.
- [68] Zurab Berezhiani and Luís Bento. “Neutron–Mirror-Neutron Oscillations: How Fast Might They Be?” In: *Phys. Rev. Lett.* 96 (8 Feb. 2006), p. 081801. DOI: [10.1103/PhysRevLett.96.081801](https://doi.org/10.1103/PhysRevLett.96.081801). URL: <https://link.aps.org/doi/10.1103/PhysRevLett.96.081801>.
- [69] Wanpeng Tan. “Neutron oscillations for solving neutron lifetime and dark matter puzzles”. In: *Physics Letters B* 797 (2019), p. 134921. ISSN: 0370-2693. DOI: <https://doi.org/10.1016/j.physletb.2019.134921>. URL: <https://www.sciencedirect.com/science/article/pii/S0370269319306434>.
- [70] Wanpeng Tan. “Neutron Lifetime Anomaly and Mirror Matter Theory”. In: *Universe* 9.4 (2023). ISSN: 2218-1997. DOI: [10.3390/universe9040180](https://doi.org/10.3390/universe9040180). URL: <https://www.mdpi.com/2218-1997/9/4/180>.
- [71] Zurab Berezhiani. “Neutron lifetime puzzle and neutron–mirror neutron oscillation”. In: *The European Physical Journal C* 79.6 (June 2019), p. 484. DOI: [10.1140/epjc/s10052-019-6995-x](https://doi.org/10.1140/epjc/s10052-019-6995-x). URL: <https://doi.org/10.1140/epjc/s10052-019-6995-x>.
- [72] L. J. Broussard et al. “Experimental Search for Neutron to Mirror Neutron Oscillations as an Explanation of the Neutron Lifetime Anomaly”. In: *Phys. Rev. Lett.* 128 (21 May 2022), p. 212503. DOI: [10.1103/PhysRevLett.128.212503](https://doi.org/10.1103/PhysRevLett.128.212503). URL: <https://link.aps.org/doi/10.1103/PhysRevLett.128.212503>.
- [73] Surjeet Rajendran and Harikrishnan Ramani. “Composite solution to the neutron lifetime anomaly”. In: *Phys. Rev. D* 103 (3 Feb. 2021), p. 035014. DOI: [10.1103/PhysRevD.103.035014](https://doi.org/10.1103/PhysRevD.103.035014). URL: <https://link.aps.org/doi/10.1103/PhysRevD.103.035014>.
- [74] Benjamin Koch and Felix Hummel. “An exciting hint towards the solution of the neutron lifetime puzzle?” In: (2024). arXiv: [2403.00914 \[hep-ph\]](https://arxiv.org/abs/2403.00914). URL: <https://arxiv.org/abs/2403.00914>.
- [75] M. F. Blatnik et al. “An experimental search for an explanation of the difference between beam and bottle neutron lifetime measurements”. In: (2024). arXiv: [2406.10378 \[nucl-ex\]](https://arxiv.org/abs/2406.10378). URL: <https://arxiv.org/abs/2406.10378>.
- [76] Bartosz Fornal and Benjamín Grinstein. “Dark Matter Interpretation of the Neutron Decay Anomaly”. In: *Phys. Rev. Lett.* 120 (19 May 2018), p. 191801. DOI: [10.1103/PhysRevLett.120.191801](https://doi.org/10.1103/PhysRevLett.120.191801). URL: <https://link.aps.org/doi/10.1103/PhysRevLett.120.191801>.
- [77] Bartosz Fornal and Benjamín Grinstein. “Erratum: Dark Matter Interpretation of the Neutron Decay Anomaly [Phys. Rev. Lett. 120, 191801 (2018)]”. In: *Phys. Rev. Lett.* 124 (21 May 2020), p. 219901. DOI: [10.1103/PhysRevLett.124.219901](https://doi.org/10.1103/PhysRevLett.124.219901). URL: <https://link.aps.org/doi/10.1103/PhysRevLett.124.219901>.

- [78] Bartosz Fornal. “Neutron Dark Decay”. In: *Universe* 9.10 (2023). ISSN: 2218-1997. DOI: [10.3390/universe9100449](https://doi.org/10.3390/universe9100449). URL: <https://www.mdpi.com/2218-1997/9/10/449>.
- [79] M. Pfützner and K. Riisager. “Examining the possibility to observe neutron dark decay in nuclei”. In: *Phys. Rev. C* 97 (4 Apr. 2018), p. 042501. DOI: [10.1103/PhysRevC.97.042501](https://doi.org/10.1103/PhysRevC.97.042501). URL: <https://link.aps.org/doi/10.1103/PhysRevC.97.042501>.
- [80] Z. Tang et al. “Search for the Neutron Decay  $n \rightarrow X + \gamma$ , Where  $X$  is a Dark Matter Particle”. In: *Phys. Rev. Lett.* 121 (2 July 2018), p. 022505. DOI: [10.1103/PhysRevLett.121.022505](https://doi.org/10.1103/PhysRevLett.121.022505). URL: <https://link.aps.org/doi/10.1103/PhysRevLett.121.022505>.
- [81] X. Sun et al. “Search for dark matter decay of the free neutron from the UCNA experiment:  $n \rightarrow \chi + e^+e^-$ ”. In: *Phys. Rev. C* 97 (5 May 2018), p. 052501. DOI: [10.1103/PhysRevC.97.052501](https://doi.org/10.1103/PhysRevC.97.052501). URL: <https://link.aps.org/doi/10.1103/PhysRevC.97.052501>.
- [82] M. Klopff et al. “Constraints on the Dark Matter Interpretation  $n \rightarrow \chi + e^+e^-$  of the Neutron Decay Anomaly with the PERKEO II Experiment”. In: *Phys. Rev. Lett.* 122 (22 June 2019), p. 222503. DOI: [10.1103/PhysRevLett.122.222503](https://doi.org/10.1103/PhysRevLett.122.222503). URL: <https://link.aps.org/doi/10.1103/PhysRevLett.122.222503>.
- [83] J. R. Oppenheimer and G. M. Volkoff. “On Massive Neutron Cores”. In: *Phys. Rev.* 55 (4 Feb. 1939), pp. 374–381. DOI: [10.1103/PhysRev.55.374](https://doi.org/10.1103/PhysRev.55.374). URL: <https://link.aps.org/doi/10.1103/PhysRev.55.374>.
- [84] Richard C. Tolman. “Static Solutions of Einstein’s Field Equations for Spheres of Fluid”. In: *Phys. Rev.* 55 (4 Feb. 1939), pp. 364–373. DOI: [10.1103/PhysRev.55.364](https://doi.org/10.1103/PhysRev.55.364). URL: <https://link.aps.org/doi/10.1103/PhysRev.55.364>.
- [85] David McKeen et al. “Neutron Stars Exclude Light Dark Baryons”. In: *Phys. Rev. Lett.* 121 (6 Aug. 2018), p. 061802. DOI: [10.1103/PhysRevLett.121.061802](https://doi.org/10.1103/PhysRevLett.121.061802). URL: <https://link.aps.org/doi/10.1103/PhysRevLett.121.061802>.
- [86] A. Akmal, V. R. Pandharipande, and D. G. Ravenhall. “Equation of state of nucleon matter and neutron star structure”. In: *Phys. Rev. C* 58 (3 Sept. 1998), pp. 1804–1828. DOI: [10.1103/PhysRevC.58.1804](https://doi.org/10.1103/PhysRevC.58.1804). URL: <https://link.aps.org/doi/10.1103/PhysRevC.58.1804>.
- [87] Feryal Özel and Paulo Freire. “Masses, Radii, and the Equation of State of Neutron Stars”. In: *Annual Review of Astronomy and Astrophysics* 54. Volume 54, 2016 (2016), pp. 401–440. ISSN: 1545-4282. DOI: <https://doi.org/10.1146/annurev-astro-081915-023322>. URL: <https://www.annualreviews.org/content/journals/10.1146/annurev-astro-081915-023322>.
- [88] John Antoniadis et al. “A Massive Pulsar in a Compact Relativistic Binary”. In: *Science* 340.6131 (2013), p. 1233232. DOI: [10.1126/science.1233232](https://doi.org/10.1126/science.1233232). eprint: <https://www.science.org/doi/pdf/10.1126/science.1233232>. URL: <https://www.science.org/doi/abs/10.1126/science.1233232>.

- [89] Zaven Arzoumanian et al. “The NANOGrav 11-year Data Set: High-precision Timing of 45 Millisecond Pulsars”. In: *The Astrophysical Journal Supplement Series* 235.2 (Apr. 2018), p. 37. DOI: [10.3847/1538-4365/aab5b0](https://doi.org/10.3847/1538-4365/aab5b0). URL: <https://dx.doi.org/10.3847/1538-4365/aab5b0>.
- [90] Alessandro Strumia. “Dark Matter interpretation of the neutron decay anomaly”. In: *Journal of High Energy Physics* 2022.2 (2022), p. 67. ISSN: 1029-8479. DOI: [10.1007/JHEP02\(2022\)067](https://doi.org/10.1007/JHEP02(2022)067). URL: [https://doi.org/10.1007/JHEP02\(2022\)067](https://doi.org/10.1007/JHEP02(2022)067).
- [91] T. F. Motta, P. A. M. Guichon, and A. W. Thomas. “Neutron to dark matter decay in neutron stars”. In: *International Journal of Modern Physics A* 33.31 (2018), p. 1844020. DOI: [10.1142/S0217751X18440207](https://doi.org/10.1142/S0217751X18440207). URL: <https://doi.org/10.1142/S0217751X18440207>.
- [92] Benjamín Grinstein, Chris Kouvaris, and Niklas Grønlund Nielsen. “Neutron Star Stability in Light of the Neutron Decay Anomaly”. In: *Phys. Rev. Lett.* 123 (9 Aug. 2019), p. 091601. DOI: [10.1103/PhysRevLett.123.091601](https://link.aps.org/doi/10.1103/PhysRevLett.123.091601). URL: <https://link.aps.org/doi/10.1103/PhysRevLett.123.091601>.
- [93] Mar Bastero-Gil, Teresa Huertas-Roldan, and Daniel Santos. “The neutron decay anomaly, neutron stars and dark matter”. In: (2024). arXiv: [2403.08666](https://arxiv.org/abs/2403.08666) [astro-ph.CO]. URL: <https://arxiv.org/abs/2403.08666>.
- [94] James M. Cline and Jonathan M. Cornell. “Dark decay of the neutron”. In: *Journal of High Energy Physics* 2018.7 (2018), p. 81. ISSN: 1029-8479. DOI: [10.1007/JHEP07\(2018\)081](https://doi.org/10.1007/JHEP07(2018)081). URL: [https://doi.org/10.1007/JHEP07\(2018\)081](https://doi.org/10.1007/JHEP07(2018)081).
- [95] Wasif Husain, Theo F. Motta, and Anthony W. Thomas. “Consequences of neutron decay inside neutron stars”. In: *Journal of Cosmology and Astroparticle Physics* 2022.10 (Oct. 2022), p. 028. DOI: [10.1088/1475-7516/2022/10/028](https://dx.doi.org/10.1088/1475-7516/2022/10/028). URL: <https://dx.doi.org/10.1088/1475-7516/2022/10/028>.
- [96] Susan Gardner and Mohammadreza Zakeri. “Probing Dark Sectors with Neutron Stars”. In: *Universe* 10.2 (2024). ISSN: 2218-1997. DOI: [10.3390/universe10020067](https://www.mdpi.com/2218-1997/10/2/67). URL: <https://www.mdpi.com/2218-1997/10/2/67>.
- [97] K. Riisager et al. “Be11( $\beta$ p), a quasi-free neutron decay?” In: *Physics Letters B* 732 (2014), pp. 305–308. ISSN: 0370-2693. DOI: <https://doi.org/10.1016/j.physletb.2014.03.062>. URL: <https://www.sciencedirect.com/science/article/pii/S0370269314002299>.
- [98] A.C.C. Villari. “The accelerated ISOL technique and the SPIRAL project”. In: *Nuclear Physics A* 693.1 (2001). Radioactive Nuclear Beams, pp. 465–476. ISSN: 0375-9474. DOI: [https://doi.org/10.1016/S0375-9474\(01\)01107-1](https://doi.org/10.1016/S0375-9474(01)01107-1). URL: <https://www.sciencedirect.com/science/article/pii/S0375947401011071>.
- [99] URL: [faster.in2p3.fr](https://www.sciencedirect.com/science/article/pii/S0375947401011071).
- [100] G. F. Knoll. *Radiation Detection and Measurement*. 3rd. John Wiley and Sons, 2000.

- [101] T.J. Langford et al. “Event identification in  $^3\text{He}$  proportional counters using rise-time discrimination”. In: *Nuclear Instruments and Methods in Physics Research Section A: Accelerators, Spectrometers, Detectors and Associated Equipment* 717 (2013), pp. 51–57. ISSN: 0168-9002. DOI: <https://doi.org/10.1016/j.nima.2013.03.062>. URL: <https://www.sciencedirect.com/science/article/pii/S0168900213003720>.
- [102] Dmitry Testov. “Effect of shell closure  $N = 50$  and  $N = 82$  on the structure of very neutron-rich nuclei produced at ALTO: measurements of neutron emission probabilities and half lives of nuclei at astrophysical r-processes path”. PhD thesis. 2014. URL: <https://theses.hal.science/tel-01059803>.
- [103] Xiaobo Liu, Yaru Shi, and Jiansheng Li. “Time-dependent multiplicity for Cf-252 neutron source”. In: *Applied Radiation and Isotopes* 199 (2023), p. 110836. ISSN: 0969-8043. DOI: <https://doi.org/10.1016/j.apradiso.2023.110836>. URL: <https://www.sciencedirect.com/science/article/pii/S0969804323001896>.
- [104] D. Testov et al. “The  $^3\text{He}$  long-counter TETRA at the ALTO ISOL facility”. In: *Nuclear Instruments and Methods in Physics Research Section A: Accelerators, Spectrometers, Detectors and Associated Equipment* 815 (2016), pp. 96–103. ISSN: 0168-9002. DOI: <https://doi.org/10.1016/j.nima.2015.11.150>. URL: <https://www.sciencedirect.com/science/article/pii/S0168900215015697>.
- [105] D. Testov, E. Kuznetsova, and J.N. Wilson. “Response of the TETRA  $4\pi$  detector to neutrons”. In: *Journal of Instrumentation* 10.09 (Sept. 2015), P09011. DOI: [10.1088/1748-0221/10/09/P09011](https://doi.org/10.1088/1748-0221/10/09/P09011). URL: <https://dx.doi.org/10.1088/1748-0221/10/09/P09011>.
- [106] Sang-Tae Park. “Neutron energy spectra of  $^{252}\text{Cf}$ , Am-Be source and of the  $\text{D}(\text{d},\text{n})^3\text{He}$  reaction”. In: *Journal of Radioanalytical and Nuclear Chemistry* 256.1 (2003), pp. 163–166. ISSN: 1588-2780. DOI: [10.1023/A:1023333016692](https://doi.org/10.1023/A:1023333016692). URL: <https://doi.org/10.1023/A:1023333016692>.
- [107] M.-M. Bé et al. *Table of Radionuclides*. Vol. 2. Monographie BIPM-5. Pavillon de Breteuil, F-92310 Sèvres, France: Bureau International des Poids et Mesures, 2004. ISBN: 92-822-2207-1. URL: [http://www.bipm.org/utils/common/pdf/monographieRI/Monographie\\_BIPM-5\\_Tables\\_Vol2.pdf](http://www.bipm.org/utils/common/pdf/monographieRI/Monographie_BIPM-5_Tables_Vol2.pdf).
- [108] T. Björnstad et al. “The decay of  $^8\text{He}$ ”. In: *Nuclear Physics A* 366.3 (1981), pp. 461–468. ISSN: 0375-9474. DOI: [https://doi.org/10.1016/0375-9474\(81\)90522-4](https://doi.org/10.1016/0375-9474(81)90522-4). URL: <https://www.sciencedirect.com/science/article/pii/0375947481905224>.
- [109] M.J.G. Borge et al. “Beta-delayed triton emission in the decay of  $^8\text{He}$ ”. In: *Nuclear Physics A* 460.3 (1986), pp. 373–380. ISSN: 0375-9474. DOI: [https://doi.org/10.1016/0375-9474\(86\)90420-3](https://doi.org/10.1016/0375-9474(86)90420-3). URL: <https://www.sciencedirect.com/science/article/pii/0375947486904203>.
- [110] URL: <http://g4beamline.muonsinc.com>.
- [111] *NuDat3.0*. URL: <https://www.nndc.bnl.gov/nudat3/>.

- [112] M. Kanafani et al. “High-precision measurement of the  ${}^6\text{He}$  half-life”. In: *Phys. Rev. C* 106 (4 Oct. 2022), p. 045502. DOI: [10.1103/PhysRevC.106.045502](https://doi.org/10.1103/PhysRevC.106.045502). URL: <https://link.aps.org/doi/10.1103/PhysRevC.106.045502>.
- [113] S. Navas et al. “Review of Particle Physics”. In: *Phys. Rev. D* 110 (3 Aug. 2024), p. 030001. DOI: [10.1103/PhysRevD.110.030001](https://doi.org/10.1103/PhysRevD.110.030001). URL: <https://link.aps.org/doi/10.1103/PhysRevD.110.030001>.
- [114] H-W Hammer, C Ji, and D R Phillips. “Effective field theory description of halo nuclei”. In: *Journal of Physics G: Nuclear and Particle Physics* 44.10 (Sept. 2017), p. 103002. DOI: [10.1088/1361-6471/aa83db](https://doi.org/10.1088/1361-6471/aa83db). URL: <https://dx.doi.org/10.1088/1361-6471/aa83db>.
- [115] G. Papadimitriou et al. “Charge radii and neutron correlations in helium halo nuclei”. In: *Phys. Rev. C* 84 (5 Nov. 2011), p. 051304. DOI: [10.1103/PhysRevC.84.051304](https://doi.org/10.1103/PhysRevC.84.051304). URL: <https://link.aps.org/doi/10.1103/PhysRevC.84.051304>.
- [116] Y.L. Sun et al. “Three-body breakup of  ${}^6\text{He}$  and its halo structure”. In: *Physics Letters B* 814 (2021), p. 136072. ISSN: 0370-2693. DOI: <https://doi.org/10.1016/j.physletb.2021.136072>. URL: <https://www.sciencedirect.com/science/article/pii/S0370269321000125>.
- [117] J. D. Goss et al. “Angular distribution measurements for  ${}^{14}\text{C}(d,p){}^{15}\text{C}$  and the level structure of  ${}^{15}\text{C}$ ”. In: *Phys. Rev. C* 12 (6 Dec. 1975), pp. 1730–1738. DOI: [10.1103/PhysRevC.12.1730](https://doi.org/10.1103/PhysRevC.12.1730). URL: <https://link.aps.org/doi/10.1103/PhysRevC.12.1730>.
- [118] J.S. Winfield et al. “Single-neutron transfer from  ${}^{11}\text{Be}$  via the (p,d) reaction with a radioactive beam”. In: *Nuclear Physics A* 683.1 (2001), pp. 48–78. ISSN: 0375-9474. DOI: [https://doi.org/10.1016/S0375-9474\(00\)00463-2](https://doi.org/10.1016/S0375-9474(00)00463-2). URL: <https://www.sciencedirect.com/science/article/pii/S0375947400004632>.
- [119] H Ejiri and J D Vergados. “Neutron disappearance inside the nucleus”. In: *Journal of Physics G: Nuclear and Particle Physics* 46.2 (Jan. 2019), p. 025104. DOI: [10.1088/1361-6471/aaf55b](https://doi.org/10.1088/1361-6471/aaf55b). URL: <https://dx.doi.org/10.1088/1361-6471/aaf55b>.
- [120] David McKeen and Maxim Pospelov. “How Long Does the Hydrogen Atom Live?” In: *Universe* 9.11 (2023). ISSN: 2218-1997. DOI: [10.3390/universe9110473](https://doi.org/10.3390/universe9110473). URL: <https://www.mdpi.com/2218-1997/9/11/473>.
- [121] Roberto Tartaglia. “BOREXINO: the technical description”. In: *Nuclear Instruments and Methods in Physics Research Section A: Accelerators, Spectrometers, Detectors and Associated Equipment* 461.1 (2001). 8th Pisa Meeting on Advanced Detectors, pp. 327–328. ISSN: 0168-9002. DOI: [https://doi.org/10.1016/S0168-9002\(00\)01235-3](https://doi.org/10.1016/S0168-9002(00)01235-3). URL: <https://www.sciencedirect.com/science/article/pii/S0168900200012353>.
- [122] M. Agostini et al. “Test of Electric Charge Conservation with Borexino”. In: *Phys. Rev. Lett.* 115 (23 Dec. 2015), p. 231802. DOI: [10.1103/PhysRevLett.115.231802](https://doi.org/10.1103/PhysRevLett.115.231802). URL: <https://link.aps.org/doi/10.1103/PhysRevLett.115.231802>.

## BIBLIOGRAPHY

---

[123] URL: <https://frib.msu.edu/users/beams/calculator?a=17&z=6>.

# Abstract

## Français

L'écart entre les expériences dites du faisceau et de la bouteille mesurant la durée de vie du neutron libre pourrait être expliqué en considérant une nouvelle voie de désintégration du neutron en matière noire. Une telle décroissance pourrait être mise en lumière dans une sélection de noyaux radioactifs dans lesquels certains neutrons sont très faiblement liés au reste de la structure nucléaire. Dans le cas du noyau borroméen  ${}^6\text{He}$ , une décroissance en matière noire d'un des deux neutrons du halo produirait nécessairement les particules suivantes :  ${}^4\text{He} + n + \chi$ . Observer une émission de neutron corrélée à la décroissance de l'hélium 6 fournirait ainsi une signature claire et unique de création de matière noire. Un faisceau intense  ${}^6\text{He}^+$  produit au Grand Accélérateur National d'Ions Lourds (GANIL) couplé au détecteur de neutron TETRA a permis d'établir une limite supérieure à l'existence de cette décroissance en matière noire dans l'hélium 6 à  $\text{Br}_\chi \leq 4.0 \times 10^{-10}$  avec un degré de confiance de 95%. Cette limite expérimentale a également été traduite en une contrainte de l'ordre de  $\mathcal{O}(10^{-5})$  pour la probabilité de décroissance en matière noire du neutron libre.

**Mots-clés :** Anomalie de la durée de vie du neutron ; Décroissance en matière noire du neutron ;  ${}^6\text{He}$  ; GANIL ; TETRA

## English

Neutron dark decays have been suggested as a solution to the discrepancy between bottle and beam experiments, providing a dark matter candidate that can be searched for in halo nuclei. The free neutron in the final state following the decay of  ${}^6\text{He}$  into  ${}^4\text{He} + n + \chi$  provides an exceptionally clean detection signature when combined with a high-efficiency neutron detector. Using a high-intensity  ${}^6\text{He}^+$  beam at the Grand Accélérateur National d'Ions Lourds (GANIL), a search for a coincident neutron signal resulted in an upper limit on a dark decay branching ratio of  $\text{Br}_\chi \leq 4.0 \times 10^{-10}$  with a 95% confidence level. Using the dark neutron decay model proposed originally by Fornal and Grinstein, we translate this into an upper bound on a dark neutron branching ratio of  $\mathcal{O}(10^{-5})$ , improving over global constraints by one to several orders of magnitude depending on  $m_\chi$ .

**Keywords :** Neutron lifetime discrepancy ; Neutron dark decay ;  ${}^6\text{He}$  ; GANIL ; TETRA